ORNL/TM-2018/811

Embedded Sensors and Controls to Improve Component Performance and Reliability – Final Report

Alexander Melin
Roger Kisner
Bryan Blaise
Christopher Meert
F. Kyle Reed

March 2018

OAK RIDGE NATIONAL LABORATORY
MANAGED BY UT-BATTELLE FOR THE US DEPARTMENT OF ENERGY

ORNL/TM-2018/811

Electrical and Electronics Systems Research Division

EMBEDDED SENSORS AND CONTROLS TO IMPROVE COMPONENT PERFORMANCE AND RELIABILITY – FINAL REPORT

Alexander Melin
Roger Kisner
Bryan Blaise
Christopher Meert
F. Kyle Reed

Date Published: April 2018

Prepared by
OAK RIDGE NATIONAL LABORATORY
P.O. Box 2008
Oak Ridge, Tennessee 37831-6285
managed by
UT-Battelle, LLC
for the
US DEPARTMENT OF ENERGY
under contract DE-AC05-00OR22725

CONTENTS

LIST OF FIGURES

LIST OF TABLES

ACRONYMS

AMB	Active Magnetic Bearing
ASI	Advanced Sensors and Instrumentation
AWG	American Wire Gauge
DOE	Department of Energy
DOE-NE	Department of Energy, Office of Nuclear Energy
FEA	Finite-Element Analysis
I&C	Instrumentation and Control
LQG	Linear Quadratic Gaussian
MIMO	Multiple Input Multiple Output
MPC	Model Predictive Control
NEET	Nuclear Energy Enabling Technologies
OD	Outer Diameter
ORNL	Oak Ridge National Laboratory
PI	Proportional Integral
PID	Proportional Integral Derivative
PWM	Pulse Width Modulation
SISO	Single Input Single Output

ABSTRACT

Oak Ridge National Laboratory has researched embedded instrumentation and controls (I&C) for extreme environments under the Department of Energy, Office of Nuclear Energy's Nuclear Energy Enabling Technology program. Advanced sensors and controls have the potential to dramatically increase the performance, reliability, and efficiency of nuclear reactor components; however, the extreme environments of advanced reactor designs limit the options for sensors, actuators, and control designs. The focus of this research is to address two of the extreme environment challenges to embedded I&C: to fill technology gaps needed for electromagnetic systems that can operate at temperatures greater than 700 °C and in corrosive salt environments. A magnetically suspended, canned-rotor pump was chosen for the embedded I&C development platform because it is a system with a practical need in industry and because the sensors, actuators, and embedded I&C technologies needed to successfully build this platform will be widely applicable to any high-temperature components that utilize electromagnetic interactions. This design also eliminates the need for pump seals and mechanical bearings, which are the main sources of pump failures and maintenance costs. During the project a conceptual design for the high-temperature, magnetically suspended pump was developed and analyzed for manufacturability and reliability. Specifications for the materials, control system, sensors, mechanical performance, high-temperature wiring, and electromagnetic properties were developed for the conceptual design. The canned-rotor design of the high-temperature pump presents unique fluid force characteristics arising from the thin fluid channel between the rotor and stator. A model of the fluid forces was developed, and the impact of these forces on the stability and performance of magnetic bearing controllers was studied. Then a room temperature, bench-scale, magnetic testbed was designed and fabricated for testing the performance of sensors and electromagnetic actuators, modern control design techniques, closed-loop system identification, state estimation, and model uncertainty. Finally, a loop-scale testbed with submerged magnetic bearings was designed and fabricated. This testbed will be used to analyze the stability and performance of control system designs in response to the nonlinear and cross-coupling fluid effects between the shaft axes of motion, rotordynamics, gyroscopic effects, and impeller disturbances.

1 INTRODUCTION

Oak Ridge National Laboratory (ORNL), through the Department of Energy, Office of Nuclear Energy's (DOE-NE) Nuclear Energy Enabling Technology (NEET) program, has researched embedded instrumentation and controls (I&C) for advanced reactor systems. The NEET program focuses on the development of cross-cutting technologies that directly support the DOE-NE advanced reactor and fuel concepts with the goal of dramatically improving component performance. Specifically, this work was sponsored by the Advanced Sensors and Instrumentation (ASI) subprogram of NEET. The ASI program supports research to develop the scientific basis for sensors and supporting infrastructure technology that addresses current gaps in technology relating to measurements at existing and advanced nuclear power plants and their fuel cycles. This program focuses on monitoring and control technologies and their integration along with communications and data transmission for digital technologies.

Under these programs, ORNL has been researching advanced I&C concepts for extreme environments since 2012. Existing nuclear reactors and advanced reactor designs contain physical environments that make the integration of sensors and controls into components difficult. These reactor components must survive high radiation, corrosive materials, high temperatures, and sometimes high pressures to operate reliably and safely for long periods. Commercially available sensors, actuators, and controls do not

currently exist that will operate in some of the more challenging nuclear environments, and existing solutions are often expensive and inefficient. This research focuses on bridging some of the technical gaps in sensing, actuation, and control for components that operate in extreme environments. The specific component chosen to demonstrate embedded I&C for extreme environments was a high-temperature pump for molten salt. This component was chosen in part because of its wide applicability to nuclear reactors, solar collection systems, and other high-temperature applications. This component was also chosen because the design limitations arising from the difficult environment can be overcome through the development of high-temperature electromagnetic sensors and actuators and advanced control algorithms. The successful development of these technologies cross-cut a wide range of industrial applications by significantly raising the maximum temperature at which electromagnetic devices can operate. This development would enable high-temperature versions of any device that requires electromagnetics to operate, such as induction sensors, valves, motors, or magnetic bearings.

The first phase of this project researched the technologies needed to develop a high-temperature (700 °C) molten salt pump. After researching sensors, actuators, materials, controls, fluid effects, corrosion, and pump designs, a conceptual design for the pump was created [5, 10]. The conceptual design uses a magnetically suspended canned-rotor pump with a switched reluctance motor. The magnetic suspension system negates the need for ball bearings, which have a maximum operating temperature of <260 °C [3], and allows the rotor to be submerged in the molten salt during operation, which eliminates the need for shaft seals. The canned-rotor design, which uses thin metal "cans" around the rotor outer diameter and stator inner diameter, protects the more sensitive components from corrosion by the salt. Nickle cobalt alloys known commercially as Hiperco 50 and Hiperco 27 were selected as the electromagnetic core materials as they are two of the few magnetic materials with Curie temperatures and operating temperatures above 700 °C. Inconel or Hastelloy series metals were identified as potential materials for the protective cans because of their corrosion resistance and strength. Other options involve electroplating the rotor and stator with noble metals like rhodium that are highly resistant to oxidation and have similar coefficients of thermal expansion to steels. A strategy for control and measurement of the conceptual design was outlined, and multiple options were compared. Finally, in the conceptual design, system requirements for the control system, motor/pump, mechanical performance, rotational dynamics, electrical and magnetic properties, sensors, high-temperature wiring, environmental conditions, and reliability were developed.

Dynamic models of the conceptual design were developed in [7]. A Jeffcott rotor model with lumped shaft mass was used to describe the coupled rotor dynamics. The thin fluid gap in the canned-rotor design creates large fluid forces on the shaft that are not present in a typical magnetic bearing application. In [7] and [11], theoretical models of the fluid forces and damping were developed. These fluid forces can exhibit nonlinear Taylor-Couette flow bifurcations and are dependent on the shaft position. They also cause large coupling forces between the magnetic bearing control axes. Control stability and performance were investigated for the complete model with the fluid and shaft gyroscopic forces. The traditional decoupled Proportional Integral Derivative (PID) controllers typically used to independently control each magnetic bearing axis performed poorly in the presence of the coupling forces and in some cases were unable to stabilize the shaft position. Controllers designed using optimal control techniques that can capture cross-axis coupling were shown to perform well and mitigate the impact of the cross-axis coupling on the control stability and performance.

The manufacturability of the conceptual design was studied by Kisner et al. [4]. Based on the conceptual design, techniques necessary for fabricating the design were identified and evaluated. Each component was categorized by function, materials, operating conditions, material considerations, interfaces, and failure

modes. Using this component information, possible fabrication methods and joining options were considered based on their impact on dimensions and tolerance, materials, and failure modes. Then the material options for pump fabrication were investigated, including commonly used fabrication methods for each material, structural considerations, heat transfer, availability, and chemical compatibility. Finally, fabrication and joining methods were analyzed for each component to determine potential challenges to the fabrication and the impacts on the structural and functional aspects of each component.

In the next phase of the project, ORNL designed and fabricated a bench-scale magnetic bearing testbed for room-temperature testing of embedded I&C concepts. The goal of this testbed is to investigate the performance of sensors and electromagnetic actuators, modern control design techniques, closed-loop system identification, state estimation, and model uncertainty. In [9], details of the bench-scale testbed design are presented. The testbed consists of two radial magnetic bearings and one axial magnetic bearing that can produce up to 500 N of force. The mechanical and electromagnetic systems were designed using a coupled process. A parameterized bearing geometry was developed for the coupled model that was used to optimize the geometry of the magnetic bearings to reduce the bearing mass while maximizing the bearing forces achievable. A custom power electronics unit was developed for the magnetic bearings using some commercially available components. The control system was deployed using a high-speed, real-time computer. A more detailed summary of the bench-scale design and fabrication is given in Section 2.1, and the complete details are provided in [9].

In the final phase of the project, a loop-scale testbed was developed that has fluid force characteristics analogous to the expected high-temperature pump. This testbed is designed to test the control algorithms, system identification, and state estimation techniques under conditions like those experienced by the high-temperature conceptual design. This testbed is designed to be a fully operational radial impeller pump with submerged magnetic bearings and a canned rotor design.

For the second phase of the project, a low-temperature pump testbed for developing and testing embedded I&C during pump operation was developed. This testbed will be integrated with a water loop to verify robustness of the I&C to nonlinear and cross-coupling fluid effects between the shaft axes of motion, rotordynamics and gyroscopic effects, and impeller disturbances. A summary of the design of this loop-scale testbed is given in Section 2.2, and more detailed information on the design can be found in [8].

The report is organized as follows. In Section 2, design and fabrications of the bench-scale and loop-scale testbeds are discussed. Then assembly and waterproofing of the loop-scale testbed are presented in Section 3. A detailed derivation of the dynamic models of the magnetic bearing systems is given in Section 4, including models with independent coil dynamics and flexible shaft analysis. Section 5 presents system identification techniques for magnetic bearings and results for the testbeds. Control design and state estimation for magnetic bearings are addressed in Section 6. Next, some challenges that arose during the development of the initial stabilizing controller for the loop-scale magnetic bearings are given in Section 7. Future topics of research are discussed in Section 8, and finally conclusions are given in Section 9.

2 TESTBED DESIGNS

To develop technologies for embedded I&C in extreme environments, two testbeds were designed and fabricated during this project. The first testbed to be designed and fabricated was a bench-scale magnetic bearing system. This testbed operates at room temperature and includes two radial magnetic bearings, an axial magnetic bearing, and two touchdown bearings. The purpose of the bench-scale testbed is to provide a flexible platform for testing embedded system identification techniques and control algorithms needed for high-temperature magnetic bearing operation, which will eventually be applied to high-temperature components.

The second loop-scale testbed that was designed and fabricated was a larger magnetic bearing pump with a submerged shaft. This testbed was created to investigate embedded I&C challenges associated with scaling up the magnetic bearings size, nonlinear fluid forces from the thin fluid gap between the rotor and stator, flexible shaft modes, and impeller forces.

Detailed information about the designs of the bench-scale testbed and the loop-scale testbed is available in [9] and [8], respectively, so the designs will only be summarized in the remainder of this section.

2.1 Bench-Scale Testbed*

The goal of the testbed design was to provide a flexible platform for hardware in the loop testing of embedded I&C. The testbed requirements for flexible operation and safety lead to the following design features:

- easily changeable rotor and stator laminations,
- touch-down bearings to protect the rotor and stator,
- external position sensors,
- variable axial spacing between bearings,
- external shaft torque, and
- optical table mount.

The easily changeable rotor and stator laminations allow different lamination materials to be tested with and without protective cans, with varying air gaps between the stator and rotor, and multiple stack lengths. The external position sensors are high-precision and high-bandwidth sensors that will be used for the initial feedback control stabilization of the rotor and to test and validate sensorless bearing control techniques. The variable axial spacing between bearings will allow different physical configurations and different shaft moments of inertia and mode shapes to be tested to study the sensitivity of the controller to variations in these parameters. External shaft torque is supplied by a flexible coupling to an induction motor for testing the effect of rotational velocity and shaft imbalance on the stability and performance of different feedback control designs. To provide stability and options for precision measurement, the testbed is designed to be mounted to an optics table. Figure 1 shows a rendering of the final testbed design, and Figure 2 shows a cross-sectional view of the final testbed design.

The bench-scale testbed design consists of a baseplate that bolts to an optical table for rigidity. The other components of the testbed are designed to be modular and clamp to the baseplate. The touchdown bearings

*All material in this section has been taken from [9].

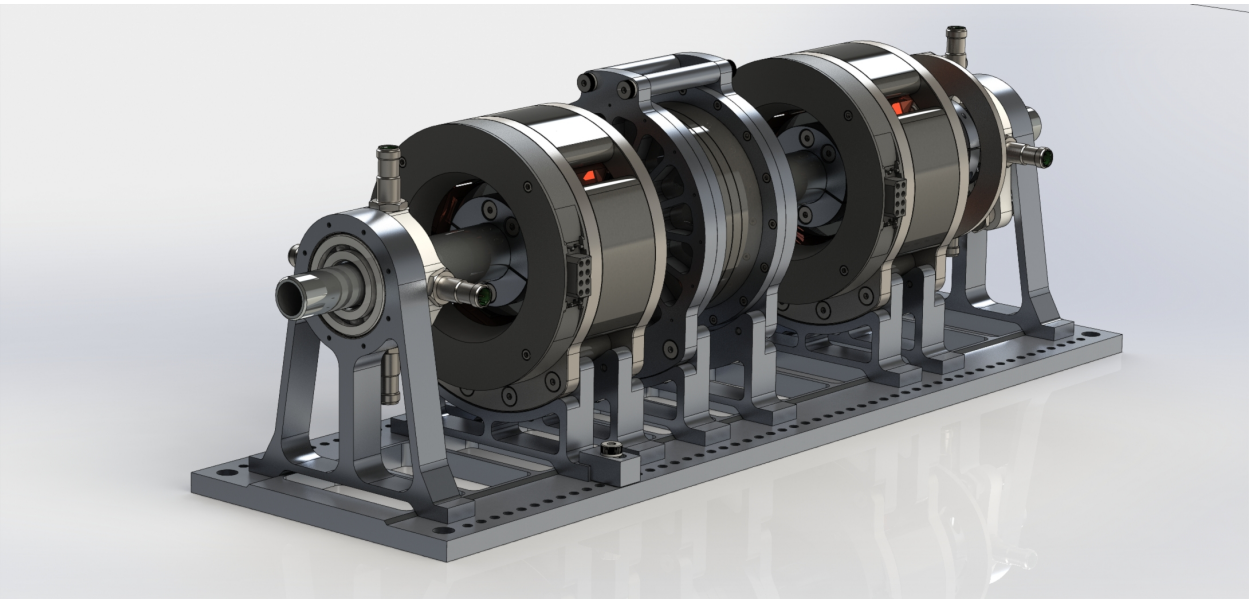

Figure 1. Final bench-scale testbed design.

are mounted to towers and held in place by bearing tolerance rings that provide some damping when the shaft contacts the touchdown bearing. The external position sensors are mounted to the tower that houses the touchdown bearings so that they are spaced at opposite ends of the shaft and there is no physical contact with the shaft when it is levitating. Two radial active magnetic bearings (AMBs) are used to control the radial movement and tilt of the shaft. The two radial AMBs are located on either side of an axial AMB that controls the shaft's axial movement. Everything is mounted by high-precision shoulder bolts and shaft collars that allow different stator and rotor configurations to be used. The radial magnetic bearings utilize split stators to minimize stray magnetic fields that can cause coupling between the axes. Figure 3 shows an exploded view of a radial bearing.

The testbed design utilizes some parts that were made using additive manufacturing. Specifically, the sensor mounts and the covers and tie-downs for the stator coil wires were printed in ABS using a 3D printer. The testbed assembled without sensors is shown in Figure 4.

To design the geometry of the radial bearing, the geometry is parameterized using the following dimensions. Figure 5 shows the location of the dimensions on the stator and rotor cross section.

- s_0 - Air gap between the stator and rotor
- w_t - Width of a stator tooth
- w_y - Width of the stator yoke
- h_t - Height of a stator tooth
- l_s - Axial length of the stator and rotor stacks
- d_r - Diameter of the rotor
- d_s - Diameter of the shaft

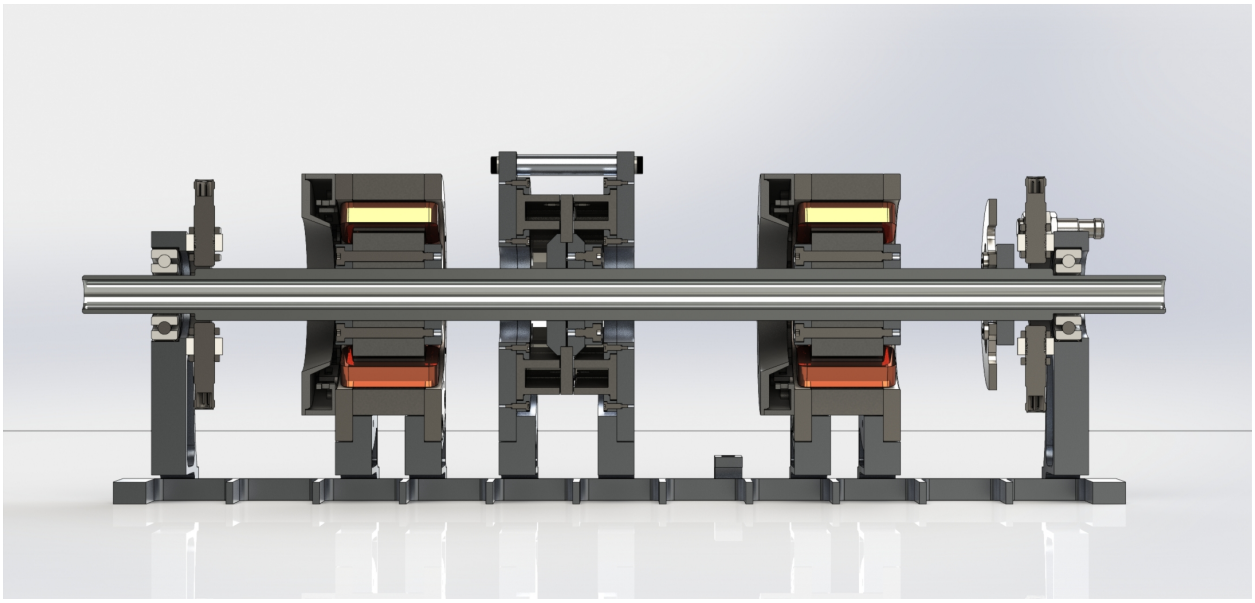

Figure 2. Cross-sectional view of the final bench-scale testbed design.

- θ_t - Angle between two teeth in the stator

The geometry parameters listed are used to calculate the total flux path lengths through the stator and rotor. The flux path for the stator is given by the equation

$$l_s = 2h_t + w_y + \theta_t \left(\frac{d_r + w_y + s(s_0 + h_t)}{2} \right). \tag{1}$$

The flux path length through the rotor is given by the equations

$$\gamma_a = \theta_t - 1 - \frac{d_s}{d_r}, \tag{2}$$

$$\gamma_b = \frac{1}{2}\left(1 - \frac{d_s}{d_r}\right), \tag{3}$$

$$f_H = \frac{d_r}{2}(1 - \cos(\gamma_b)), \tag{4}$$

$$l_r = \frac{\gamma_a}{4}(d_r - d_s) + \frac{\pi}{4}(d_r - d_s) - 2f_H. \tag{5}$$

If the stator has n teeth in total, the angle between two teeth is given by

$$\theta_t = 2\pi/n. \tag{6}$$

The testbed stator and rotor laminations are made from 29 gauge M19 C5 steel. Figure 6 shows the B-H curve for the M19 steel. The equations that relate the magnetic flux B with the magnetization force H are

$$\mu = \mu_0 + \frac{1}{\exp^{k_1 B^2} + k_2}, \tag{7}$$

$$H = \frac{B}{100\mu}, \tag{8}$$

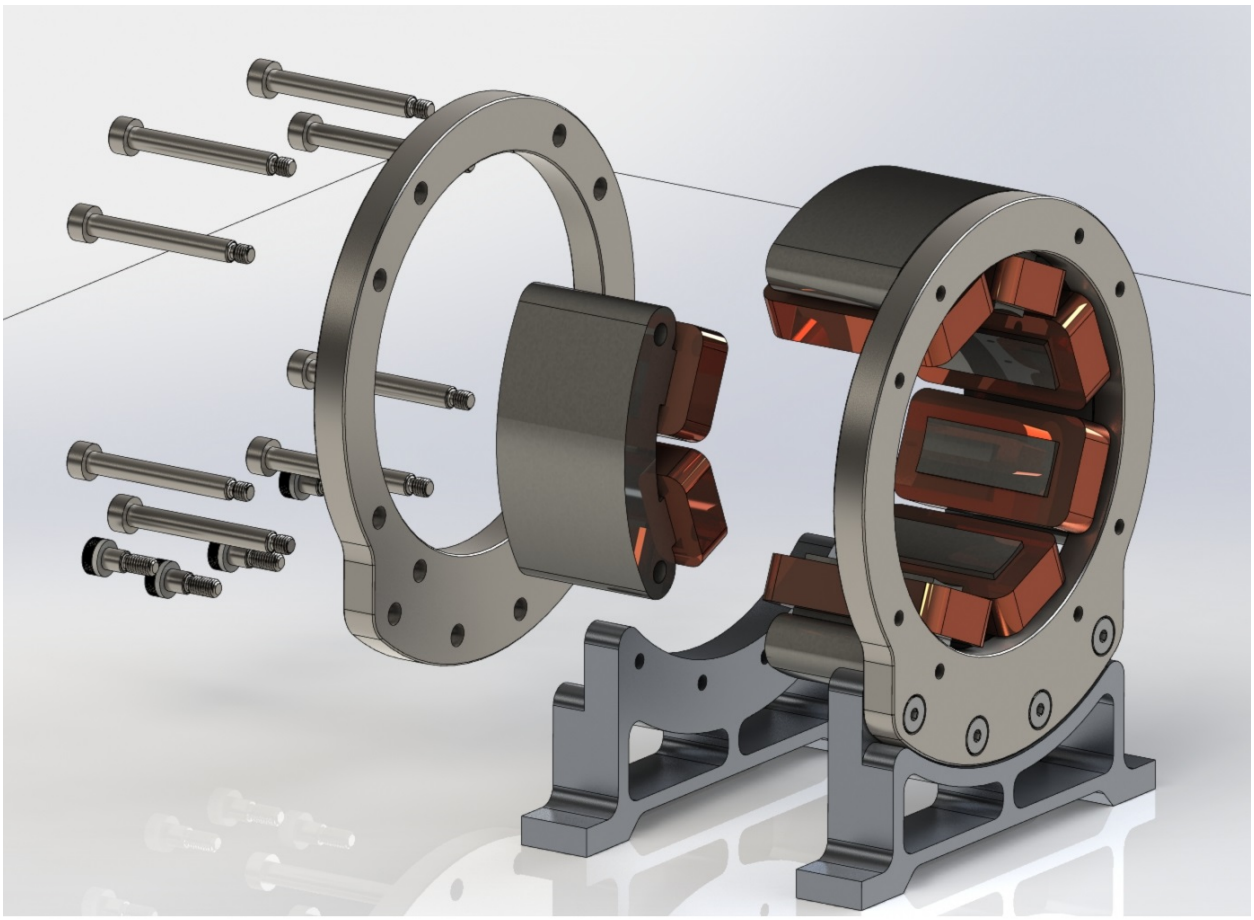

Figure 3. Exploded view of a radial bearing stator.

where μ_0 is the permeability of air, $k_1 = 2.477$, and $k_2 = 83.03$.

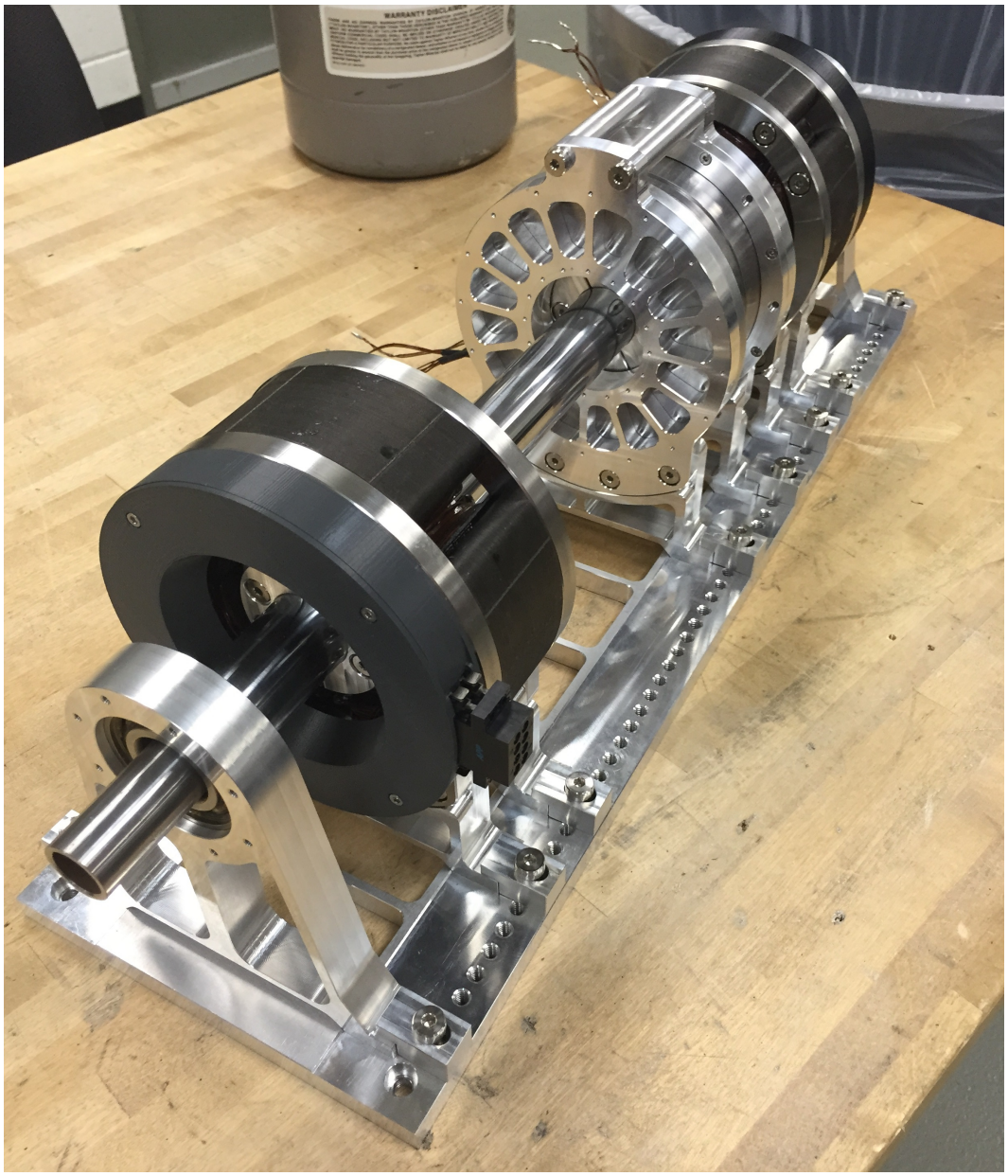

Figure 4. Assembled testbed without sensors or power electronics.

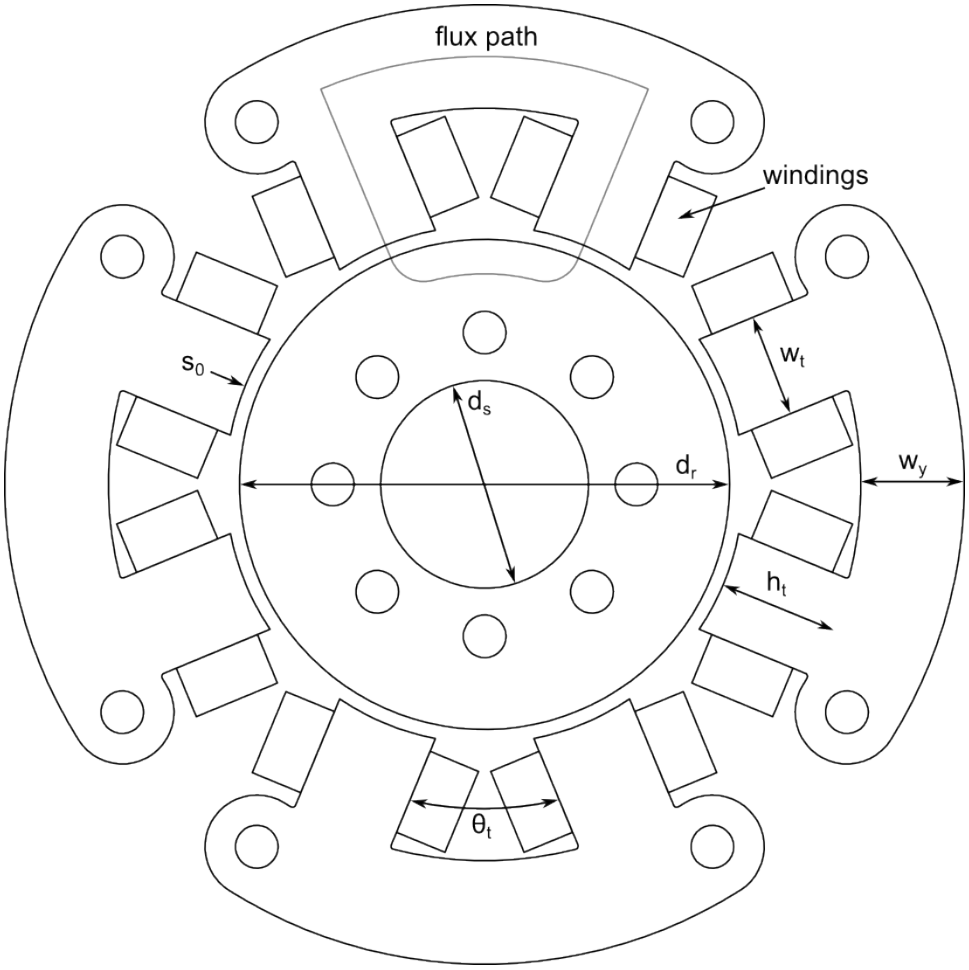

Figure 5. Dimensions used in the calculation of the flux path lengths.

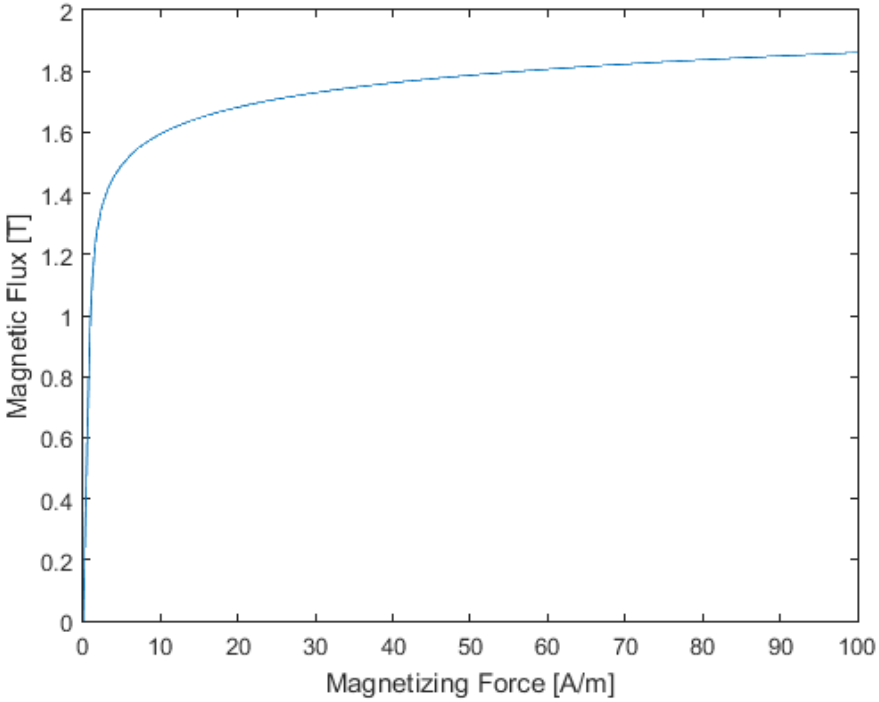

Figure 6. B-H curve for the M19 steel used in the testbed laminations.

The optimized radial bearing design geometry for the bench-scale testbed is given in Table 1. The optimal geometry was chosen using the minimum air gap of 0.0005 m because the magnetic flux is maximized at this rotor position and can easily become saturated with sub-optimal geometry, leading to decreased dynamic response of the bearing. Because there are two bench-scale bearing radial magnetic bearings, they will be denoted as the *A* and *B* bearings.

Table 1. Radial AMB Optimized Geometry

Parameter	Value	Units
s_0	0.002	m
w_t	0.015	m
w_y	0.015	m
h_t	0.017	m
l_s	0.04125	m
d_r	0.071	m
d_s	0.030	m
θ_t	$\pi/4$	rad
L_A	0.14126	m
L_B	0.12348	m
S_A	0.24744	m
S_B	0.23211	m

The nonlinear force characteristics of the radial bearings are shown in Figure 7 over the range of shaft motion and coil currents.

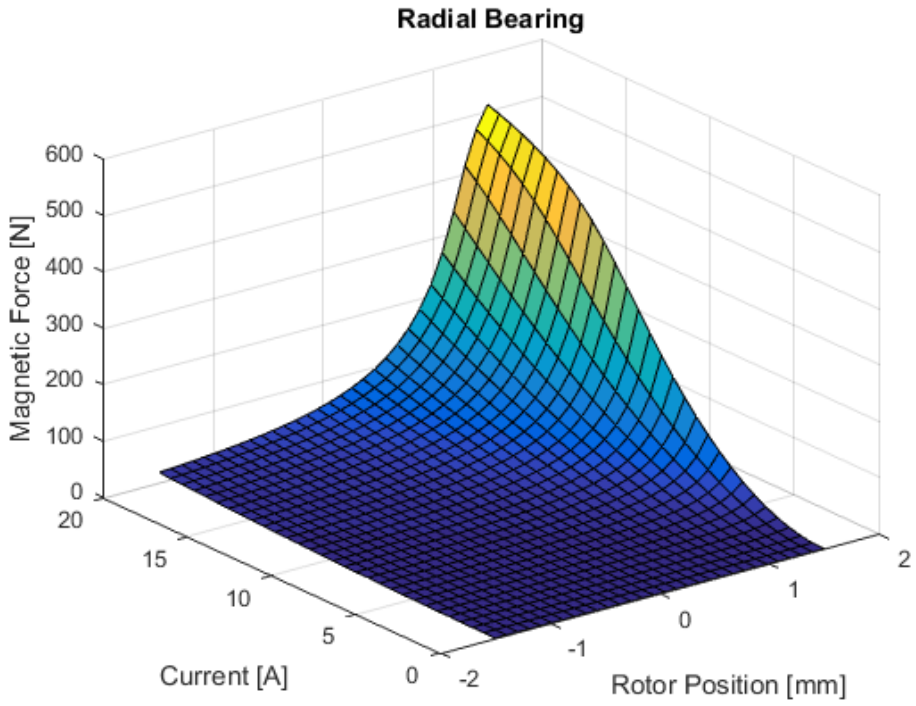

Figure 7. Radial bearing force as a function of current and airgap.

2.2 Loop-Scale Testbed[†]

The loop-scale testbed is designed to be a low-temperature analog of a high-temperature magnetic bearing pump with a canned-rotor design. This testbed has a submerged shaft with a canned-rotor design that has a small fluid-filled gap between the rotor and stator. The nonlinear fluid forces created in this gap are a primary source of uncertain time-varying external disturbances to the shaft. For the high-temperature design to be feasible, a stabilizing feedback controller must be designed for the low-temperature testbed that can maintain shaft position despite these external disturbances. In [11] the authors present a detailed derivation of the hydrodynamics forces due to the small fluid-filled gap for the interested reader. It should be noted that the forces are nonlinear and that the force calculation given in [11] has uncertainty, so any theoretical calculation of the fluid forces should be reinforced with experimental tests for a specific design if possible. The loop-scale testbed utilizes the same radial bearing geometry (see Figure 5) as the bench-scale testbed, and the optimized radial bearing geometry parameters are given in Table 2.

Table 2. Radial Bearing Geometry

Parameter	Value	Units	Description
x_0	0.0015	m	Air Gap
i_0	8.0	A	Bias Current
d_r	0.066	m	Rotor OD
h_t	0.030	m	Tooth Height
w_t	0.0129	m	Tooth Width
h_s	0.100	m	Stack Height
N	167	turns	Total Coil Turns
α	22.5°	deg	Tooth Angle

Figure 8 shows the theoretical nonlinear force characteristics of the radial bearing differential drive design calculated using the material properties of M19 electrical steel, which is used for fabricating the rotor and stator lamination for the radial bearings. From [14], linearizing (29) about the operating points $x = 0$ and $u_i = 0$ yields the expression of the bearing force given by

$$F_l = k_i i + k_x x, \tag{9}$$

where

$$k_i = \frac{4ki_0}{x_0^2}, \tag{10}$$

$$k_x = \frac{4ki_0^2}{x_0^3}. \tag{11}$$

For this radial bearing design, $k_i = 126.3$ and $k_x = 673,539$. Note that the number of windings achieved in the radial bearing coils is 154, as opposed to the anticipated 160 turns for the radial winding, so the linearized coefficients for the loop-scale testbed are slightly lower than those given in [8].

Figure 9 shows a rendered exploded view of the radial bearing design.

[†]Most of the material in this section has been taken from [8].

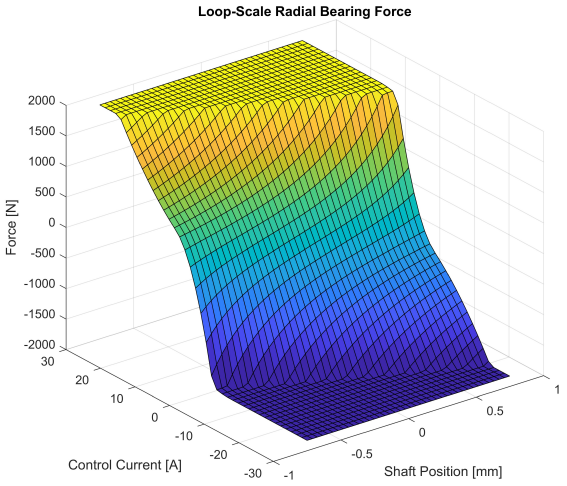

Figure 8. Radial bearing nonlinear force over the bearings operational coil current and shaft position.

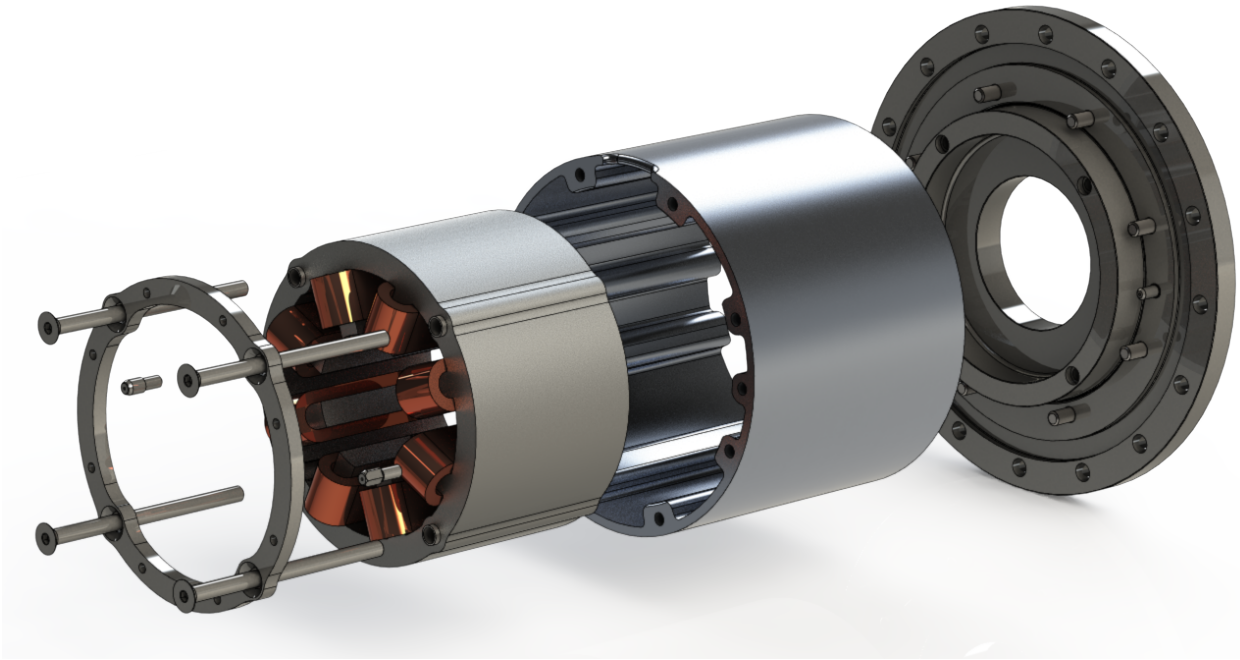

Figure 9. Exploded view of the axial magnetic bearing.

The axial bearing design will have two concentric annulus surfaces on the stator for the flux to pass through to the rotor. To maximize the magnetic flux, the area of both annuli should be equal. In addition, we would like to separate the outer diameter of the smaller annulus and the inner diameter of the larger annulus by a gap larger than the thrust bearing air gap to reduce the magnetic forces between them and prevent a short circuit of the magnetic flux.

For the loop-scale testbed, we will choose a r_o = 43 mm, r_o^m = 34.2 mm, r_i^m = 32.2 mm, and r_i = 17 mm for a 2 mm gap. Figure 10 shows a typical cross section of the thrust bearing design. This diameter value

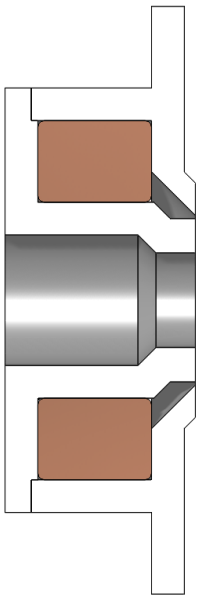

Figure 10. Thrust bearing cross-sectional geometry.

gives a cross-sectional area of 2350 mm^2. Assuming a maximum flux density B_{max} of 1.4 T, the maximum force that can be created by the impeller side axial magnetic bearing is

$$F_{max} = \frac{B_{max}^2 A_T}{\mu_0} = 3328\ N, \tag{12}$$

and the number of windings N_T to achieve the maximum magnetic flux is

$$N_T = \frac{2B_{max} z_0}{\mu_0 u_i} = 334\ turns, \tag{13}$$

where z_0=1.5 mm is the nominal air gap and u_i = 10 A is the nominal coil current. With 16 AWG wire with a cross-sectional area of 1.3 mm^2 and a packing factor of 0.6, the required winding area is 868 mm^2.

With a bias current of 3.5 A and an air gap of 1.5 mm, the thrust bearing has the linearized coefficients

$$k_i = 465.4, \tag{14}$$

$$k_x = 1085963. \tag{15}$$

Figure 11 shows an exploded view of the final thrust bearing design.

Figure 12 shows the nonlinear force characteristics of the axial bearings over their operating ranges calculated using the magnetic properties of 410 grade stainless steel.

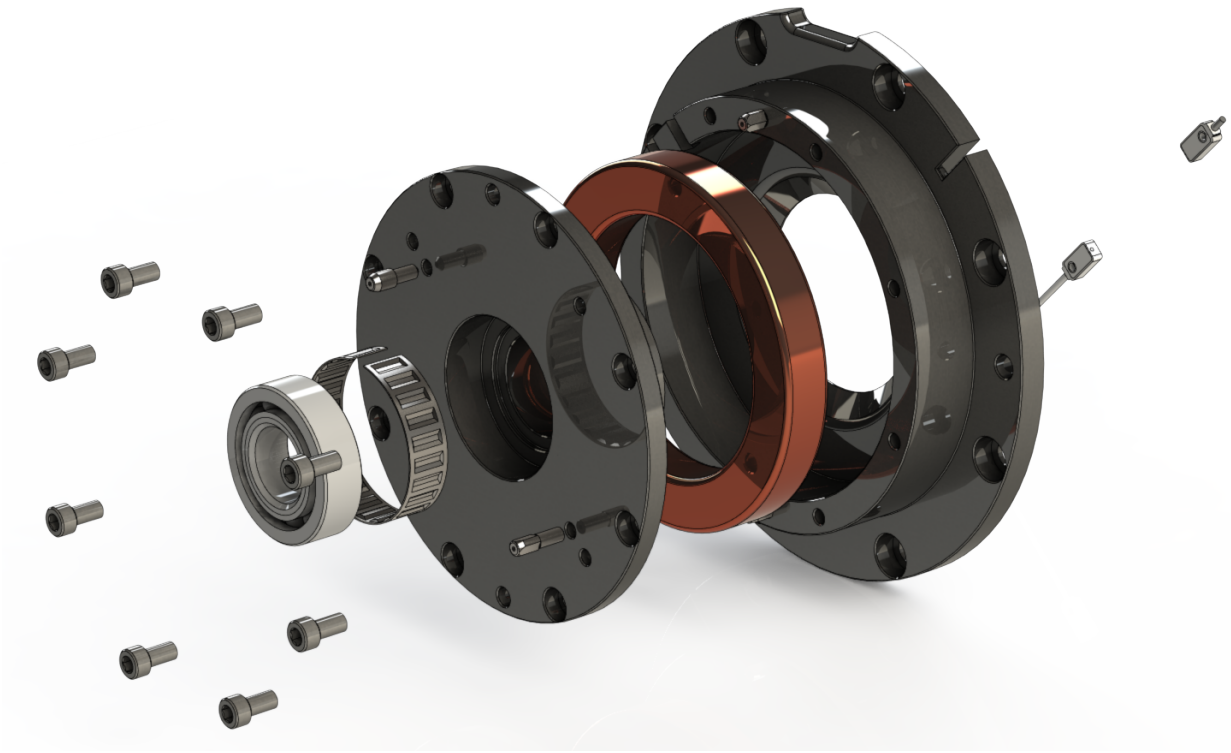

Figure 11. Exploded view of the thrust bearing.

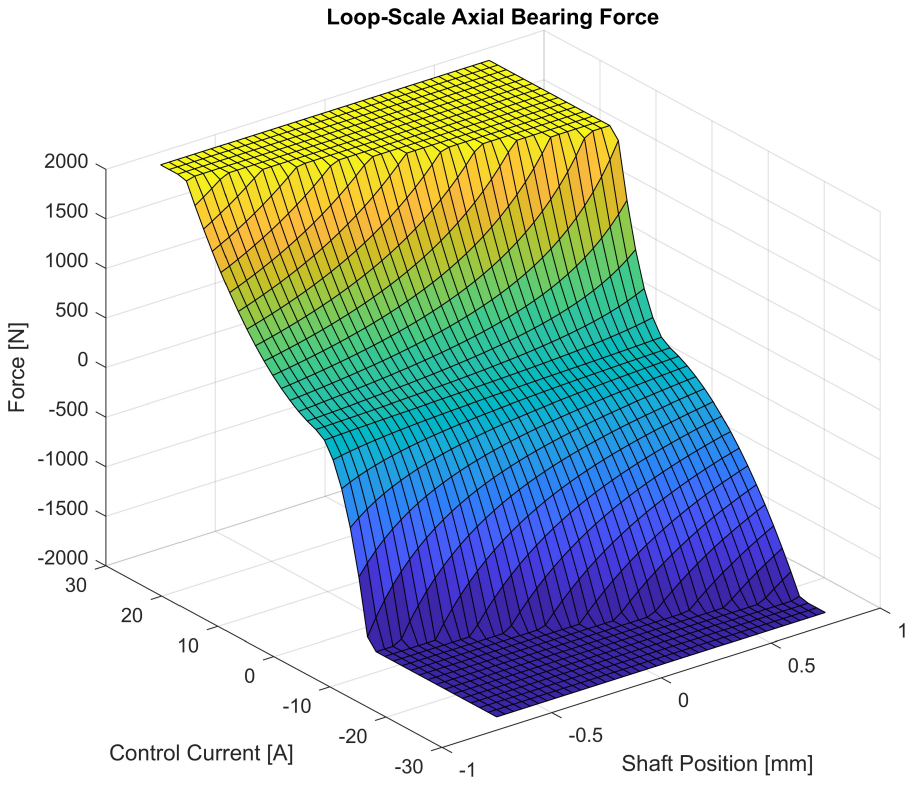

Figure 12. Axial bearing force as a function of current and shaft position.

2.3 Sensors and Power Electronics[‡]

Stable levitation of the testbed shafts using the magnetic bearings requires a precise, high-bandwidth measurement of the shaft position. The shaft position and tilt are measured using a physical sensor in a differential mode to remove any sensor bias from the measurement. Orthogonal radial measurements and an axial measurement are taken at each end of the shaft. For measuring the shaft position, inductive sensors were chosen over capacitive, lasers metrology, and other non-contact sensor techniques. Inductive sensors offered sufficient resolution, accuracy, repeatability, noise rejection, and insensitivity to the target material in a convenient form factor and reasonable price. The specific sensors selected for the bench-scale testbed are the Baumer IR12.D06S-11123877 shown in Figures 13 and 14. Table 3 gives characteristics of the sensors.

Table 3. Sensor Technical Specification

General Data	
Mounting type	quasi-flush
Measuring distance Sd	$0 \cdots 6$ mm
Resolution	$<$ 0.005 mm (static)
	$<$ 0.01 mm (dynamic)
Repeat accuracy	$<$ 0.01 mm
Linearity error	$\pm 720\ \mu$m (S=$0 \cdots 6$ mm)
	$\pm 300\ \mu$m (S=$1.5 \cdots 4.5$ mm)
Temperature drift	± 6 (Full Scale; $-25 \cdots +75^{\circ}C$)
	± 4 (Full Scale; $0 \cdots +60^{\circ}C$)
Electrical Data	
Response time	$<$ 1 ms
Voltage supply range $+Vs$	$12 \cdots 36$ VDC
Current consumption max. (no load)	10 mA
Output circuit	voltage output
Output signal	$0 \cdots 10$ VDC
Load resistance	$>$ 4000 Ohm
Short circuit protection	yes
Reverse polarity protection	yes
Mechanical Data	
Type	cylindrical threaded
Housing material	brass nickel plated
Dimension	12 mm
Housing length	50 mm
Connection types	connector M12
Ambient Conditions	
Operating temperature	$-25 \cdots +75^{\circ}C$
Protection class	IP67

[‡]Most material in the section has been taken from [8] and [9].

Figure 13. Baumer: inductive sensor IR12.D06S-11123877.

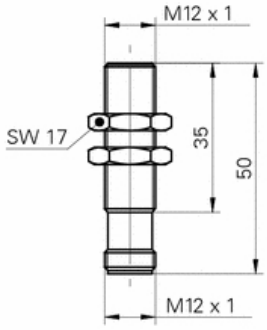

Figure 14. Baumer: inductive sensor dimension drawing.

The loop-scale magnetic bearing pump also utilizes the Baumer IR12.D06S inductive sensor for the radial shaft positions. The excellent performance of the sensors in the bench-scale testbed was one consideration for their use. Another consideration is that the sensor must operate continuously submerged in water in the loop-scale testbed. The Baumer IR12.D06S sensors are IP67 rated, which can withstand submersion at up to 1 m in depth. While this is not sufficient for operation in the loop-scale testbed, it is higher than many other inductive sensors, and in consultation with Baumer, it was determined that additional waterproofing of the sensor would allow continuous submerged operation in the loop-scale testbed.

The form factor of the Baumer IR12.D06S sensor makes using it for the axial measurement difficult, so a Baumer IWFM 08U9501 sensor was chosen. Figure 15 shows the IWFM sensor dimensions.

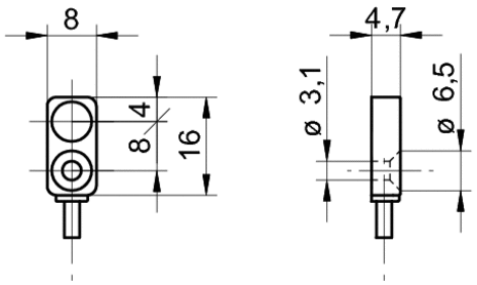

Figure 15. Baumer IWFM: inductive sensor dimension drawing.

The Baumer IWFM sensor technical specifications are given in Table 4.

Figure 16 shows the location of the axial sensors. At this location their target is the thrust bearing rotor.

The Baumer IWFM sensors also have an IP67 rating and were modified with further waterproofing.

To simplify operation and reduce project costs, the power electronics unit developed is utilized by both the bench-scale and loop-scale magnetic bearing testbeds. The power electronics for AMB consists of four power supplies, two RSP 2000-24's used for the X-axis and Y-axis, one RSP 750-24 used for Z-axis, and one RS 15-24 used for the sensors. The specifications for these power supplies are tabulated in Tables 5, 6, and 7. The RSP's power supplies are connected to Pololu High-Power Motor Driver 36v20 CS, with its specifications in Table 8, which outputs the commanded voltages to the coils while feeding back the current sensing after receiving the Pulse Width Modulation(PWM) from the SpeedGoat© real-time computer (see Table 9).

Additional information on the power electronics wiring diagrams can be found in [9].

Table 4. Baumer IWFM Position Sensor Technical Specification

General Data	
Mounting type	quasi-flush
Measuring distance Sd	$0 \cdots 2$ mm
Resolution	< 0.001 mm (static) < 0.005 mm (dynamic)
Repeat accuracy	< 0.02 mm
Linearity error	$\pm 100\,\mu$m
Temperature drift	$\pm 5\%$
Electrical Data	
Response time	< 1 ms
Voltage supply range $+Vs$	$15 \ldots 30$ VDC
Current consumption max. (no load)	10 mA
Output circuit	voltage output
Output signal	$0 \ldots 10$ VDC
Load resistance	> 3000 Ohm
Short circuit protection	yes
Reverse polarity protection	yes
Mechanical Data	
Type	cylindrical threaded
Housing material	brass nickel plated
Dimension	8 mm
Housing length	16 mm
Connection types	cable
Ambient Conditions	
Operating temperature	$10 \cdots + 60\ ^{\circ}C$
Protection class	IP67

Table 5. RSP 2000-24: 2000W Single Output Power Supply Specification

Specification		
Output	DC Voltage	24 V
	Rated Current	80 A
	Current Range	0–80 A
	Rated Power	1920 W
	Voltage ADJ. Range	21–28 V
Input	Voltage Range	90–264 VAC 127–370 VDC
	Frequency Range	47–63 Hz
	Efficiency	90.5%
	AC Current	16A/115 VAC 10A/230 VAC
	Leakage Current	<2 mA/240 VAC

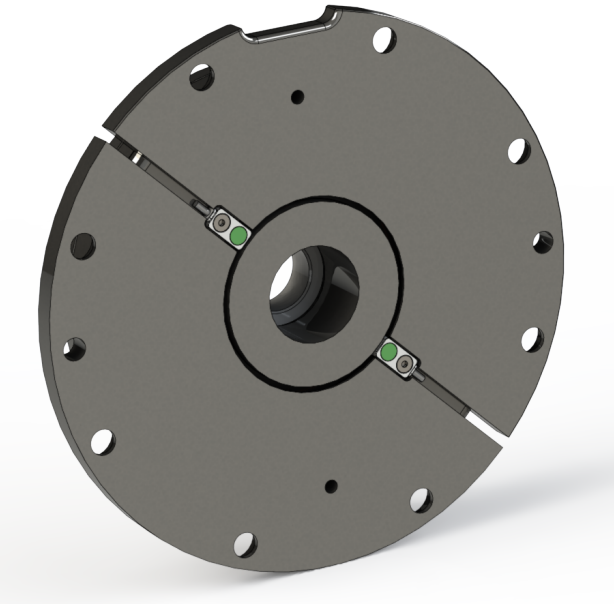

Figure 16. Location of the axial position sensors on the magnetic thrust bearing.

Table 6. RSP 750-24: 750W Single Output Power Supply Specification

Specification		
Output	DC Voltage	24 V
	Rated Current	31.3 A
	Current Range	0–31.3 A
	Rated Power	751.2 W
	Voltage ADJ. Range	20–26.4 V
Input	Voltage Range	90–264 VAC 127–370 VDC
	Frequency Range	47–63 Hz
	Efficiency	90.5%
	AC Current	8.2A/115 VAC 3.9A/230 VAC
	Leakage Current	<2 mA/240 VAC

3 LOOP-SCALE TESTBED ASSEMBLY

Simultaneously, the components for the loop-scale testbed were being fabricated, the magnetic bearing coils were being built, and the wiring harnesses were created and waterproofed. The connector feedthroughs and sensors also received additional waterproofing. Special care was taken in the fabrication of the magnetic bearing coils to maximize their structural properties and minimize their inductance. The coils were designed to be freestanding to save the space that a bobbin would take up. A split-core bobbin was fabricated, as shown in Figure 17.

The removable sides and the split core allow the coil to be easily removed from the bobbin. The split core

Figure 17. Bobbin for winding the loop-scale magnetic bearing radial coils.

Table 7. RS 15-24: 15W Single Output Switching Power Supply Specification

Specification		
Output	DC Voltage	24 V
	Rated Current	0.625 A
	Current Range	0–0.625 A
	Rated Power	15 W
	Voltage ADJ. Range	22–27.6 V
Input	Voltage Range	85–264 VAC 120–370 VDC
	Frequency Range	47–63 Hz
	Efficiency	82%
	AC Current	0.35 A/115 VAC 0.25 A/230 VAC
	Leakage Current	<2 mA/240 VAC

Table 8. Pololu High-Power Motor Driver 36v20 CS Specification

General specifications	
Motor channels	1
Size	1.8 in. x 1.2 in.
Weight:	7 g
Minimum operating voltage	5.5 V
Maximum operating voltage	50 V
Continuous output current per channel	20 A2
Current sense	0.066 V/A3
Maximum PWM frequency	40 kHz
Maximum logic voltage	5.5 V
MOSFET on-resistance (max per leg)	4.8 $m\Omega$
Reverse voltage protection	N

is important because the sides of the coil are parallel. To maintain structural integrity and electrical isolation, strips of paper were placed around the bobbin and between every layer of the coil. The coil was then coated in epoxy on each layer to form a composite structure. Two epoxies were tested, Loctite© ES-1001 and E-00CL. Loctite© ES-1001 is a low-viscosity structural sealant for electronics that can withstand temperatures of up to 104 °C and has a dielectric strength of 1100 V/mil. E-00CL is a more viscous epoxy that can withstand temperatures of up to 82 °C and has a dielectric strength of 16,000 V/mil. Figure 18 shows a coil curing on the bobbin after winding encapsulated with ES-1001, and Figure 19 shows the same coil after removal from the bobbin.To prevent the epoxy from adhering to the bobbin, it was treated with mold release wax between every use.

While the ES-1001 epoxy is superior in its strength, penetration, and temperature characteristics, it needs to harden overnight before it can be removed from the bobbin. The E-00CL has superior dielectric strength and can be removed from the bobbin after 1 hour. These two factors led to the choice of E-00CL as the structural epoxy. In addition to the structural benefits of the epoxy, it also serves as another layer of waterproofing for the submerged coils. The coils achieved a packing factor of 0.67, which was slightly

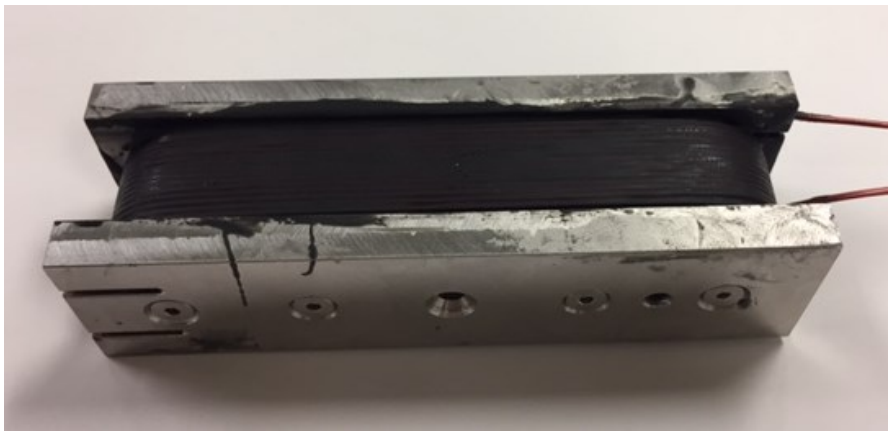

Figure 18. Radial coil still on the bobbin with ES-1001 epoxy encapsulant.

Figure 19. Radial coil after removal from the bobbin with ES-1001 epoxy encapsulant.

Table 9. Speedgoat: Performance Real-Time Target Machine Specification

Main Board	CPU
Processor	Intel Core i7-3770K 3.5 GHz
Chipset	Intel C216 Express
Bus	PCI, 32-bit/33MHz
Graphics	Intel HD Graphics 400P onboard
USB	4 x USB 3.0 and 1 x USB 2.0 at front
	6 x USB 2.0 internal
Ethernet	2 x Gigabit at front
Serial Ports	1 x RS232/422/485 at front
(for baud rates up to 115kb/s only)	1 x RS232/422/485 and 4 x RS232 internal
Memory	4096 MB
BIOS	American Megatrend Inc. (AMI) BIOS
Drives	
Main drive (C:)	250 GB Solid State Drive
Power	
Power inlet	AC 100–240 V, 50/60 Hz, at rear
Power switch	at rear
Secondary power switch	at front
Reset button	none (secondary power switch)
Power LED	at front (combined with secondary power switch)
Environment	
Temperature	0° to $+60^\circ C$ (operating)
Humidity	10–90%, noncondensing
Software	
OS / RTOS	FreeDOS / Simulink Real-Time kernel, preinstalled on CompactFlash
	or Hard Disk for current release of MathWorks software
Development computer	Utilities for kernel transfer,
	I/O drivers and Simulink test models for your selected I/O modules

below the theoretical maximum of 0.68 due to the space taken by the insulating paper between layers.

After consulting with the position sensor manufacturer, epoxy was added to any points where water might ingress into the sensors electronics to waterproof the positions sensors. IP69k sensor cables were purchased so that they would remain watertight when submerged. As an additional layer of protection, dielectric grease was used inside the connector socket in case any water did enter. Additionally, where the outer cable sheath was removed to access the individual wires, that location was sealed in epoxy to prevent any migration of water down the inside of the cable sheath. Figure 20 shows the radial bearing after assembly and wiring. Kevlar thread was used to weave the wiring harness together. To waterproof the internal lug connectors in the magnetic bearings, a heat shrink tubing was used that contains an internal heat-activated epoxy to seal around the connectors after final wiring. Then an additional layer of rubberized plastic was sprayed onto the magnetic bearing electrical components. The preliminary testing of

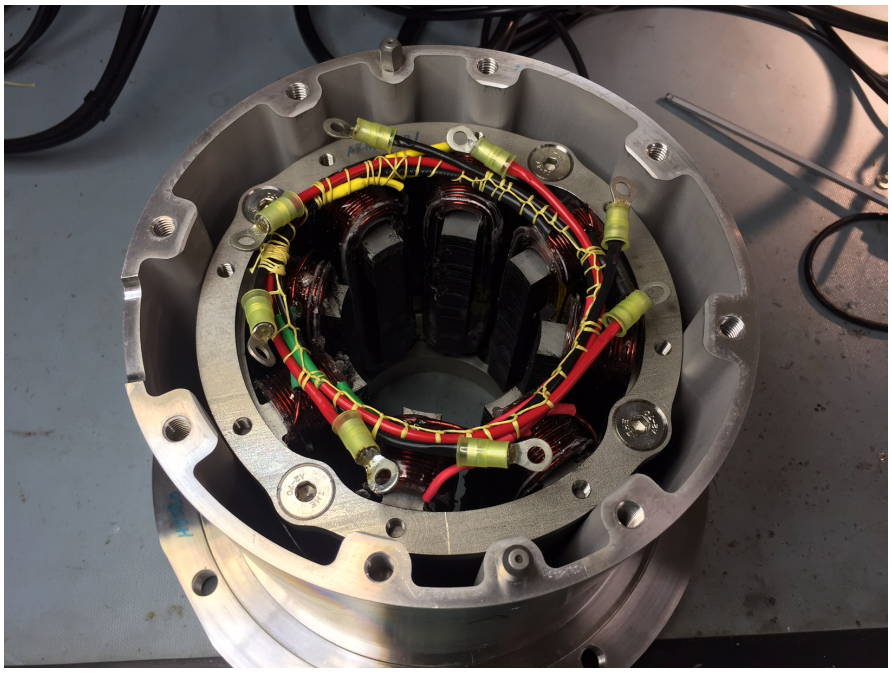

Figure 20. Radial bearing after wiring the coils.

the control algorithms was done before the final waterproofing in case modifications needed to be made. The assembled loop-scale testbed before final waterproofing is shown in Figure 21. Finally, the mount for the pump, the plumbing to integrate it with the water test loop, and the test loop for operational testing are shown in Figure 22.

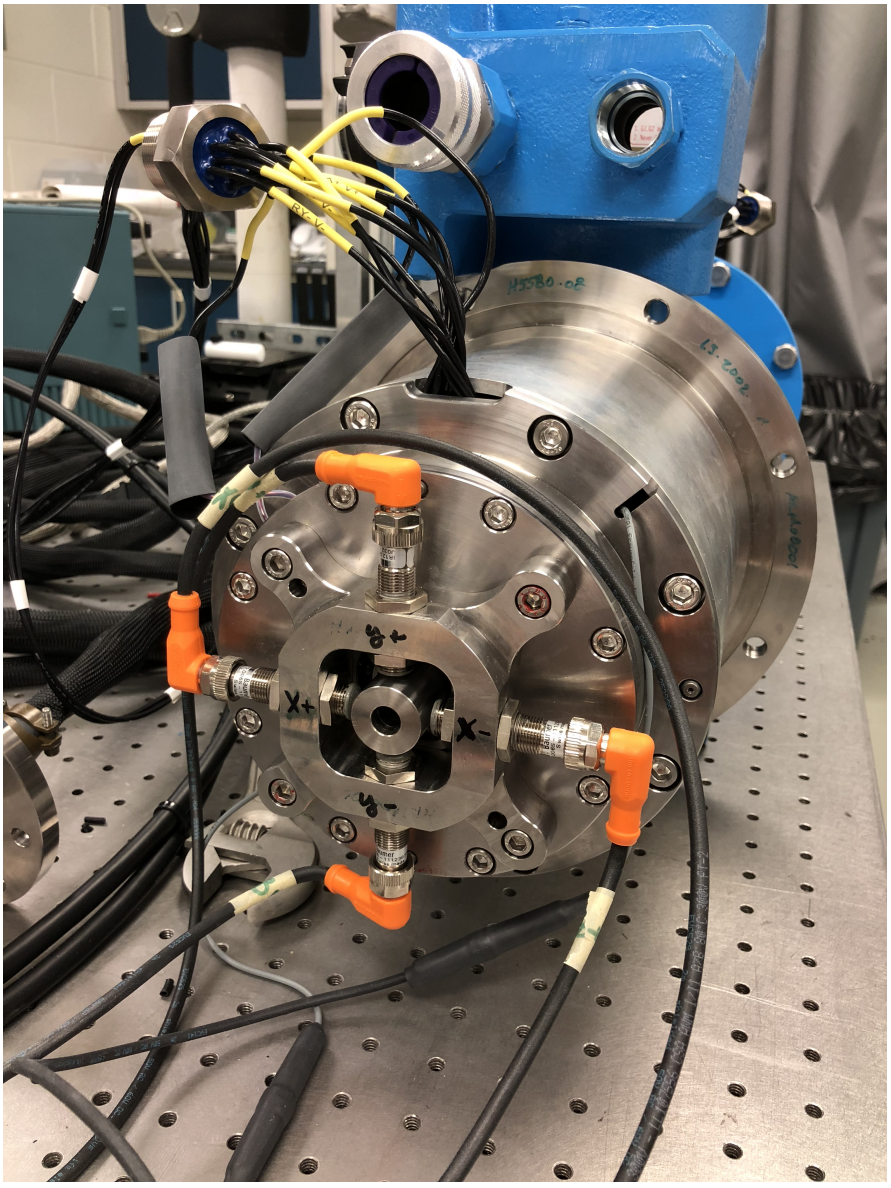

Figure 21. Assembled loop-scale testbed before final waterproofing.

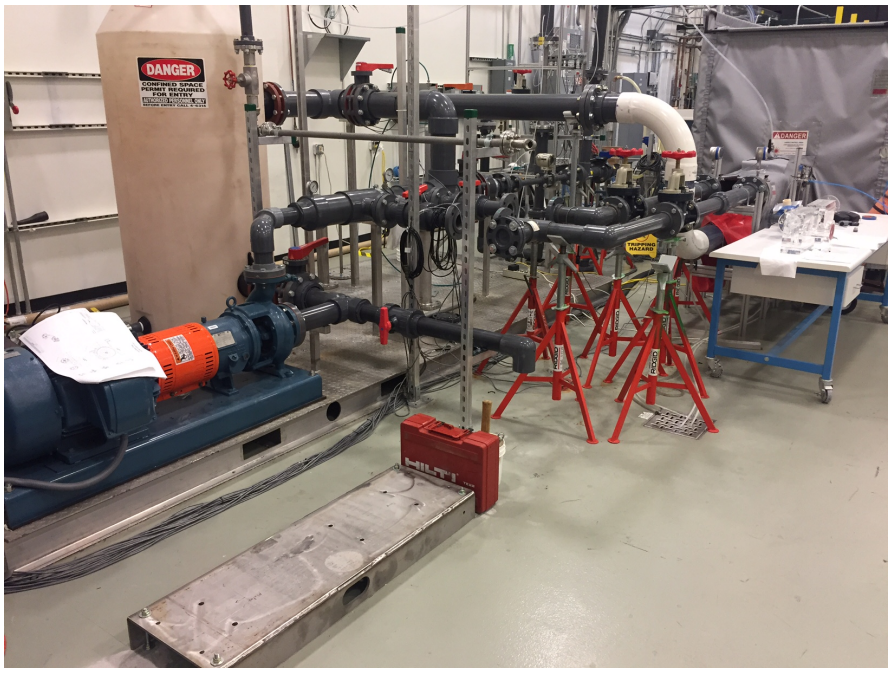

Figure 22. Loop-scale testbed mount and water test loop.

4 SYSTEM MODELS

The fundamental physics that describes the dynamics of magnetic bearings is well understood; however, most references on magnetic bearings do not have detailed derivations of the coupled differential equation model. Typically, a simplified derivation of the system dynamics is presented with the goal of developing a decoupled linearized model of the system. In many situations, this decoupled linearized model is sufficient. The benefit of the decoupled linearized model is that it greatly simplifies the design of the magnetic bearing controller. For many applications of magnetic bearings, this simplified model is sufficient. However, for more challenging operating conditions such as this high-temperature application, a model of the system that more accurately captures the dynamics is needed. For example, the loop-scale testbed has a small fluid-filled gap between the rotor and stator, which develops nonlinear forces on the shaft that are a function of the shaft position. These forces couple the motion of the axes, so the decoupled model is no longer sufficient.

A detailed derivation of magnetic bearing models from the fully nonlinear model to the decoupled linearized model also presents a reference for nonlinear control design, state estimation, and sensorless magnetic bearing control using the less restrictive intermediate models developed. We are not aware of models that are developed with independent coils, which can provide some benefits for nonlinear state estimation, particularly for transient situations and during initial stabilization of the magnetic bearing controller.

4.1 Nonlinear System Model

We develop in this section the full nonlinear system model for a single-axis magnetic bearing. The two fundamental systems are the mechanical motion of the shaft and the electromagnetic response of the coil.

The basic equations for these two systems are

$$m\ddot{s}(t) = f(t), \tag{16}$$

$$v(t) = Ri(t) + N\frac{d\Phi}{dt}, \tag{17}$$

where $s(t) > 0$ is the distance between the shaft and the electromagnet, also known as the air gap, $f(t)$ is the force on the shaft, $v(t)$ is the voltage applied to the coil, $i(t)$ is the current in the coil, $\Phi(t)$ is the magnetic flux in the coil, m is the mass of the shaft, R is the induction of the coil, and N is the total number of turns in the coil winding. Ignoring fringe effects, eddy currents, magnetic saturation and hysteresis, and assuming a uniform spatial flux distribution, we know that the magnetic flux of a magnetic circuit is

$$\Phi = \frac{\mu_0 ANi(t)}{(2s(t) + \frac{l}{\mu_r})}, \tag{18}$$

where $\mu_0 = 4\pi \times 10^{-7}$ is the magnetic permeability of air, A is the cross-sectional area of the core and air gap (assuming the area remains uniform around the magnetic circuit), N is the total number of turns in the coil winding, l is the flux path length in the magnetic core, and μ_r is the relative magnetic permeability of the core material. Typically, for ferromagnetic materials the term l/μ_r is small compared to $2s(t)$ and is neglected. The total derivative of $\Phi(i, s)$ can be calculated by

$$\frac{d\Phi}{dt} = \frac{\partial\Phi}{\partial s}\frac{ds}{dt} + \frac{\partial\Phi}{\partial i}\frac{di}{dt}, \tag{19}$$

$$= -2\frac{\mu_0 ANi(t)}{(2s(t) + \frac{l}{\mu_r})^2}\frac{ds}{dt} + \frac{\mu_0 AN}{(2s(t) + \frac{l}{\mu_r})}\frac{di}{dt}. \tag{20}$$

Magnetic bearings do not typically have conductors in their rotors to interact with the magnetic field through Lorentz forces. Magnetic bearings instead operate using the reluctance force created by the regions of different magnetic permeability. The force is caused by the magnetic flux minimizing the energy stored in the magnetic field. The minimum energy occurs when the air gap $s = 0$. From Maxwell's equations, the energy in the air gap can be expressed as a function of the flux density B and air gap volume V by

$$E = \frac{1}{2}\frac{B^2}{\mu_0}V. \tag{21}$$

The total volume of the air gap V can be calculated by

$$V = 2As. \tag{22}$$

Because work is given by the contour integral

$$W = \int_C F \cdot dx, \tag{23}$$

we will use the principle of virtual displacement (which can be loosely thought of as taking the derivative of Equation (23) over an infinitesimal contour dC) to calculate the force. This relationship is

$$f(t) = \frac{\partial W}{\partial s}, \tag{24}$$

$$= \frac{\partial}{\partial s}\frac{B^2 As}{\mu_0}, \tag{25}$$

$$= \frac{B^2 A}{\mu_0}. \tag{26}$$

Again, by neglecting fringing effects, eddy currents, magnetic saturation, and hysteresis, we can calculate the magnetic flux density B by

$$B(t) = \frac{\mu_0 N i(t)}{2s(t) + \frac{l}{\mu_r}}. \tag{27}$$

Combining Equation (27) with Equation (26) gives the following equation for force as a function of the coil current $i(t)$ and the air gap $s(t)$:

$$f(t) = \mu_0 N^2 A \left(\frac{i^2(t)}{(2s(t) + \frac{l}{\mu_r})^2} \right). \tag{28}$$

4.2 Independent Bipolar Bearing Model

This subsection develops the complete bearing nonlinear model for a bipolar (two opposing electromagnets) magnetic bearing. This presents the most general nonlinear model for a bipolar magnetic bearing (the unipolar model should be evident by inspection), and subsequent sections will deal with the application of simplifying assumptions and the linearization of the model shaft dynamics to arrive at the linearized axis-independent model most commonly used in control design for magnetic bearings.

Generally, we can define the total force created by a bipolar magnetic bearing by applying the nonlinear force Equation (28) to each opposing bearing as follows:

$$f(t) = \mu_0 N_1^2 A_1 \left(\frac{i_1^2(t)}{(2s_1(t) + \frac{l_1}{\mu_r})^2} \right) - \mu_0 N_2^2 A_2 \left(\frac{i_2^2(t)}{(2s_2(t) + \frac{l_2}{\mu_r})^2} \right), \tag{29}$$

where the subscripts 1 and 2 denote the physical parameters for the positive and negative sides of the bipolar magnetic bearing, respectively. This model can be initially simplified based on some nonrestrictive assumptions.

Because the magnetic bearing stators are stationary, we can replace the two dependent air gap terms, $s_1(t)$ and $s_2(t)$, for the two coils with the related shaft position x. Defining the nominal air gap as x_0, the air gaps and shaft position are related by

$$s_1(t) = x_0 - x(t), \tag{30}$$

$$s_2(t) = x_0 + x(t). \tag{31}$$

Generally, a bipolar bearing is designed to be symmetric, so we will assume that $N_1 = N_2$, $A_1 = A_2$, and $l_1 = l_2$. These assumptions are not restrictive for most AMB designs. Furthermore, as will be shown in subsequent sections, small variations in these parameters can be incorporated into a lumped inductance parameter for each magnetic bearing.

For control design, linearization, and gravity compensation, it is useful to define some additional quantities in the model. To capture the gravitational force on the shaft and other constant external forces, we will define a vector h as a constant (possibly unknown) external force. Second, unmodeled dynamics and other noise sources are denoted by $w(t)$.

For the general model we will assume that each coil (positive and negative direction) is independent, with coil currents given by $i_1(t)$ and $i_2(t)$. Typically, the coil currents are forced to be dependent on each other

through the use of a bias current, and this will be addressed in a subsequent section. Using independent coil currents avoids numerical issues with developing Kalman filters to estimate the systems states and could be used to develop magnetic bearing controllers with independent control of each coil.

In radial bearings, the force of the positive and negative bearings is not perpendicular to the bearing axis (see Figure 5). We will denote the angle of force defined by the radial bearing tooth angles in radial bearings by α.

Together Equations (16), (17), (20), and (28) yield the system equations

$$m\ddot{x} = h + w(t) + \mu_0 N^2 A \left(\frac{i_1^2(t)}{(2(x_0 - x(t)) + \frac{l}{\mu_r})^2} \right) \cos\alpha - \mu_0 N^2 A \left(\frac{i_2^2(t)}{(2(x_0 + x(t)) + \frac{l}{\mu_r})^2} \right) \cos\alpha, \tag{32}$$

$$\frac{\mu_0 A N^2}{(2(x_0 - x(t)) + \frac{l}{\mu_r})} \frac{di_1}{dt} = -2 \frac{\mu_0 A N^2 i_1(t)}{(2(x_0 - x(t)) + \frac{l}{\mu_r})^2} \frac{dx}{dt} - R_1 i_1(t) + v_1(t), \tag{33}$$

$$\frac{\mu_0 A N^2}{(2(x_0 + x(t)) + \frac{l}{\mu_r})} \frac{di_2}{dt} = 2 \frac{\mu_0 A N^2 i_2(t)}{(2(x_0 + x(t)) + \frac{l}{\mu_r})^2} \frac{dx}{dt} - R_2 i_2(t) + v_2(t), \tag{34}$$

subject to

$$-x_0 < x < x_0. \tag{35}$$

Rearranging the preceding equations so that some of the terms in the coil equations cancel yields

$$\ddot{x} = \frac{h}{m} + \frac{w(t)}{m} + \frac{\mu_0 N^2 A}{m} \left(\frac{i_1^2(t)}{(2(x_0 - x(t)) + \frac{l}{\mu_r})^2} \right) \cos\alpha - \mu_0 N^2 A \left(\frac{i_2^2(t)}{(2(x_0 + x(t)) + \frac{l}{\mu_r})^2} \right) \cos\alpha, \tag{36}$$

$$\frac{di_1}{dt} = \frac{2 i_1(t)}{(2(x_0 - x(t)) + \frac{l}{\mu_r})} \frac{dx}{dt} - \frac{R_1 (2(x_0 - x(t)) + \frac{l}{\mu_r})}{\mu_0 A N^2} i_1(t) + \frac{(2(x_0 - x(t)) + \frac{l}{\mu_r})}{\mu_0 A N^2} v_1(t), \tag{37}$$

$$\frac{di_2}{dt} = -\frac{2 i_2(t)}{(2(x_0 + x(t)) + \frac{l}{\mu_r})} \frac{dx}{dt} - \frac{R_2 (2(x_0 + x(t)) + \frac{l}{\mu_r})}{\mu_0 A N^2} i_2(t) + \frac{(2(x_0 + x(t)) + \frac{l}{\mu_r})}{\mu_0 A N^2} v_2(t). \tag{38}$$

In this model, the only assumption that is made is that the core permeability μ_r is constant, which implies that the magnetic field in the core does not saturate. These assumptions only hold under certain shaft position and coil current ranges but typically are valid because the bearing core geometry is designed to keep the permeability in the linear range of the magnetic material and the magnetic flux below saturation over the operating range.

4.3 Independent Bipolar Bearing Model without Core Losses

The next common simplification that is made is the assumption that the magnetic permeability of the air gap μ_0 is much greater than the magnetic permeability of the core μ_r. For many electrical steels used in magnetic bearing cores, the permeability of air or vacuum is greater than three orders lower than the electrical steels used. This implies that l/μ_r is usually much smaller than $2x_0$, which allows us to set the

term $l/\mu_r \to 0$. By ignoring the small magnetic core losses, the nonlinear bearing model with independent coils is given by

$$\ddot{x} = \frac{h}{m} + \frac{w(t)}{m} + \frac{\mu_0 N^2 A}{4m}\left(\frac{i_1(t)^2}{(x_0 - x(t))^2}\right)\cos\alpha - \frac{\mu_0 N^2 A}{4m}\left(\frac{i_2(t)^2}{(x_0 + x(t))^2}\right)\cos\alpha, \tag{39}$$

$$\frac{di_1}{dt} = -\frac{i_1(t)}{x_0 - x(t)}\frac{dx}{dt} - \frac{2R_1(x_0 - x(t))}{\mu_0 A N^2} i_1(t) + \frac{2(x_0 - x(t))}{\mu_0 A N^2} v_1(t), \tag{40}$$

$$\frac{di_2}{dt} = \frac{i_2(t)}{x_0 + x(t)}\frac{dx}{dt} - \frac{2R_2(x_0 + x(t))}{\mu_0 A N^2} i_2(t) + \frac{2(x_0 + x(t))}{\mu_0 A N^2} v_2(t), \tag{41}$$

subject to

$$-x_0 < x < x_0. \tag{42}$$

4.4 Simplification of Coil Dynamics

There are two major simplifications commonly made to the coil dynamics. The first is that the coil inductance is constant instead of depending upon the shaft position. The second is that the shaft velocity is zero during stable operation. More formally we assume that $x(t) \approx 0$ and note that the term

$$L = \frac{\mu_0 A N^2}{2x_0} \tag{43}$$

is the nominal coil inductance L. In this model we will assume that the nominal inductances for the positive and negative coils are not identical. This can arise from small variations in the area, the number of windings, or errors in the nominal air gap (due to sensor errors or limitation on the sensor calibration).

Applying these simplifications leads to the system equations

$$\ddot{x} = \frac{h}{m} + \frac{w(t)}{m} + \frac{\mu_0 N^2 A}{4m}\left(\frac{i_1^2(t)}{(x_0 - x(t))^2}\right)\cos\alpha - \frac{\mu_0 N^2 A}{4m}\left(\frac{i_2^2(t))^2}{(x_0 + x(t))^2}\right)\cos\alpha, \tag{44}$$

$$\frac{di_1}{dt} = -\frac{i_1(t)}{x_0 - x(t)}\frac{dx}{dt} - \frac{R_1}{L_1} i_1(t) + \frac{1}{L_1} v_1(t), \tag{45}$$

$$\frac{di_2}{dt} = \frac{i_2(t)}{x_0 + x(t)}\frac{dx}{dt} - \frac{R_2}{L_2} i_2(t) + \frac{1}{L_2} v_2(t). \tag{46}$$

4.5 Simplification of Shaft Motion

Unlike the coil dynamics, assumptions based on the structure of the bipolar magnetic bearings cannot be used to simplify the shaft motion; linearization of the force functions will be the primary tool used to simplify the shaft motion model.

Recall that linearization takes place at a point in the state space x_0, and given a function $f(x)$ of two state variables x_1 and x_2, the function linearized about point $x = (x_{10}, x_{20})$ is given by

$$f(x_1, x_2) \approx f(x_{10}, x_{20}) + \left.\frac{\partial f}{\partial x_1}\right|_{x=(x_{10},x_{20})} (x_1 - x_{10}) + \left.\frac{\partial f}{\partial x_2}\right|_{x=(x_{10},x_{20})} (x_2 - x_{20}). \tag{47}$$

4.5.1 Horizontal Axis Linearization

The horizontal axis does not experience any gravitational forces, so the linearization of the horizontal shaft dynamics is symmetric. It is obvious that the shaft dynamics should be linearized about the operating point $x = 0$, where the shaft is centered between the opposing magnetic bearings. The linearization point for the coil currents is not as obvious from the prior discussion or models. It is common practice to apply a bias current i_0 to bipolar magnetic bearing coils. This has the advantage of linearizing the force/current relationship of the magnetic bearings, which will be explored further in the following section. Another advantage is that it increases the effective stiffness of the magnetic bearing. In this section, however, before we maintain the assumption of independent coil currents and without loss of generality, we will linearize the positive coil about the positive bias current i_{10} and the negative coil about the negative bias current i_{20}. For the horizontal axis we will assume that $h = 0$ so that there is no gravity or other external shaft forces, and for simplicity of presentation, we will assume $w(t) = 0$. Additionally, since the shaft equation is affine in force, to simplify the presentation, we will linearize the positive force and negative force separately.

Positive Coil: First, using the version of the nonlinear shaft equations of motion with two separate coil control currents given by Equation (36), we will linearize the positive coil in the horizontal axis. The coil equation in the positive direction is given by

$$f_+(i_1, x) = k\left(\frac{i_1^2}{(x_0 - x(t))^2}\right), \tag{48}$$

where $k = \frac{1}{4}\mu_0 N^2 A\cos(\alpha)$. We will linearize about the points $i_1 = i_{10} \geq 0$ and $x = 0$. The position is linearized about $x = 0$ because this is the desired stable shaft positions. The current is linearized about a positive current because, as we will show later, the addition of a bias term to the coil currents can linearize the shaft response to changes in current. The first term in the linearization is given by

$$f_+(i_1, x) = f_+(i_1 = i_{10}, x = 0) = k\left(\frac{i_{10}^2}{(x_0 - 0)^2}\right) = k\frac{i_{10}^2}{x_0^2}. \tag{49}$$

The second and third Jacobian terms in the linearization are

$$\left.\frac{\partial f_+}{\partial i_1}\right|_{(i_1=i_{10},x=0)}(i_1(t) - i_{10}) = 2k\left(\frac{i_1(t)}{(x_0 - x(t))^2}\right)\Bigg|_{(i_1=i_{10},x=0)} i_{c1}(t) = 2k\frac{i_{10}}{x_0^2}i_{c1}(t), \tag{50}$$

$$\left.\frac{\partial f_+}{\partial x}\right|_{(i_1=i_{10},x=0)}(x(t) - 0) = 2k\left(\frac{i_1(t)^2}{(x_0 - x(t))^3}\right)\Bigg|_{(i_1=i_{10},x=0)} x(t) = 2k\frac{i_{10}^2}{x_0^3}x(t), \tag{51}$$

where $i_{c1} = i_1 - i_{10}$. So, the complete linearization is

$$f_+(i_{c1}, x) \approx k\frac{i_{10}^2}{x_0^2} + 2k\frac{i_{10}}{x_0^2}i_{c1}(t) + 2k\frac{i_{10}^2}{x_0^3}x(t), \tag{52}$$

$$= k_{10} + \frac{1}{2}k_{i1}i_{c1}(t) + \frac{1}{2}k_{x1}x(t), \tag{53}$$

where $k_{10} = k\frac{i_{10}^2}{x_0^2}$, $k_{i1} = 2k\frac{i_{10}}{x_0^2}$, and $k_{x1} = 2k\frac{i_{10}^2}{x_0^3}$. Note that the lower bound on the linearized coil current i_{c1} is $-i_{10} \leq i_{c1}$.

Negative Coil: Similarly, for the negative coil force given by

$$f_-(i_2, x) = k\left(\frac{i_2(t)^2}{(x_0 + x(t))^2}\right), \tag{54}$$

we will linearize the equation around the points $i_2 = i_{20}$ and $x = 0$. The first linearization term is given by

$$f_-(i_2, x) = f_-(i_2 = i_{20}, x = 0) = k\left(\frac{i_{20}^2}{(x_0 + 0)^2}\right) = k\frac{i_{20}^2}{x_0^2}, \tag{55}$$

and defining the linearized negative coil current as $-i_{c2} = (i_2 - i_{20})$, the Jacobian terms are given by

$$\left.\frac{\partial f_-}{\partial i_2}\right|_{(i_2=i_{20},x=0)}(i_2(t) - i_{20}) = -2k\left(\frac{i_2(t)}{(x_0 + x(t))^2}\right)\Bigg|_{(i_2=i_{20},x=0)} i_{c2}(t) = -2k\frac{i_{20}}{x_0^2}i_{c2}(t), \tag{56}$$

$$\left.\frac{\partial f_-}{\partial x}\right|_{(i_2=i_{20},x=0)}(x(t) - 0) = -2k\left(\frac{i_2(t)^2}{(x_0 + x(t))^3}\right)\Bigg|_{(i_2=i_{20},x=0)} x(t) = -2k\frac{i_{20}^2}{x_0^3}x(t). \tag{57}$$

The reason for the negative sign on the linearized coil current i_{c2} for the negative coil should become clear after the introduction of the bias current and dependent coil currents in Section 4.5.2.

Together, the dynamics of the negative force coil equation is

$$f_-(i_2, x) \approx k\frac{i_{20}^2}{x_0^2} - 2k\frac{i_{20}}{x_0^2}i_{c2}(t) - 2k\frac{i_{20}^2}{x_0^3}x(t), \tag{58}$$

$$= k_{20} - \frac{1}{2}k_{i2}i_{c2}(t) - \frac{1}{2}k_{x2}x(t), \tag{59}$$

where $k_{20} = k\frac{i_{20}^2}{x_0^2}$, $k_{i2} = 2k\frac{i_{20}}{x_0^2}$, and $k_{x2} = 2k\frac{i_{20}^2}{x_0^3}$. Note that the definition of the linearized negative coil control current $i_{c2} = i_{20} - i_2$ and the relationships $i_{20} \geq 0$ and $0 \leq i_2$ imply that the upper bound on the linearized coil current for the negative coil is

$$i_{c2} \leq i_{20}. \tag{60}$$

Combining the two linearized coils, the linearization of Equation (39) where $h = 0$ is given by

$$\ddot{x} = \frac{w(t)}{m} + \frac{f_+}{m} - \frac{f_-}{m}, \tag{61}$$

$$\ddot{x} = \frac{w(t)}{m} + \frac{1}{m}\left(k_{10} + \frac{1}{2}k_1 i_{c1}(t) + \frac{1}{2}k_{x1}x(t)\right) - \frac{1}{m}\left(k_{20} - \frac{1}{2}k_2 i_{c2}(t) - \frac{1}{2}k_{x2}x(t)\right), \tag{62}$$

$$\ddot{x} = \frac{1}{m}\left(w(t) + (k_{10} - k_{20}) + \frac{1}{2}k_i i_{c1}(t) + \frac{1}{2}k_i i_{c2}(t) + \frac{1}{2}(k_{x1} + k_{x2})x(t)\right), \tag{63}$$

$$i_{c1} = i_1 - i_{10}, \tag{64}$$

$$i_{c2} = i_{20} - i_2. \tag{65}$$

The limits on the states in the shaft motion equation are

$$-x_0 < x_{min} \leq x(t) \leq x_{max} < x_0, \quad \forall t, \tag{66}$$

$$-i_{10} \leq i_{c1}(t), \quad \forall t, \tag{67}$$

$$i_{20} \geq i_{c2}(t), \quad \forall t, \tag{68}$$

where x_{min} and x_{max} are the physical constraints on the shaft motion. Enforcing the last two relationships is equivalent to forcing the actual coil currents to always be positive. As an aside, it is very important to enforce, through the design of the magnetic bearing, that the rotor physical motion is strictly limited to being smaller than the nominal air gap. This is normally accomplished through the inclusion of touchdown bearings, which also serve to prevent the rotor and stator from coming into contact (i.e., $x = x_0$ or $x = -x_0$) and to provide a rest for the rotor when the magnetic bearings are not operating. While mechanically enforcing the constraints on the shaft motion is important to prevent damage to the rotor and stator, it also impacts magnetic saturation, simulation, and state estimation. When designing a magnetic circuit for magnetic bearings, it is usually desirable to maintain the magnetic flux in the linear range of the electric steel used in the magnetic cores. As the air gap s between the rotor and stator reduces to zero, the magnetic flux increases by $1/s$, and the magnetic flux rapidly saturates as the air gap goes to zero, so maintaining a small physical separation between the rotor and stator helps keep the magnetic flux in the linear zone. This also impacts simulations of the magnetic bearing. Unless a nonlinear model of the magnetic BH curve for the core material is used in simulating the magnetic flux, when $x \to x_0$ or $x \to -x_0$ this causes divide by zero numerical errors with the simulation. Similarly, this will also cause numerical issues with state estimators both in simulation and application.

Finally, our coil models need to be converted to the new coil currents i_{c1} and i_{c2}. By substitution we have

$$\frac{di_{c1}}{dt} = -\left(\frac{i_{10}(t) + i_{c1}}{x_0 - x(t)}\right)\frac{dx}{dt} - \frac{R_1}{L_1}(i_{10} + i_{c1}) + \frac{1}{L_1}v_1, \tag{69}$$

$$\frac{di_{c2}}{dt} = -\left(\frac{i_{20} - i_{c2}(t)}{x_0 + x(t)}\right)\frac{dx}{dt} + \frac{R_2}{L_2}(i_{20} - i_{c2}) - \frac{1}{L_2}v_2. \tag{70}$$

Similarly, since $v_1 = R_1 i_1$ and $v_2 = R_2 i_2$, we have

$$v_1(t) = R_1 i_{10} + v_{c1}(t) = v_{10} + v_{c1}(t), \tag{71}$$

$$v_2(t) = R_2 i_{20} - v_{c2}(t) = v_{20} - v_{c2}(t). \tag{72}$$

4.5.2 Current Bias

Up until now we have assumed that the coil currents are independent. However, to simplify the system, the coil currents are forced to be dependent on each other. Typically, the positive and negative coils utilize a single coil control current. This dependency can be accomplished in either hardware or software. Another technique that is often employed in conjunction with dependent coil currents is the addition of a bias current to both positive and negative coils. This has many advantages. First, since magnetic bearings create force using magnetic reluctance, they can only create attractive forces (hence the bipolar design of opposing electromagnets). Moving from a positive coil current to a negative coil current will reverse the direction of magnetic flux but will not change the direction of force. A bias current on the magnetic bearings allows the bearings to operate at a non-zero nominal current. If designed correctly, this means that the coil currents never approach the hard force nonlinearity at zero coil current. Second, using the following bias current and a dependent coil control relationship,

$$i_1 = i_0 + i_c, \tag{73}$$

$$i_2 = i_0 - i_c, \tag{74}$$

makes the force/current relationship exactly linear between $-i_0 \leq i_c \leq i_0$ if the inductance of both coils is constant. This linearization is not an approximation of a nonlinear relationship—it is linear in that range. Third, as the bias used increases, the effective stiffness of the magnetic bearing also increases. This can be important for minimizing deflections of the shaft from external disturbances.

Utilizing a coil bias has some downsides. The coils are always operating using higher currents than necessary to counteract forces on the shaft. This causes energy loss and additional Joule heating. Bias currents also decrease the usable current ranges of the power electronics because the nominal current is already some fraction of the maximum current capacity of the power electronics. Finally, the increased apparent stiffness of the magnetic bearing due to bias currents requires a controller with a higher processing speed to obtain the bandwidth needed to operate above the natural frequency of the magnetic bearings.

From Equations (61–65) we can apply the bias current and force dependency between the two magnetic bearing control currents by noting that $i_{10} = i_{20} \triangleq i_0$ and $i_{c1} = i_{c2} \triangle i_c$. This means that

$$k_{10} = k_{20} = k\frac{i_0^2}{x_0^2}, \tag{75}$$

$$k_i = k_1 = k_2 = 2k\frac{i_0}{x_0^2}, \tag{76}$$

$$k_x = k_{x1} = k_{x2} = 2k\frac{i_0^2}{x_0^3}, \tag{77}$$

and Equation (63) can be simplified to the standard single axis linearized magnetic bearing equation by assuming that there is no noise and no external forces h given by

$$m\ddot{x} = k_x x(t) + k_i i_c(x). \tag{78}$$

To apply the bias currents to the independent coil equations, first we note that

$$\frac{k_i}{L} = \frac{2k\frac{i_0}{x_0^2}}{\frac{\mu_0 N^2 A}{2x_0}} = \frac{\mu_0 N^2 A i_0 x_0}{\mu_0 N^2 A x_0^2} = \frac{i_0}{x_0}. \tag{79}$$

Because the coil currents are controlled by varying their voltage, the control current i_c and bias current i_0 can be related to a control voltage v_c and bias voltage v_0 through the coil resistance, which yields

$$v_1(t) = v_c(t) + R_1 i_0 = v_c(t) + v_0, \tag{80}$$

$$v_2(t) = R_2 i_0 - v_c(t) = v_0 - v_c(t), \tag{81}$$

if $R_1 = R_2$.

Next, starting with the equations for the two coil equations using the bias offset and noting that $\frac{d(i_0+i_c)}{dt} = \frac{di_c}{dt}$ since i_0 is constant, we have

$$\frac{di_{c1}}{dt} = \frac{di_c}{dt} = -\frac{i_0 + i_c}{x_0 - x(t)}\frac{dx}{dt} - \frac{R_1}{L_1}(i_0 + i_c) + \frac{1}{L_1}(v_c + v_0), \tag{82}$$

$$\frac{di_{c2}}{dt} = \frac{di_c}{dt} = -\frac{i_0 - i_c}{x_0 + x(t)}\frac{dx}{dt} + \frac{R_2}{L_2}(i_0 - i_c) - \frac{1}{L_2}(v_0 - v_c). \tag{83}$$

Combining Equations (82) and (83), we have

$$2\frac{di_c}{dt} = \left(-\frac{i_0 + i_c}{x_0 - x} - \frac{i_0 - i_c}{x_0 + x}\right)\dot{x} - \frac{R}{L}(2i_c) + \frac{1}{L}(2v_c). \tag{84}$$

Next, we will linearize the coefficient of the shaft velocity term about $i_c = 0$, $x = 0$, and $\dot{x} = 0$. This yields

$$-2\frac{i_0}{x_0}\dot{x}, \tag{85}$$

so, the combined dynamics of dependent coils with a bias current is given by

$$\frac{di_c}{dt} = -\frac{k_i}{L}\dot{x}(t) - \frac{R}{L}i_c(t) + \frac{1}{L}v_c. \tag{86}$$

There are practical issues that arise with the application of a bias current. First, if the individual coil currents are created in the power electronics hardware, the control voltage v_c should be kept in the range $-R_1 i_0 \leq v_c(t) \leq R_2 i_0$. Control voltages outside of this range will reverse the expected direction of the force, which will cause a linear controller to become unstable. If the individual coil voltages are calculated in the controller, they can be digitally saturated so that $v_1(t) \geq 0$ and $v_2(t) \geq 0$. This extends the usable control voltage signal. The next problem is that this single coil model assumes that $R_1 = R_2$, which is often not the case. This means that because the current in each coil is controlled by the same voltage, there will be a current error proportional to the inverse of the error between the measured coil resistance and the actual coil resistance. Another practical problem with voltage control and bias currents is that they can limit the bandwidth of the magnetic bearing coils. The inductance of the magnetic bearing coil defines how quickly the magnetic field and coil current collapse when $v_1 = 0$ or $v_2 = 0$. This uncontrolled transient behavior of the coil current creates an upper limit on the speed at which the coil current and, by extension, bearing force can change. This rate limit on the coil current defines an upper bandwidth that the coil can operate at. If the controller needs to have a higher bandwidth due to the frequencies of the shaft modes or external forces, a stabilizing controller will not exist. In Section 6 we will discuss mitigating the bandwidth challenge due to the force nonlinearities and coil natural bandwidth restrictions. The final issue with the single coil model is that the initial transient behavior of the model cannot match the actual behavior of the system. Initially, both $v_1(0) = 0$ and $v_2(0) = 0$. However, a value of $v_c(0)$ that will satisfy that condition does not exist. Assuming that the initial voltage on both coils is zero from Equation (80), we have $v_c(0) = -R_1 i_0$, and from Equation (81), we have $v_c(0) = R_2 i_0$. Equating the two initial coil voltages we have $-R_1 i_0 = R_2 i_0 \implies -R_1 = R_2$. This can only be true if $R_1 \equiv R_2 \equiv 0$, and since $R_1 > 0$ and $R_2 > 0$, this implies that no v_c exists that can satisfy $v_1(0) = v_2(0) = 0$. Practically, there is an initial transient where the model does not match the physical system. Assuming without loss of generality that $v_c(0) = 0$, then $v_1(t) \to R_1 i_0$ and $v_2(t) \to R_2 i_0$ as $t \to \infty$. The time the model takes to converge is dependent on the inductance L. This mismatch becomes an issue when online state estimation is used. This initial error can cause the Kalman filter to diverge from the true state estimates.

Combined, this leads to a single axis linearized model of a bipolar magnetic bearing given by

$$\dot{x}(t) = \begin{bmatrix} 0 & 1 & 0 \\ \frac{k_x}{m} & 0 & \frac{k_i}{m} \\ 0 & \frac{-k_i}{L} & \frac{-R}{L} \end{bmatrix} x(t) + \begin{bmatrix} 0 \\ 0 \\ \frac{1}{L} \end{bmatrix} u(t). \tag{87}$$

4.5.3 Vertical Axis Gravity Compensation

The vertical axis operates under the effect of gravity. It can be difficult to design a stabilizing controller that can compensate for gravity fast enough to stabilize the shaft, so as an alternative, based on knowledge of the shaft mass, we can add a gravity compensation term to the vertical axis magnetic bearings. In this case,

we need to linearize about a current that counteracts the effects of gravity to remove the bias caused by that term. To begin, we will look at the equilibrium case for the shaft where $\dot{x} = 0$, which implies that $\ddot{x} = 0$. Assuming the expected value of the noise $E[w(t)] = 0$ and ignoring constant external forces other than gravitation so that $h = g$ where g is the acceleration due to gravity, we can rewrite Equation (44) as

$$m\ddot{y} = -mg + k\left(\frac{(i_{10} + i_{c1}(t))^2}{(y_0 - y(t))^2}\right) - k\left(\frac{(i_{20} - i_{c2}(t))^2}{(y_0 + y(t))^2}\right), \tag{88}$$

where, again, $k = \frac{1}{4}\mu_0 N^2 A\cos(\alpha)$ and y_0 is the nominal air gap in the magnetic bearing. Note that i_{10} and i_{20} are not necessarily the same values as they are for the horizontal, but they often are. Also, i_{c1} and i_{c2} are not the same as the horizontal bearings; however, to simplify notation, we will not distinguish between the two cases and leave it to the reader to determine which is meant from the context.

Unlike the horizontal axis, for the vertical axis we next need to find the nominal control current i_g that balances out the gravitational force on the shaft when the shaft is centered at $y = 0$. The gravity compensation force can be applied in two ways:

i) as a bias on the dependent control current and

ii) as a bias on the top coil only.

First Option: For the first case we want to calculate a nominal current i_g that compensates for gravity when the shaft is centered and stationary. In this case, we will assume that we have a dependent coil current or $i_{c1} = i_{c2} \triangleq i_c + i_g$. To compensate for gravity, we will find a current i_g such that when $i_c \equiv 0$, then the force of the magnetic bearings is exactly equal to mg, so setting $\ddot{y} = 0$, $y = 0$, and solving for i_g, we have

$$mg = \frac{k}{y_0^2}\left((i_0 + (i_c + i_g))^2 - (i_0 - (i_c + i_g))^2\right), \tag{89}$$

$$\frac{mgy_0^2}{k} = \left((i_{10}^2 + 2i_{10}i_g + i_g^2) - (i_{20}^2 - 2i_{20}i_g + i_g^2)\right), \tag{90}$$

$$\frac{mgy_0^2}{k} = (i_{10}^2 - i_{20}^2) + 2(i_{10} + i_{20})i_g, \tag{91}$$

$$i_g = \frac{mgy_0^2 - k(i_{10}^2 - i_{20}^2)}{2k(i_{10} + i_{20})}. \tag{92}$$

Furthermore, when $i_{10} \equiv i_{20} \triangleq i_0$, the gravity compensation current i_g can be further simplified to

$$i_g = \frac{mgy_0^2}{4ki_0}. \tag{93}$$

This leads to the gravity compensated shaft force given by

$$f(y, i_c) = -mg + k\left(\frac{(i_0 + (i_c(t) + i_g))^2}{(y_0 - y(t))^2}\right) - k\left(\frac{(i_0 - (i_c(t) + i_g))^2}{(y_0 + y(t))^2}\right). \tag{94}$$

Next, assuming that the positive and negative biases are equal, we will linearize the positive coil about the point $y = 0$ and $i_c = 0$. The first term in the linearization is given by

$$f_+(i_c = 0, y = 0) = k\left(\frac{(i_0 + i_g)^2}{(y_0 - 0)^2}\right) = k\frac{(i_0 + i_g)^2}{y_0^2}. \tag{95}$$

The second and third terms in the linearization are

$$\left.\frac{\partial f_+}{\partial i_c}\right|_{(i_c=0,y=0)}(i_c(t)-0) = 2k\left(\frac{(i_0+i_c(t)+i_g)}{(y_0-y(t))^2}\right)\Bigg|_{(i_c=i_0,y=0)} i_c(t) = 2k\frac{i_0+i_g}{y_0^2}i_c(t), \tag{96}$$

$$\left.\frac{\partial f_+}{\partial y}\right|_{(i_c=0,y=0)}(y(t)-0) = 2k\left(\frac{(i_0+i(t)+i_g)^2}{(y_0-y(t))^3}\right)\Bigg|_{(i_c=0,y=0)} y(t) = 2k\frac{(i_0+i_g)^2}{y_0^3}y(t). \tag{97}$$

$$\tag{98}$$

Next, we will linearize the negative coil about the point $y = 0$ and $i_c = 0$. The first term in the linearization is given by

$$f_-(i_c=0, y=0) = k\left(\frac{(i_0-0-i_g)^2}{(y_0+0)^2}\right) = k\frac{(i_0-i_g)^2}{y_0^2}. \tag{99}$$

The second and third terms in the linearization are

$$\left.\frac{\partial f_-}{\partial i_c}\right|_{(i_c=0,y=0)}(i_c(t)-0) = -2k\left(\frac{(i_0-i(t)-i_g)}{(y_0+y(t))^2}\right)\Bigg|_{(i_c=0,y=0)} i_c(t) = -2k\frac{i_0-i_g}{y_0^2}(i_c(t)), \tag{100}$$

$$\left.\frac{\partial f_-}{\partial y}\right|_{(i_c=0,y=0)}(y(t)-0) = -2k\left(\frac{(i_0-i(t)-i_g)^2}{(y_0+y(t))^3}\right)\Bigg|_{(i_c=0,y=0)} y(t) = -2k\frac{(i_0-i_g)^2}{y_0^3}y(t). \tag{101}$$

$$\tag{102}$$

Combining terms yields

$$m\ddot{y} = -mg + \frac{k}{y_0^2}\left[(i_0^2+2i_0i_g+i_g^2)-(i_0^2-2i_0i_g+i_g^2)\right] \tag{103}$$

$$+ \frac{2k}{y_0^2}\left[(i_0+i_g)+(i_0-i_g)\right]i_c(t) \tag{104}$$

$$+ \frac{2k}{y_0^3}\left[(i_0^2+2i_0i_g+i_g^2)+(i_0^2-2i_0i_g+i_g^2)\right]y(t), \tag{105}$$

$$m\ddot{y} = -mg + \frac{k}{y_0^2}\left[4i_0i_g\right] \tag{106}$$

$$+ \frac{2k}{y_0^2}\left[2i_0\right]i_c(t) \tag{107}$$

$$+ \frac{2k}{y_0^3}\left[2i_0^2+2i_g^2\right]y(t). \tag{108}$$

$$\tag{109}$$

Substituting for i_g we have

$$m\ddot{y} = -mg + mg + \frac{4ki_0}{y_0^2}i_c(t) + \frac{2k}{y_0^3}\left[2i_0^2+2i_{c0}^2\right]y(t), \tag{110}$$

$$m\ddot{y} = k_ii_c(t) + k_yy(t), \tag{111}$$

where

$$k_i = \frac{4ki_0}{y_0^2}, \tag{112}$$

$$k_y = \frac{4k(i_0^2 + i_{c0}^2)}{y_0^3}. \tag{113}$$

$$\tag{114}$$

Second Option: Let's start again with the vertical bearing force

$$m\ddot{y} = -mg + k\left(\frac{(i_0 + i_c(t))^2}{(y_0 - y(t))^2}\right) - k\left(\frac{(i_0 - i_c(t))^2}{(y_0 + y(t))^2}\right), \tag{115}$$

and let i_g be the gravity compensation current so that the vertical equation becomes

$$m\ddot{y} = -mg + k\left(\frac{(i_0 + i_c(t) + i_g)^2}{(y_0 - y(t))^2}\right) - k\left(\frac{(i_0 - i_c(t))^2}{(y_0 + y(t))^2}\right). \tag{116}$$

Now we want to linearize about $i_c = 0$. First, we will find the gravity compensation current at steady state where $y(t) = 0$ and $i_c = 0$ using

$$mg = k\left(\frac{(i_0 + i_g)^2}{y_0^2}\right) - k\left(\frac{i_0^2}{y_0^2}\right), \tag{117}$$

$$\frac{mgy_0^2}{k} = (i_0 + i_g)^2 - i_0^2, \tag{118}$$

$$\frac{mgy_0^2}{k} = (i_0^2 + 2i_0i_g + i_g^2) - i_0^2, \tag{119}$$

$$i_g^2 + 2i_0i_g - \frac{mgy_0^2}{k} = 0. \tag{120}$$

Then, using the quadratic equation, we have the gravity compensation current

$$i_g = \frac{-2i_0 \pm \sqrt{4i_0^2 + 4\frac{mgy_0^2}{k}}}{2}. \tag{121}$$

4.6 Flexible Shaft Model

For systems that employ longer shafts, the flexibility of the shaft can affect the stability and performance of the magnetic bearing controllers if it is not accounted for. Shaft mode shapes also impact the placement of sensors. If a position sensor is placed at an inflection point of a shaft mode shape, it will not be able to measure the shaft position effectively and will cause the magnetic bearing controller to become unstable.

In this section, models of the loop-scale shaft determine the mode shapes and frequencies of the shaft. The model of the shaft dynamics will be determined using finite-element analysis. The basic equation for shaft bending is the Euler-Bernoulli Beam Equation:

$$M = EI\frac{d^2y}{dz^2}, \tag{122}$$

where M is the moment on the shaft, E is Young's Modulus of the beam section, I is the second area moment of inertia of the beam section, z is the distance along the shaft axis, and y is the deflection of the shaft.

To calculate the static and dynamic characteristics of the shaft bending, a custom Matlab© finite-element analysis (FEA) code was developed. The reason for developing the shaft model in Matlab© versus a dedicated FEA package is that the model can easily be in the control design. Because custom code is developed, the code is validated by applying the Euler-Bernoulli equation to both a simple cantilever beam and a simply supported beam to compare the results to the outputs of the custom FEA code. This next part of this section briefly presents the simple beam models used to validate the custom Matlab© FEA code. The next section develops the static FEA model. Next the shaft model with dynamics is developed and used to calculate the resonant frequencies of the shaft. Then the frequency response of the dynamic model is presented along with results for the specific geometry and materials used in the loop-scale shaft.

4.6.1 Validation Models

In this section we will briefly present the models used to validate the custom FEA code. The first model used is the standard cantilever beam with a point source shown in Figure 23.

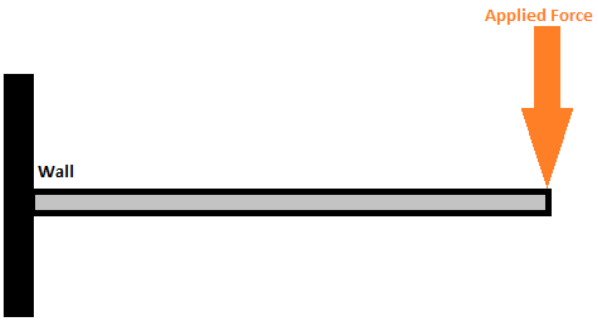

Figure 23. Basic cantilever beam.

Using the Euler-Bernoulli Beam Equation and Newton's second law, the deflection of the beam at any point along its length is given by

$$y(z) = \frac{Fz^2}{6EI}(3L - z), \tag{123}$$

where F is a point force on the end of the cantilever beam and $0 \leq z \leq L$. The slope of the beam at any point z along its length is given by

$$y'(z) = \frac{Fx}{2EI}(2L - x), \tag{124}$$

for $0 \leq z \leq L$. The cantilever support is at $z = 0$, and the force is applied at $z = L$.

The second model used to validate the custom FEA code is a simply supported beam, as shown in Figure 24, which is similar to the model of the loop-scale shaft. For a point force F in the center of the

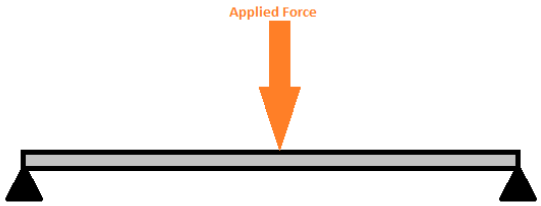

Figure 24. Basic cantilever beam.

simply supported beam with distance L between the supports, the deflection of the beam is given by the equation

$$y(z) = \frac{Fx(3L^2 - 4z^2)}{48EI}, \tag{125}$$

for $0 \leq z \leq L/2$. For $L/2 < z \leq L$, the deflection can be easily calculated by recognizing the symmetry of the deflection.

4.7 Static FEA Model

One quantity of interest in the analysis of the shaft is the deflection under a static load. This is particularly important for a canned-rotor design to verify that the rotor is sufficiently stiff so that it will not contact the stator under a static load. The static FEA begins by deriving a set of stiffness equations for a small beam element. These equations will also form part of the dynamic model of the shaft.

We chose Hermite polynomials as the basis for our FEA elements because they are highly accurate for bending. A diagram of a two-element, three-node FEA model is shown in Figure 25. For the loop-scale

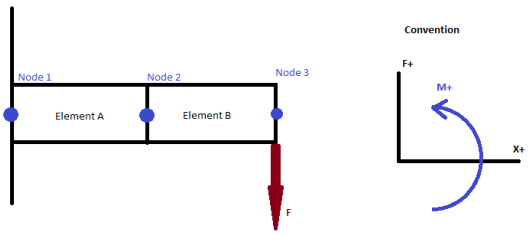

Figure 25. Two-element one-dimensional cantilever beam finite-element setup.

shaft model we will utilize a one-dimensional FEA model. The shaft is symmetric, and any axial motion will be negligible for the loop-scale pump, so a one-dimensional FEA model will provide sufficient accuracy. A one-dimensional model is also chosen because it is more straightforward to integrate with the control design. For a one-dimensional element, there are four states needed to capture the movement of a single element i—the deflections and angles at the left and right nodes of the element.

These are denoted as the state vector

$$\mathbf{x}_i = \begin{bmatrix} v_i \\ \theta_i \\ v_{i+1} \\ \theta_{i+1} \end{bmatrix}. \tag{126}$$

Similarly, the external forces on an element i are forces and moments at the left and right nodes of the elements. These are denoted as

$$\mathbf{F}_i = \begin{bmatrix} f_i \\ M_i \\ f_{i+1} \\ M_{i+1} \end{bmatrix}. \tag{127}$$

Hermite polynomials are used to interpolate the deflection and slope of the element in between the nodes. In matrix form this means that the beam element deflection and slope are given by

$$\mathbf{K}_i \mathbf{x}_i = \mathbf{F}_i, \tag{128}$$

where the stiffness matrix K_i for an element with length l_i is given by

$$\mathbf{K}_i = \frac{EI}{l_i^3} \begin{bmatrix} 12 & 6l_i & -12 & 6l_i \\ 6l_i & 4l_i^2 & -6l_i & 2l_i^2 \\ -12 & -6l_i & 12 & -6l_i \\ 6l_i & 2l_i^2 & -6l_i & 4l_i^2 \end{bmatrix}. \tag{129}$$

To model a beam, it is then broken up into small elements and a block diagonal global stiffness and force matrix is created by summing stiffness matrices that describe the same node. For example, in the two-node cantilever beam model, assuming that both elements have the same length l, the global stiffness matrix is

$$\mathbf{K} = \frac{EI}{l^3} \begin{bmatrix} 12 & 6l & -12 & 6l & 0 & 0 \\ 6l & 4l^2 & -6l & 2l^2 & 0 & 0 \\ -12 & -6l & 24 & 0 & 0 & 0 \\ 6l & 2l^2 & 0 & 8l^2 & 0 & 0 \\ 0 & 0 & -12 & -6l & 12 & -6l \\ 0 & 0 & 6l & 2l^2 & -6l & 4l^2 \end{bmatrix}. \tag{130}$$

After assembling the global stiffness matrix, the forces at each node need to be balanced and any external forces applied. By Newton's second law, the forces and moments at each node cancel out, which leaves only the external force F in the negative direction at the end of the cantilever beam. This leaves the force vector given by

$$\mathbf{F} = \begin{bmatrix} 0 \\ 0 \\ 0 \\ 0 \\ -F \\ 0 \end{bmatrix}, \tag{131}$$

so the overall equation for the static motion of the shaft is

$$\mathbf{Kx} = \mathbf{F} \tag{132}$$

$$\frac{EI}{l^3}\begin{bmatrix} 12 & 6l & -12 & 6l & 0 & 0 \\ 6l & 4l^2 & -6l & 2l^2 & 0 & 0 \\ -12 & -6l & 24 & 0 & 0 & 0 \\ 6l & 2l^2 & 0 & 8l^2 & 0 & 0 \\ 0 & 0 & -12 & -6l & 12 & -6l \\ 0 & 0 & 6l & 2l^2 & -6l & 4l^2 \end{bmatrix}\begin{bmatrix} v_1 \\ \theta_1 \\ v_2 \\ \theta_2 \\ v_3 \\ \theta_3 \end{bmatrix} = \begin{bmatrix} 0 \\ 0 \\ 0 \\ 0 \\ -F \\ 0 \end{bmatrix}, \tag{133}$$

and the solution is given by $\mathbf{x} = \mathbf{K}^{-1}F$. However, the stiffness matrix K cannot be inverted because it is rank deficient. This is because as it is formulated, there are no boundary conditions used in the model. Intuitively, without boundary conditions, this is the same as if the beam were free to move and rotate anywhere. To get a unique solution, we need to use the cantilever beam boundary conditions which are where the deflection and slope at the first node are both zero. One method for applying the boundary conditions is to remove the row and column corresponding to a zero deflection or zero slope condition from the model. They are not set to zero as the K matrix will still be rank deficient and non-invertible. In the case of the two-element cantilever beam, the equations with boundary conditions included are

$$\frac{EI}{l^3}\begin{bmatrix} 24 & 0 & 0 & 0 \\ 0 & 8l^2 & 0 & 0 \\ -12 & -6l & 12 & -6l \\ 6l & 2l^2 & -6l & 4l^2 \end{bmatrix}\begin{bmatrix} v_2 \\ \theta_2 \\ v_3 \\ \theta_3 \end{bmatrix} = \begin{bmatrix} 0 \\ 0 \\ -F \\ 0 \end{bmatrix}. \tag{134}$$

Figure 26 shows the solution to the two-element one-dimensional FEA model of the cantilever beam.

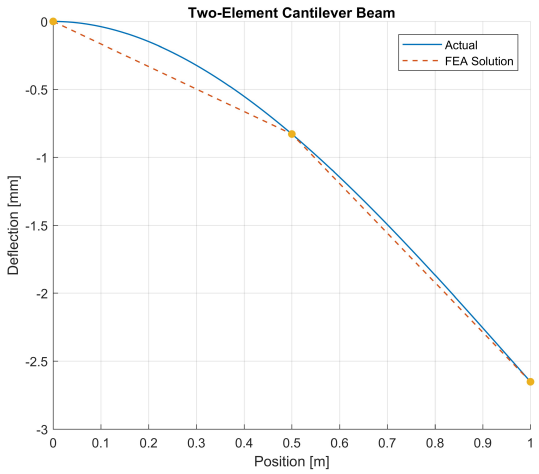

Figure 26. Solution to the two-element cantilever beam FEA to validate the analysis.

Another more general method that allows non-zero initial conditions is to set each row of the stiffness matrix K that corresponds to a nodal boundary condition to zero with the diagonal element set to one. The boundary condition is then inserted into the row of the force matrix F that corresponds to that nodal

boundary condition. For example, if the boundary conditions of the left node are $v_1 = 0.001$ meters and $\theta_1 = 0.002$ radians, then the corresponding equations become

$$\frac{EI}{l^3}\begin{bmatrix} 1 & 0 & 0 & 0 & 0 & 0 \\ 0 & 1 & 0 & 0 & 0 & 0 \\ -12 & -6l & 24 & 0 & 0 & 0 \\ 6l & 2l^2 & 0 & 8l^2 & 0 & 0 \\ 0 & 0 & -12 & -6l & 12 & -6l \\ 0 & 0 & 6l & 2l^2 & -6l & 4l^2 \end{bmatrix}\begin{bmatrix} v_1 \\ \theta_1 \\ v_2 \\ \theta_2 \\ v_3 \\ \theta_3 \end{bmatrix} = \begin{bmatrix} 0.001 \\ 0.002 \\ 0 \\ 0 \\ -F \\ 0 \end{bmatrix}, \tag{135}$$

and the FEA solution to this is shown in Figure 27.

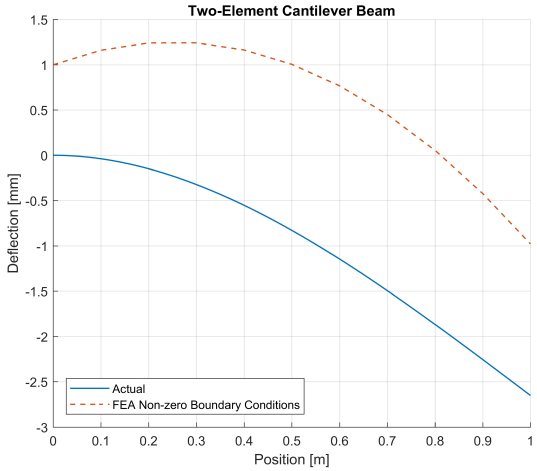

Figure 27. Solution to the two-element cantilever beam FEA with non-zero boundary conditions.

Even with only two elements, the Hermite polynomial–based deflection is exact (numerical error below the floating-point precision). It is also useful to interpolate the deflection between the solution points. We can also use Hermite polynomials for this interpolation. Hermite polynomials are orthogonal polynomials that have the useful property for interpolation that their value and the value of their derivatives up to the order of the polynomial are either one or zero at the end points of the closed interval [0, 1] [2]. The four first-order orthogonal Hermite polynomials used in this analysis are

$$H^1_{01}(s) = 1 - 3s^2 + 2s^3, \tag{136}$$

$$H^1_{11}(s) = Ls(s-1)^2, \tag{137}$$

$$H^1_{02}(s) = s^2(3 - 2s), \tag{138}$$

$$H^2_{12}(s) = Ls^2(s-1), \tag{139}$$

where

$$0 \leq s = \frac{z - z_1}{z_2, z_1} \leq 1, \tag{140}$$

z_1 is the axial position of the element's first node, and z_2 is the axial position of the element's second node. The interpolated deflection is calculated using the boundary conditions of each element by

$$y = H^1_{01}v_i + H^1_{11}\theta_i + H^1_{02}v_{i+1} + H^1_{12}\theta_{i+1}. \tag{141}$$

Figure 28 shows the two-element solution interpolated using five points for each element with Hermite polynomials.

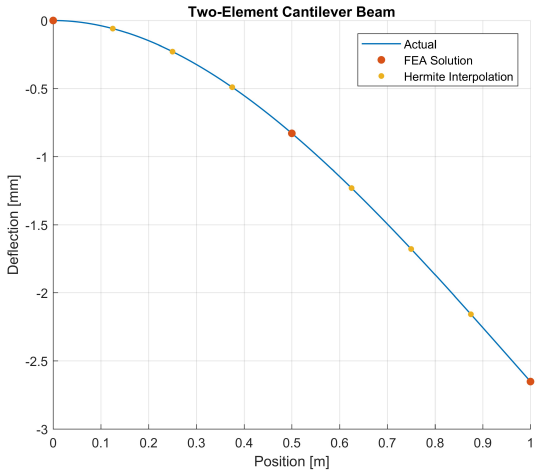

Figure 28. Hermite interpolation of the solution to the two-element FEA solution.

Similar results can be obtained for the simply supported beam. Finally, in this section we will develop a model for the Jeffcott rotor which is the equivalent lumped parameter model for a magnetically suspended shaft with the shaft mass concentrated in a single disk at the center of mass of the shaft. This is the simplest flexible shaft model.

Typically, FEA analysis of shaft vibration assumes that the bearings are infinitely stiff. This assumption is generally valid for mechanical bearings because their stiffness is orders of magnitude higher than the shaft bending stiffness, and so they do not contribute significantly to the deflection of the shaft. In the case of magnetic bearings, their effective stiffness is often lower than the bending stiffness of the shaft and thus contribute to the shaft deflection, modal analysis, and frequency response.

4.8 Modal Analysis

When designing shafts and embedded magnetic bearing controllers for rotating shaft, it is important to be able to model the shaft bending modes and modal frequencies. The model frequencies can cause a resonance when the shaft is rotating at those speeds which will greatly increase the disturbance forces on shaft that the magnetic bearings controller will need to compensate for. Intuitively a stiffer shaft will increase the natural frequencies at which it vibrates. The "stiffness" of the magnetic bearing controller will also impact the shaft vibrational frequencies. When the operating rotational speed of the shaft is higher than the lowest modal frequency of the shaft, the impacts can be mitigated by spending as little time as possible at the model frequencies during the ramp up of the shaft to its operation speed. The other option is to design the magnetic bearing controller to be robust to the worst-case frequency-dependent gain in the shaft modal frequencies that are in the operating range.

Building on the static FEA model from the previous section, we can write the dynamic model of the shaft as the second-order matrix differential equation

$$\mathbf{M}\ddot{\mathbf{y}} + \mathbf{D}\dot{\mathbf{y}} + \mathbf{K}\mathbf{y} = \mathbf{F}, \tag{142}$$

where the overdot notation is the time derivative (i.e., $\dot{x} = dx/dt$), the matrix $\mathbf{M}$ is some mass matrix for the finite-element model, and the $\mathbf{D}$ matrix is some matrix of damping coefficients for the FEA model. There are two sources of damping for typical magnetic bearing applications—external fluid damping and energy dissipation in the shaft material. Most applications involve magnetic bearings because they typically operate in air or vacuum, so they have minimal external damping. The damping from internal energy dissipation in the shaft is also typically small, and theoretical derivation of this damping has large uncertainties. Including damping in the model will decrease the peak amplitude of the vibrations and decrease the values of the modal frequencies. However, the shift in frequencies is generally small compared to the absolute values of the frequencies and often is smaller than the uncertainties in the modal frequencies that arise from nonlinearities and other real-world effects that arise. Furthermore, without damping, the modal amplitudes achieve their worst-case values, so assuming that there is no damping is the worst-case upper bound on the shaft vibrational amplitudes. Hence, for this analysis, we will assume no damping. For high-precision and/or high-speed applications, it is necessary to experimentally determine the mass, damping, and stiffness matrix coefficients so that the controller performance can be improved because of the reduced model uncertainties.

Similarly, to the development of the stiffness matrix $\mathbf{K}$, we can develop a finite-element formulation of the mass matrix $\mathbf{M}$ using Hermite polynomials. This matrix for a single element is given by

$$\mathbf{M}_i = \frac{\mu_i l_i}{420}\begin{bmatrix} 156 & 22l_i & 54 & -13l_i \\ 22l_i & 4l_i^2 & 13l_i & -3l_i \\ 54 & 13l_i & 156 & -22l_i \\ -13l_i & -3l_i & -22l_i & 4l_i^2 \end{bmatrix}, \tag{143}$$

where $\mu_i = \rho_i A_i$, ρ_i is the density of the element, A_i is the cross-sectional area of the element, and l_i is the length of the element.

To determine the modal frequencies of the FEA model, we will analyze the eigenvalues of the homogenous form of the differential equation given by

$$\mathbf{M}\ddot{\mathbf{y}} + \mathbf{K}\mathbf{y} = 0. \tag{144}$$

Recall that the standard form of the eigenvalue equation is given by

$$[\mathbf{A} - \lambda\mathbf{I}]\mathbf{y} = 0, \tag{145}$$

where $\mathbf{A} \in \mathbb{C}^{n\times n}$ is a matrix, $\mathbf{I}$ is an $n \times n$ identity matrix, and $\lambda \in \mathbb{C}^n$ is a vector of the eigenvalues of $\mathbf{A}$. Taking the Laplace transform of (144), we can write it as

$$[\mathbf{K} - \omega_n^2\mathbf{M}]\mathbf{y} = 0. \tag{146}$$

Then pre-multiplying by the inverse of $\mathbf{M}$ we have

$$[\mathbf{M}^{-1}\mathbf{K} - \omega_n^2\mathbf{M}^{-1}\mathbf{M}]\mathbf{y} = 0, \tag{147}$$

$$[\mathbf{M}^{-1}\mathbf{K} - \omega_n^2\mathbf{I}]\mathbf{y} = 0, \tag{148}$$

which is now in the standard eigenvalue form where $\mathbf{A} = \mathbf{M}^{-1}\mathbf{K}$ and $\lambda = \omega_n^2$, so finding the natural frequencies ω_n^2 is equivalent to finding the eigenvalues of $\mathbf{M}^{-1}\mathbf{K}$. The mode shapes corresponding to each natural frequency can also be found by solving the eigenvalue problem

$$\mathbf{A}v = \lambda v, \tag{149}$$

where v are the eigenvectors. The columns of the eigenvectors correspond to the mode shapes.

A common model of the shaft used in magnetic bearing design is a single-element Jeffcott Rotor, as shown in Figure 29. In a Jeffcott rotor, all the mass is concentrated in the center of the shaft and a single bending

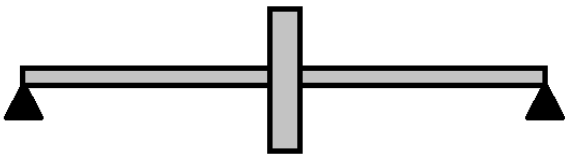

Figure 29. Jeffcott rotor with rigid and flexible bearings.

stiffness is assumed along the shaft. In other words, the Jeffcott rotor assumes a uniform shaft cross section along the length of the shaft. For this model, the natural frequency is equivalent to the scalar case

$$\omega_n = \sqrt{\frac{k}{m}}, \tag{150}$$

where m is a mass and k is a spring constant.

4.8.1 Flexible Bearings

Until now, the boundary conditions assume that supports are rigid. This is a common assumption when analyzing rotordynamics and shaft mode shapes because the stiffness of conventional bearings is high compared to the stiffness of the shaft, so numerically they have little impact on the analysis. However, from the linearized shaft motion Equation (78) we see that the magnetic bearings act as a spring with spring constant k_x. Note that the spring constant $k_x > 0$, so the unforced system is unstable. When analyzing the rotordynamics, the magnetic bearing needs to be stabilized by a feedback controller. The closed-loop spring rate of the system $\overline{k}_x$ should be used in this analysis or the analysis will be indeterminate (K will be singular and thus non-invertible). The closed-loop stiffness of magnetic bearings is lower than the mechanical stiffness of physical bearings and needs to be included in the analysis. This can be accomplished by modifying the stiffness matrix for each element that the magnetic bearing applies force to using the closed-loop magnetic bearing stiffness $\overline{k}_x$ to be

$$\mathbf{K}_i = \frac{EI}{l_i^3}\begin{bmatrix} 12+\overline{k}_x & 6l_i & -12 & 6l_i \\ 6l_i & 4l_i^2 & -6l_i & 2l_i^2 \\ -12 & -6l_i & 12+\overline{k}_x & -6l_i \\ 6l_i & 2l_i^2 & -6l_i & 4l_i^2 \end{bmatrix}. \tag{151}$$

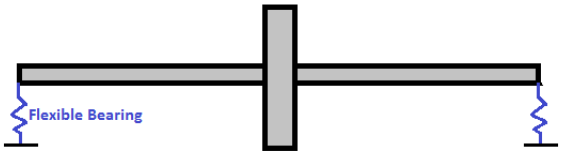

Figure 30. Jeffcott rotor with rigid and flexible bearings.

Figure (30) shows a Jeffcott rotor with flexible magnetic bearings.In this case the shaft natural frequency decreases and can be calculated by

$$\omega_n = \sqrt{\frac{1}{1 + \frac{k}{2\bar{k}_x}}}. \tag{152}$$

The flexible bearings will also change the mode shapes of the shaft. For example, Figure 31 shows the mode shapes of a simply supported beam with rigid supports, and Figure 32 shows the mode shapes of a simply supported beam with flexible supports.

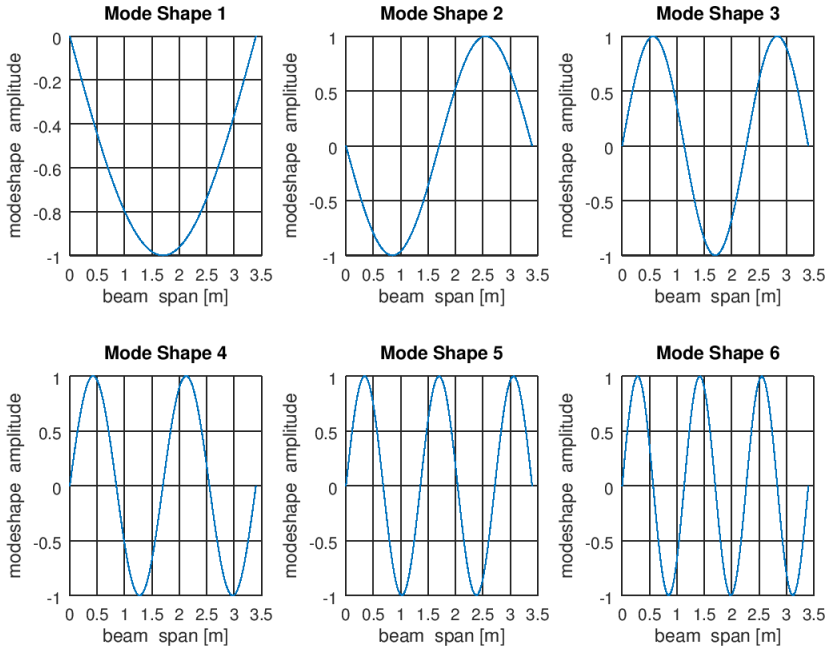

Figure 31. Jeffcott rotor with rigid and flexible bearings.

Without enforcing zero deflection at the supports, the mode shapes for the higher order modes are significantly different.

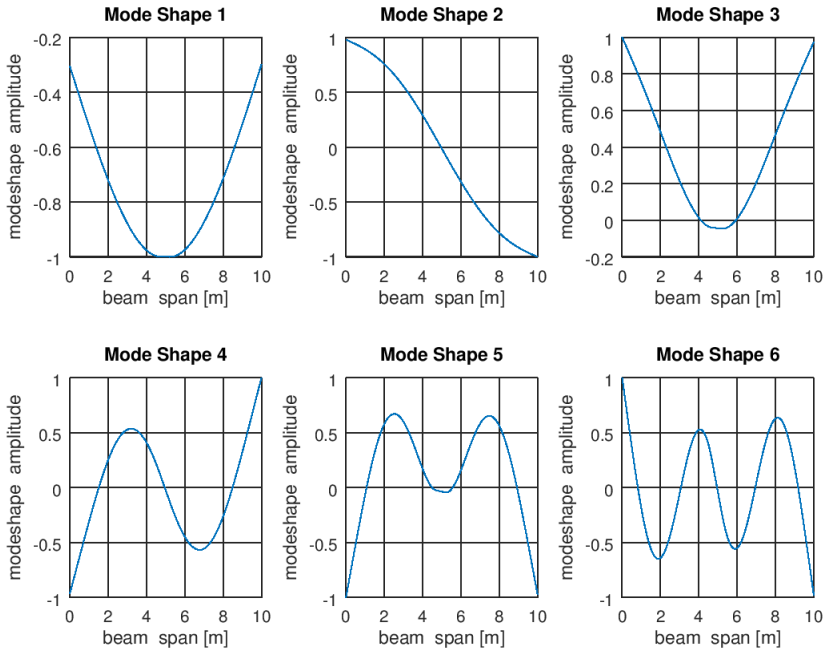

Figure 32. Jeffcott rotor with rigid and flexible bearings.

4.9 Frequency Response

In addition to calculating the modal frequencies, for developing stabilizing controllers that are robust to the flexible modes of the shaft, a more complete frequency response model of the shaft is required. This means modeling the impact of the forces generated by the magnetic bearings on the shaft displacement at points of interest along the shaft like the sensor locations or the impeller. The general model of the shaft bending dynamics is given by

$$\mathbf{M}\ddot{\mathbf{y}} + \mathbf{D}\dot{\mathbf{y}} + \mathbf{K}\mathbf{y} = \mathbf{F}\mathbf{u}, \tag{153}$$

where we have added an input vector u that corresponds to the generalized forces created by the magnetic bearings. In this situation, the matrix F determines what nodes the magnetic bearings apply their force to in the shaft model. Because theoretically determining the damping matrix coefficients is uncertain, we will parameterize the damping matrix as $d\mathbf{I}$, where d is a scalar damping coefficient and $\mathbf{I}$ is an appropriately sized identity matrix. The assumptions that the damping coefficient is scalar and the damping matrix is diagonal arise from the homogeneity of the shaft material and the one-dimensional model of the shaft bending. Because determining the coefficient d is uncertain, we will vary the values of d and determine the sensitivity of the frequency response to changes in the damping coefficient.

To analyze the frequency response, we will take the second-order Equation (153) and convert it to a coupled first-order differential equation. This system is given by

$$\dot{\mathbf{x}} = \mathbf{A}\mathbf{x} + \mathbf{B}\mathbf{u}, \tag{154}$$

$$\begin{bmatrix} \dot{\mathbf{y}} \\ \ddot{\mathbf{y}} \end{bmatrix} = \begin{bmatrix} \mathbf{0} & \mathbf{I} \\ \mathbf{M}^{-1}\mathbf{K} & \mathbf{M}^{-1}\mathbf{D} \end{bmatrix} \begin{bmatrix} \mathbf{y} \\ \dot{\mathbf{y}} \end{bmatrix} + \begin{bmatrix} \mathbf{0} \\ \mathbf{I} \end{bmatrix} \mathbf{u}. \tag{155}$$

Next, we will define an output matrix $\mathbf{C}$ where

$$\mathbf{z} = \mathbf{C}\mathbf{x}. \tag{156}$$

The $\mathbf{C}$ matrix takes the deflections and angles of each node and maps it to a subset of nodes of interest. For example, we would like to understand the frequency response of the shaft node at the location of the position sensors to determine the impact of the rotational frequency on the position measurements. For a single measurement, this would correspond to a $\mathbf{C}$ matrix where $\mathbf{C} = [0, \ldots, 1, \ldots, 0]$ where the location of the one corresponds to the desired measurement. Given the complete model

$$\dot{\mathbf{x}} = \mathbf{A}\mathbf{x} + \mathbf{B}\mathbf{u}, \tag{157}$$

$$\mathbf{z} = \mathbf{C}\mathbf{x}, \tag{158}$$

with $\mathbf{C}$ corresponding to the measurement of a single node, we can take the Laplace transform of the system and calculate the frequency response function. The peaks in the frequency response correspond to the modal frequencies. On a practical note, the practice of removing the rows and columns of the stiffness, mass, and damping matrices used in most FEA analysis will not provide good numerical results. Instead the method of setting the rows to zeros with a one on the diagonal element as shown in Equation (135) will yield better numerical solutions.

The loop-scale magnetic bearing shaft shown in Figure 33 was divided into an FEA model with 64 elements.

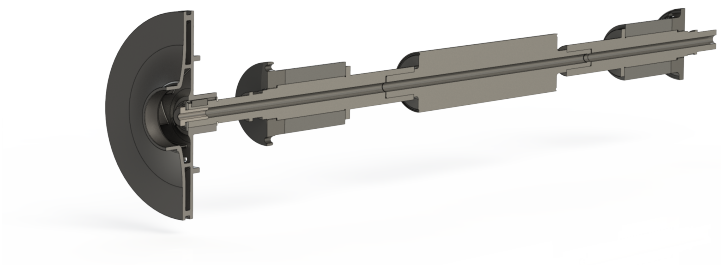

Figure 33. Section view of the loop-scale testbed shaft.

Figure 34 shows the mode shapes of the loop-scale testbed shaft. The total frequency response of the loop-scale testbed shaft is shown in Figure 35 at the location of the front sensor. The peaks in the bode amplitude correspond to the vibrational frequencies of the shaft. To understand the impact of the damping on the shaft worst-case amplitude gain and natural frequency, we performed a sensitivity analysis where the

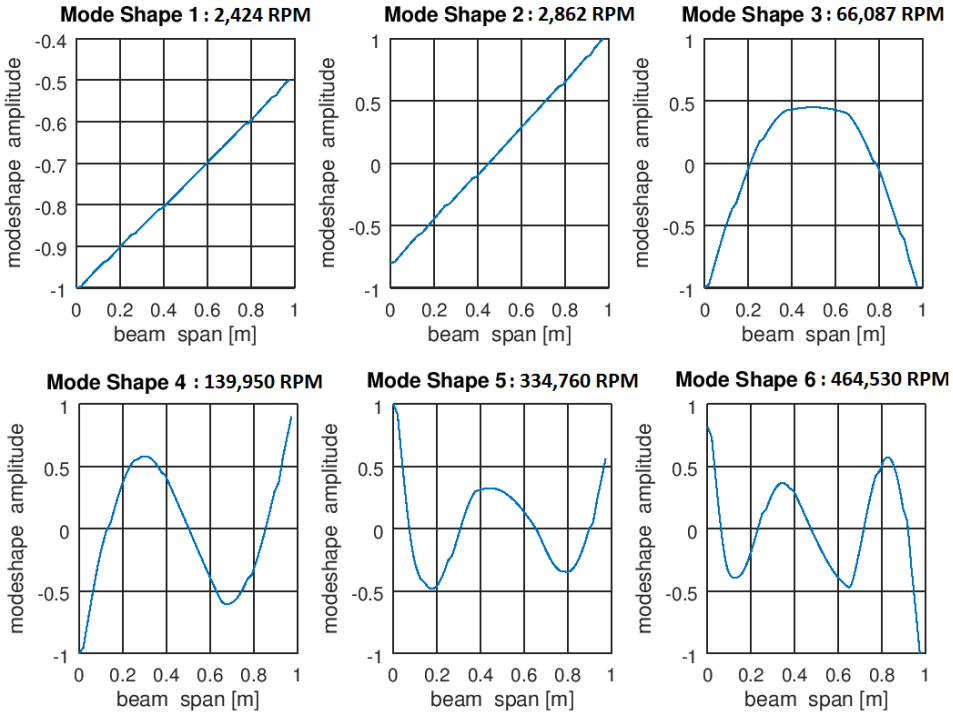

Figure 34. Mode shapes for the loop-scale testbed.

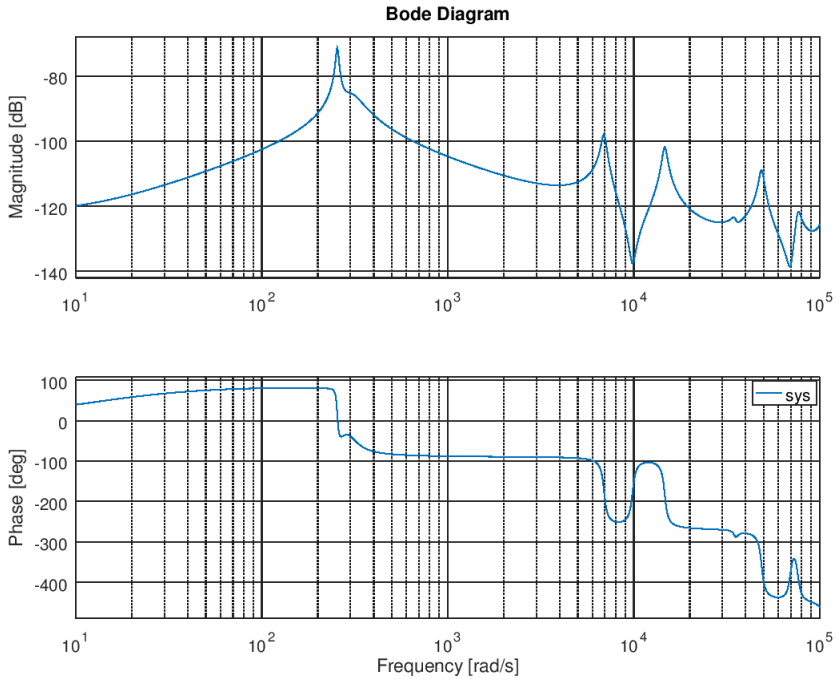

Figure 35. Shaft frequency response for the loop-scale testbed at the front sensor.

damping matrix was assumed to be diagonal and all the damping coefficients were equivalent. Physically this is equivalent to the assumption that the fluid gap thickness and the outer diameter of the shaft are constant along its length, which only approximates the actual system. This is shown in Figure 36. As expected, as the fluid damping increases, the peak amplitude of the resonant frequencies decreases.

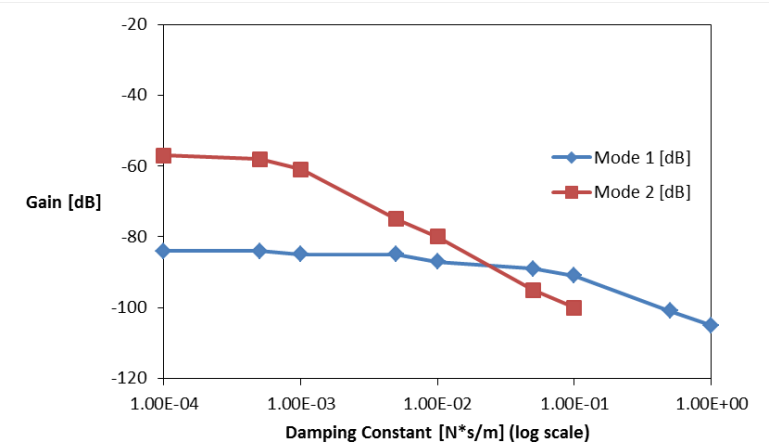

Figure 36. Sensitivity of the worst-case gain of the loop-scale shaft as a function of the damping coefficient.

5 SYSTEM IDENTIFICATION AND MODEL VALIDATION

The accuracy of the theoretical models used for understanding the behavior of the magnetic bearings depends on the uncertainty of this measurements of the system parameters and the simplifying assumptions used in developing the model. It is important that the model is refined to reflect the behavior of the real system. This refinement is accomplished by experimentally determining the parameters using system identification. This process allows the true values of the system parameters to be estimated and any unmodeled higher order system dynamics to be included in the model. Because the model is used to design the stabilizing feedback controller, a better model of the system will allow a better controller design and increase the confidence that the controller will remain stable.

5.1 Bench-Scale Testbed

5.1.1 Magnetic Coil Identification

The first system identification experiments on the bench-scale testbed are designed to identify each coil's inductance and resistance. While resistance is relatively simple to measure, the coil inductance is more complex to measure. Depending on where the measurements are take, they can leave out components that contribute to the overall behavior of the system. For example, as seen in Table 10, measuring the coil resistances at the coil connector will yield a coil resistance smaller than the overall resistance of the power electronics and coil together. By using system identification, the actual dynamic behavior of the physical system is captured and the physical parameters that predict that behavior are found.

Table 10. Bench-scale testbed coil resistances and inductances

	Resistance [Ω]		**Inductance [mH]**	
Coil Name	Measured[a]	Identified	Calculated[b]	Identified
AX+	0.25	0.2744	0.796	2.0779
AX-	0.25	0.2822	0.796	1.4763
AY+	0.24	0.3082	0.796	1.9547
AY-	0.25	0.2769	0.796	1.5440
BX+	0.25	0.2732	0.796	1.9902
BX-	0.25	0.2794	0.796	1.6574
BY+	0.24	0.3052	0.796	1.9401
BY-	0.23	0.2829	0.796	1.6451
Z+	0.46	0.4981	4.2055	26.7444
Z-	0.50	0.5561	4.2055	14.0537

[a]These resistances are measured at the coil connector and do not include the resistances of the cables or the internal resistance of the h-bridge power modules.
[b]These values are calculated using Equation 43.

To estimate the resistance and inductance for each coil, the coils were excited by a step change in their input voltage, as shown in Figure 37.

The coil currents were measured at 10 kHz using a real-time computer. We will denote a measured current by $y_i(t)$. The parameterized model used to describe the coil dynamics is

$$\frac{di(t)}{dt} = -\frac{R}{L}i(t) + \frac{1}{L}v(t). \tag{159}$$

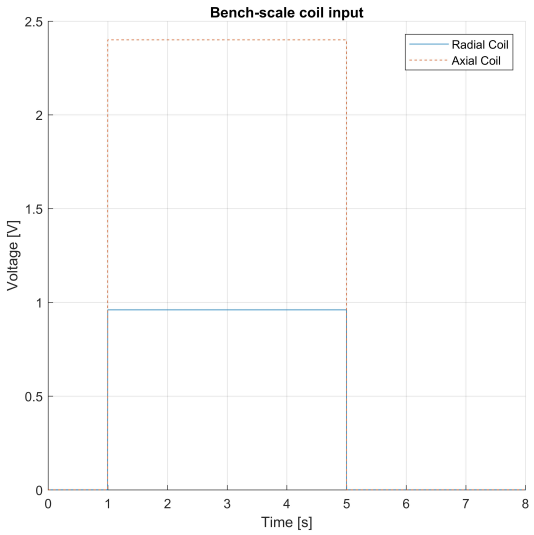

Figure 37. Voltage inputs for system identification of the axial and radial coil parameters.

Given values of L and R and the input $v(t)$ we can calculate the response of the model to the input, which we will denote as $\bar{y}_i(t)$. Then, using the parameterized first-order model of the coil dynamics, the resistance and inductance parameters R and L were identified by solving

$$\{L^*, R^*\} = \min_{\{L,R\}} \sum_t ||y_i(t) - \bar{y}_i(t)||_2, \tag{160}$$

and the results are given in Table 10.

5.1.2 Radial Bearing System Identification

System identification for the shaft motion is more challenging that magnetic coil parameter identification because the magnetic bearings are inherently unstable. This means that any experiment to gather data for system identification must already utilize a stabilizing controller for the magnetic bearings. This then leads to the problem of identifying a system model while operating in closed-loop control or aptly named as closed-loop system identification. There are three main techniques for closed-loop system identification: direct, indirect, and joint-input joint-output. Figure 38 shows a block diagram of the feedback control used to stabilize the magnetic bearings. The reference input r_i is a position signal, the error signal $e = r_i - y$ is the error between the reference position and the measured position y, r_d is a coil voltage reference input, u is the the coil control voltage given by the controller C, G is the physical system, and i is the measured coil currents.

The stabilizing controller C used in the system identification experiments is a Proportional Integral Derivative (PID) controller with gains $K_p = 1.21e3$, $K_i = 4.11e3$, and $K_d = 22.3$, and the derivative filter coefficient is $N = 6000$ or $T_f = 1/6000$. More information on the design of controllers for magnetic bearings is given in Section 6.

Direct closed-loop system identification sets the position reference input $r_i = 0$ and varies the voltage reference input r_d. This directly actuates the physical system inputs and measures the response on the

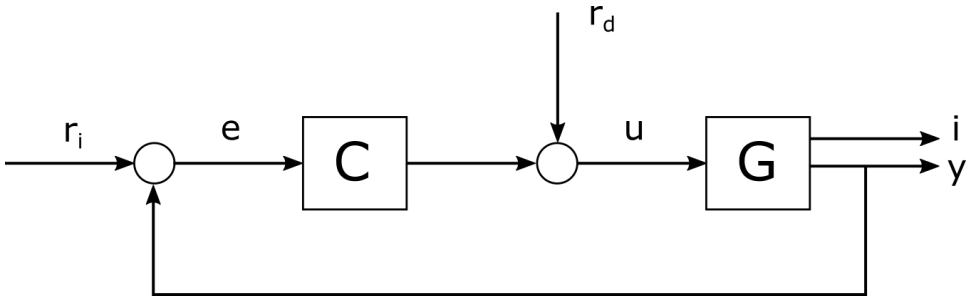

Figure 38. Closed-loop block diagram of the system used to gather the system identification data.

physical system's measured outputs. This approach ignores the feedback and uses the standard open-loop algorithms for determining the model G [6]. Given a model $\hat{G}$ of the real system G and the predicted outputs of $\hat{G}$ given by $\hat{y}$ and $\hat{i}$, the optimal model G^* is given by

$$G^* = \min_{\hat{G}} \sum_t \|\hat{y} - y\|_2 + \|\hat{i} - i\|_2. \tag{161}$$

Indirect closed-loop system identification varies the reference signal r_i and sets $r_d = 0$. Then using the closed-loop model of the system,

$$\hat{G}_c = \frac{CG}{1 + CG}. \tag{162}$$

The optimum closed loop model G_c^* is given by

$$G_c^* = \min_{\hat{G}_c} \sum_t \|\hat{y} - y\|_2 + \|\hat{i} - i\|_2, \tag{163}$$

and using knowledge of the controller dynamics C, the open-loop system G^* can be found by inverting the closed loop system using

$$G^* = \frac{G_c^*}{C - G^* C}. \tag{164}$$

Numerically, this inversion will cause the identified system G^* to be non-minimum phase (extra poles and zeros of the transfer function that nearly cancel). This issue can be resolved using coprime factorization.

The final closed-loop system identification method commonly used is the joint-input joint-output approach where both r_i and r_d are varied. This can resolve some issues with high- and low-frequency errors in the identified model.

Because the model and model structure are well known for magnetic bearings, a greybox parameters estimation approach was chosen for identifying the model of the shaft motion. The data taken in the system identification experiment were collected using the indirect configuration. The excitation signal is injected in r_i and consists of a chirp signal that starts at 0.000001 Hz and stops at 150 Hz. A chirp signal was chosen to excite a rich range of frequencies of shaft motion. The chirp signal starts at 6 sec and ends at 66 sec. The amplitude of the chirp signal is 0.0001 m. By starting the chirp signal at 6 sec, the shaft has already stabilized and the coil currents have stabilized at their bias currents. Data collection starts at 5 sec, and the experimental time vector will likewise start at 5 sec. Since the data collected is for indirect

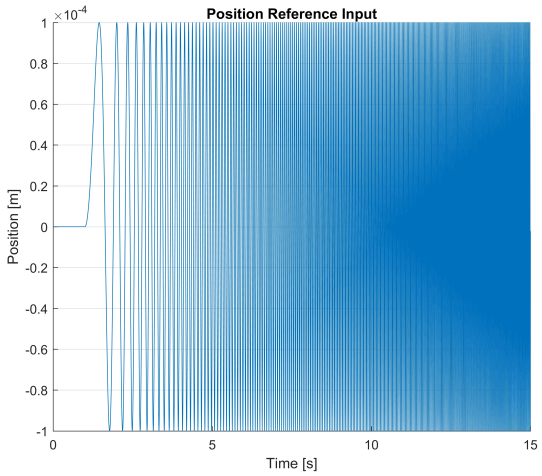

Figure 39. Reference input $r_i(t)$ used for identifying the bench-scale shaft dynamics.

closed-loop identification, the control input injected reference signal $r_d = 0$. Figure 39 shows the chirp signal injected into the system for closed-loop system identification with the time shifted to start at zero for numerical reasons.

The data collection rate of the experiment is 10 kHz, so $dt = 0.0001$ sec.

The data collected and the data names are listed in Table 11.

Table 11. Data collected in the bench-scale shaft motion system identification experiments

Signal	Variable Name	Description	Units
r_i	`reference`	Input signal for system identification	[m]
u	`input`	Output of the PID controller	[V]
y	`position`	Measured shaft position	[m]
i	`current`	Measured coil currents	[A]

The experiment was run five times, and the signals for each run were averaged to reduce Gaussian noise in the data. The control current was measured but does not reflect the actual current injected into the coils. Instead the independent coil currents measured at the output of the H-bridge drivers are used to calculate the effective control current i_c and bias current i_0. These quantities need to be calculated because they are not directly controlled. Since the coil commands are a voltage command v_c and bias v_0, the accuracy of i_c and i_0 are heavily dependent on the accuracy of the coil resistance measurements, so the actual measured currents are used instead of the assumed currents.

Recall that the individual coil currents for a bipolar magnetic bearing with dependent coil voltages are given by

$$i_1 = i_0 + i_c, \tag{165}$$

$$i_2 = i_0 - i_c. \tag{166}$$

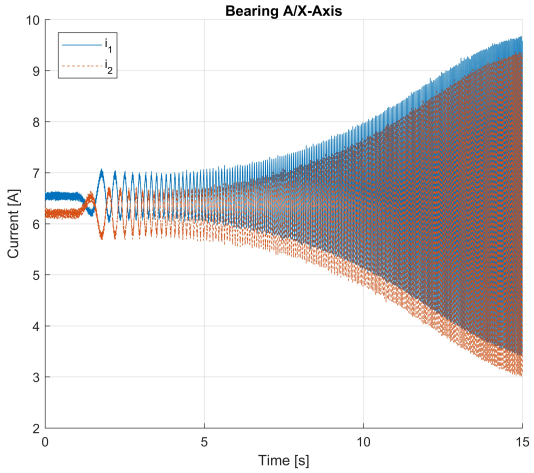

Figure 40. Measured coil currents for the horizontal axis of the bench-scale testbed.

The individual coil currents measured are shown in Figure 40. Using the measured individual coil currents, the actual control current and bias can be calculated using

$$i_c = \frac{1}{2}(i_1 - i_2), \tag{167}$$

$$i_0 = \frac{1}{2}(i_1 + i_2). \tag{168}$$

Figure 41 shows the calculated control current that the horizontal axis coils see. Figure 42 shows the calculated bias current based on the measured coil currents. The desired bias was 6.4 A. Note that the bias decreases slightly as the frequency increases, which implies that the output of the H-bridge drivers is nonlinear and frequency dependent. These dynamics are unmodeled in the theoretical systems models but will be present in the model identified by the system identification experiments.

The measured position for the shaft horizontal motion of the A bearing is shown in Figure 43. To utilize the grey-box system identification method, a state-space model of the closed-loop system is needed. Recall that linearized shaft model is given by

$$\ddot{x}(t) = \frac{k_x}{m}x(t) + \frac{k_i}{m}i(t), \tag{169}$$

$$\frac{di_c(t)}{dt} = -\frac{k_i}{L} - \frac{R}{L}i_c(t) + \frac{1}{L}v_c(t). \tag{170}$$

Then using the states $z_1 = x$, $z_2 = \dot{x}$, and $z_3 = i$ we have the parameterized state-space equation for the shaft and coil dynamics denoted by G and given by

$$\begin{bmatrix} \dot{z}_1 \\ \dot{z}_2 \\ \dot{z}_3 \end{bmatrix} = \begin{bmatrix} 0 & 1 & 0 \\ \frac{k_x}{m} & 0 & \frac{k_i}{m} \\ 0 & -\frac{k_i}{L} & -\frac{R}{L} \end{bmatrix} \begin{bmatrix} x_1 \\ x_2 \\ x_3 \end{bmatrix} + \begin{bmatrix} 0 \\ 0 \\ \frac{1}{L} \end{bmatrix} u, \tag{171}$$

$$y = \begin{bmatrix} 1 & 0 & 0 \\ 0 & 0 & 1 \end{bmatrix} \begin{bmatrix} x_1 \\ x_2 \\ x_3 \end{bmatrix}. \tag{172}$$

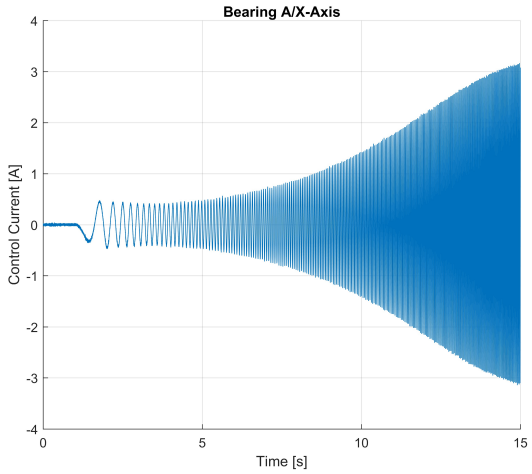

Figure 41. Calculated effective coil control current for the bench-scale testbed system identification experiment.

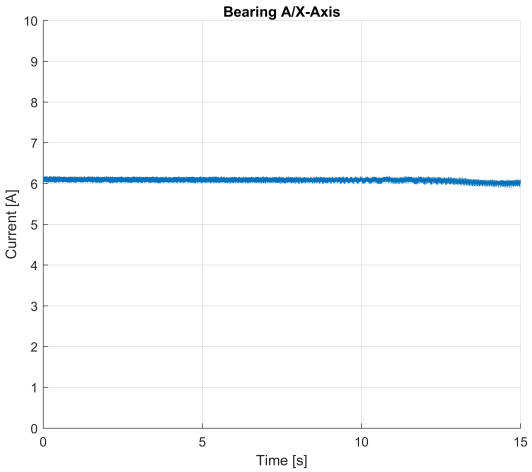

Figure 42. Calculated effective coil bias current for the bench-scale testbed system identification experiment.

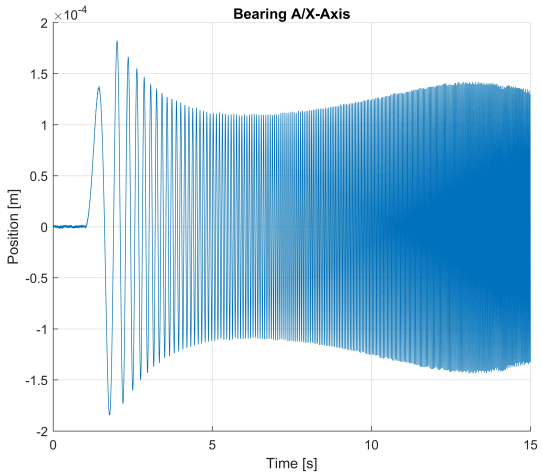

Figure 43. Measured position of the bench-scale testbed horizontal axis during the system identification experiment.

A PID controller with a derivative filter can be expressed as the transfer function

$$C(s) = K_p + \frac{K_i}{s} + \frac{K_d s}{T_f s + 1}, \tag{173}$$

where K_p is the proportional gain, K_i is the integral gain, K_d is the derivative gain, and T_f is the filter frequency. This controller, denoted by C, can also be expressed as the parameterized state-space model

$$\begin{bmatrix} \dot{u} \\ \ddot{u} \end{bmatrix} = \begin{bmatrix} 0 & 0 \\ 0 & -\frac{1}{T_f} \end{bmatrix} \begin{bmatrix} u \\ \dot{u} \end{bmatrix} + \begin{bmatrix} 1 \\ \frac{1}{T_f} \end{bmatrix} e, \tag{174}$$

$$y = \begin{bmatrix} K_i & \frac{K_d}{T_f} \end{bmatrix} \begin{bmatrix} u \\ \dot{u} \end{bmatrix} + \left[K_p + \frac{K_p}{T_f} \right] e. \tag{175}$$

Now, the closed-loop states space equation for the system, denoted by G_c, can be created using the `feedback` command in Matlab©. We chose k_i, k_x, m, L, and R as the parameters to be identified. The parameters k_i and k_x could be further split into their component parameters, but for the lumped model, this was not deemed necessary. The shaft mass m is well known, but the axial placement of the radial bearings is not. This leads to some uncertainty in the shaft mass seen by each bearing, so it was included as a parameter to identify. Including the shaft mass also provides some flexibility to adjust the identified model to compensate for any unmodeled dynamics. This also prevents the optimization from being under constrained. Table 12 shows the identified parameters for the A and B radial bearings.

Table 12. Bench-scale radial bearing magnetic parameters identified using grey box system identification

Parameter	Identified Value	Theoretical Value	Units
Bearing A			
k_i	8.8844	4.6815	[N/A]
k_x	2.1186×10^4	1.4901×10^4	[N/m]
L	1.2075	0.7960	[mH]
R	0.2168	0.24	[Ω]
m	3.9524	2.5225	[kg]
Bearing B			
k_i	9.3739	4.4751	[N/A]
k_x	2.6134×10^4	1.3616×10^4	[N/m]
L	1.2883	0.7960	[mH]
R	0.1909	0.24	[Ω]
m	4.5809	2.5225	[kg]

6 CONTROL SYSTEM DESIGN

Magnetic bearings are inherently unstable systems, so feedback control is needed to stabilize and levitate the shaft. Feedback control has been utilized since the 1920s in practically every industrial setting to automate a wide variety of physical systems. Before going into detail on the control design for the bench-scale and loop-scale magnetic bearings, we will very briefly describe some of the general aspects of modern control for the readers who are unfamiliar with control theory or modern control design techniques.

In general, a feedback controller takes measurements of a physical system and uses them to create a control input to actuators in the system that modify the unforced behavior of the physical system to minimize the effect of unknown external disturbances, stabilize the system states, and improve the overall performance. Figure 44 shows the standard block-diagram of a closed-loop feedback control system. In Figure 44, C is a

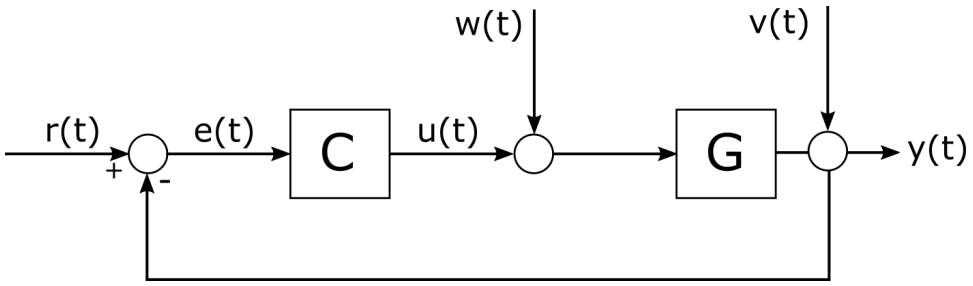

Figure 44. Closed-loop block diagram of a typical feedback control system.

controller, G is the physical system, $u(t)$ are the control signals, $w(t)$ are unknown control disturbances, $y(t)$ are the measurements, $v(t)$ are unknown measurement disturbances, $r(t)$ is a reference input which defines the desired values of the system states, and $e(t)$ is the error between the desired value of the system states and the measured system states.

System states are defined as the minimal number of physical quantities required to mathematically describe the time evolution of the physical system. For example, as seen in Section 4, the shaft position, shaft velocity, and magnetic coil currents are the states of the system required to fully describe the dynamics of a

magnetic bearing. Note that for linear systems, the existence of similarity transforms means that the system states do not necessarily correspond to a familiar physical quantity. Performance criteria for controllers mathematically describe desired conditions on the systems states, some of which are general and some that are related to the specific application.

Performance criteria for controllers target many different quantitative metrics. Arguably the most critical performance criteria for a controller is stability. There are multiple mathematical definitions describing stability such as exponential stability, uniform stability, or bounded-input bounded-output stability, to name a few. For example, a system state $x(t)$ is *Lyapunov stable* about the equilibrium point x_e if for every $\epsilon > 0$ there exists $\delta(\epsilon) > 0$ such that if $\|x(0) - x_e)\| < \delta$, then for every $t > 0$ we have $\|x(t) - x_e\| < \epsilon$. Colloquially, this means that a system state will remain bounded by ϵ for all time if it starts close enough to the equilibrium point and that that point always exists. While in general, stability means that the error between the desired system states and the actual (measured) system states does not get infinitely large, stability performance metrics such as exponential stability mean that the error converges asymptotically to zero. Another important control performance metric is the speed at which the system error converges to zero, known as the *settling time*. The system settling time is the time after which the system state remains within a specified error band around the reference value. Typically, this is calculated in response to a unit step change in the reference input. Another important performance metric used is the amplitude of the system states in response to disturbances. Using frequency domain analysis, we can take the Laplace transform of the general closed-loop system shown in Figure 44 to find the transfer functions from the reference input $r(t)$ and disturbance $w(t)$ to the measurements $y(t)$ and the error $e(t)$, respectively, given by

$$Y(s) = \frac{C(s)G(s)}{1 + C(s)G(s)}R(s) - \frac{G(s)}{1 + C(s)G(s)}W(s), \tag{176}$$

$$E(s) = \frac{1}{1 + C(s)G(s)}R(s) + \frac{G(s)}{1 + C(s)G(s)}W(s). \tag{177}$$

Minimizing the impact of the disturbances on the system is equivalent to finding a controller C that minimizes the amplitude over all frequencies ω:

$$\min_{0 \leq \omega \leq \infty} \left\| \frac{G(\omega)}{1 + C(\omega)G(\omega)} \right\|. \tag{178}$$

Finally, performance can be defined in terms of the uncertainties in the system caused by modeling uncertainties or external disturbances. This leads to defining robust systems that are stable and meet their convergence and performance requirements in the worst-case upper bounds on their uncertainties.

The control design process starts with developing a model of the system that describes the behavior of the physical system. This model is then used to design the feedback controller. The complexity of this model is driven by the performance requirements on the controller; as the desired performance increases, the accuracy of the model must correspondingly increase. This model is used to validate the controller performance; then the controller is deployed on the physical system to verify its performance. There are many techniques available for designing feedback controllers, and we will present a brief overview here.

By far, the most commonly used feedback control is a Proportional Integral Derivative (PID) controller. This is because it is simple to apply and is analogous to physical systems, which makes understanding the controller more intuitive than other types of controller that do not have easily accessible physical analogies. The differential equation of a PID controller is given by

$$u(t) = K_p e(t) + K_i \int_0^t e(t) + K_d \dot{e}(t), \tag{179}$$

where $e(t)$ is the error between the reference input $r(t)$ and the measured output $y(t)$, and the proportional K_p, integral gain K_i, and derivative K_d gains are chosen by the designer. Physically, this system is equivalent to a mass-spring-damper system or a resistor, capacitor, inductor circuit. PID controllers are single-input single-output (SISO) controllers, which means that for complex or highly coupled systems, the system needs to be decoupled into separate simplified models. When designing PID controllers, linear or linearized models, which encompass many physical systems, are used. For loosely coupled systems or systems with small nonlinearities, PID controllers are simple and easy to apply and have excellent performance because the feedback configuration makes them extremely robust to uncertainties and nonlinearities. However, for strongly coupled systems multi-input multi-output (MIMO) dynamics and systems with high-performance requirements or large nonlinearities, PID controllers that are stable and have sufficient performance may not exist.

Another class of feedback controllers known as optimal controllers are based on time-domain analysis and apply to complex coupled MIMO systems. Optimal control design starts with the general state-space model of a system given by

$$\dot{x}(t) = Ax(t) + Bu(t), \tag{180}$$

$$y(t) = Cx(t) + Bu(t), \tag{181}$$

and then the objective is to find a feedback controller

$$u(t) = -Kx(t) \tag{182}$$

that minimizes the cost function

$$J = \int_0^\infty x(t)^T Qx(t) + u(t)^T Ru(t) + 2x(t)^T Nu(t)dt, \tag{183}$$

subject to the system dynamics $\dot{x} = Ax + Bu$. The matrices Q, R, and N are chosen to balance the need to reduce error and prevent control inputs from becoming too large. Note that the feedback controller uses the full state $x(t)$ and not the measurements $y(t)$. This means that all system states need to be measured, which is often expensive and impractical, or that the states need to be estimated. State estimation for the magnetic bearings will be discussed further in Section 6.2. Given some technical conditions on the A and C matrix, techniques to estimate all the system states have been developed that can be applied in a recursive online algorithm. The most celebrated online state estimation technique is the Kalman filter. The optimal control problem can be generalized to nonlinear systems. The combination of a linear optimal controller and Kalman filter is known as a Linear Quadratic Gaussian (LQG) controller.

Another major control design technique is known as Robust Control. This control design technique was developed in response to the lack of theoretical robustness for LQG controllers, although in practice LQG controller perform well. Robust controllers use mathematical upper bounds on model uncertainties and system disturbances to design a controller that guarantees stability and performance under these worst-case uncertainty bounds.

Model Predictive Control (MPC) is a control synthesis technique that recursively optimizes the system response. Using a predictive model of the system, the system response over a defined time window from current time step to a future time is optimized to find an optimal control input u^*. This optimal control input is then applied at the next time step, and the optimization process is repeated based on the new measurements at that time step. This optimization over this sliding window of time is highly robust to

nonlinearities in the system dynamics. However, the optimization process requires significant computational overhead, which means that it cannot currently be applied to systems with high-frequency dynamics. MPC controllers are typically used in the control of chemical or other processes that are nonlinear and have low-frequency dynamics, although there is significant active research into the application of MPC to systems with high-frequency dynamics.

Finally, an incomplete list of other control design techniques that are not as common is as follows: adaptive control, sliding mode control, variable structure control, and model-free control.

6.1 Decoupled PID Controller Design for Magnetic Bearings

The most common controllers used to stabilize magnetic bearings are decoupled PID controllers. For many magnetic bearing applications, PID controllers provide excellent performance. The decoupled axes are usually vertical and horizontal axes controlled by the radial bearings and an axis along the shaft centerline controlled by the thrust bearings. Some magnetic bearings utilize more than two radial axes. The main physical mechanisms that create coupling forces between axes are shaft imbalances, fluid forces on the shaft, and gyroscopic terms. Magnetic bearings that operate in air or vacuum have low-to-no fluid forces on the shaft, and the shaft is typically well balanced, so the magnitude of the coupling forces is low and a decoupled model is sufficient. The PID control design also uses the linearized model of the shaft and coil dynamics. If the shaft excursion away from the linearized operating point remains small, this assumption is sufficient.

Developing accurate models of the magnetic bearings which are then used for high-performance control design require performing system identification and model validation, as detailed in Section 5. Because the experiments required to gather data for system identification need a stabilizing controller, developing a decoupled PID controller to initially stabilize the testbeds is important for data collection.

6.1.1 Single-Loop PID Control

Using the simplified linearized equations for a bipolar magnetic bearing, the PID controller can be designed with the shaft position as the measurement and the coil voltage as the input.

The AMB model we will use is the linearized bipolar design given by

$$m\ddot{x} = k_x x + k_i i. \tag{184}$$

Using the Laplace transform, we will convert this into a transfer function. The Laplace transform of Equation (184) is

$$ms^2 X(s) - k_x X(s) = k_i I(s). \tag{185}$$

To use the coil dynamics to develop a PID controller, we must assume that $\dot{x} \equiv 0$, so the coil equation is given by

$$L\frac{di}{dt} + Ri = -k_i \dot{x}(t) + v(t). \tag{186}$$

The Laplace transform of the coil dynamics is given by

$$sLI(s) + RI(s) = V(s) - k_i sX(s), \tag{187}$$

$$I(s) = \frac{V(s) - k_i sX(s)}{(Ls + R)}. \tag{188}$$

Combining Equations (185) and (187) we have

$$ms^2X(s) - k_xX(s) = k_i\left(\frac{V(s) - k_i sX(s)}{(Ls + R)}\right), \tag{189}$$

$$\left(mLs^3 + mRs^2 - k_xLs - k_xR\right)X(s) = k_iV(s) - k_i^2 sX(s), \tag{190}$$

$$\left(mLs^3 + mRs^2 + (k_i^2 - k_xL)s - k_xR\right)X(s) = k_iV(s), \tag{191}$$

which gives the combined shaft/coil transfer function in input/output form

$$G(s) = \frac{X(s)}{V(s)} = \frac{k_i}{mLs^3 + mRs^2 + (k_i^2 - k_xL)s - k_xR}. \tag{192}$$

The PID controller in transfer function form is given by

$$G_c(s) = \frac{V(s)}{E(s)} = \frac{K_ds^2 + K_ps + K_i}{s}. \tag{193}$$

Finally, the open-loop equivalent transfer function of the system is given by

$$G_{cl}(s) = \frac{G_c(s)G(s)}{1 + G_c(s)G(s)}, \tag{194}$$

$$= \frac{k_iK_ds^2 + k_iK_ps + k_iK_i}{mLs^4 + mRs^3 + (k_i^2 - k_xL + k_iK_d)s^2 + (k_iK_p - k_xR)s + k_iK_i}. \tag{195}$$

Now, assume there are four poles $\{p_1, p_2, p_3, p_4\} \in \mathbb{C}$ where the real part of the poles is less than zero. Then we can calculate the fourth-order polynomial using the Matlab© command `conv` given by

$$s^4 + f_3s^3 + f_2s^2 + f_1s + f_0. \tag{196}$$

Associating terms, we have

$$K_i = \frac{mLf_0}{k_i}, \tag{197}$$

$$K_p = \frac{mLf_1 + k_xR}{k_i}, \tag{198}$$

$$K_d = \frac{mLf_2 + k_xL - k_i^2}{k_i}. \tag{199}$$

Note that the term mRs^3 has no control, so the poles cannot be placed arbitrarily using a PID controller. The relationship between the poles and the coefficients of the closed-loop denominator can be seen by

$$d = (s + p_1)(s + p_2)(s + p_3)(s + p_4), \tag{200}$$

$$= (s^2 + (p_1 + p_2)s + p_1p_2)(s^2 + (p_3 + p_4)s + p_3p_4), \tag{201}$$

$$= s^4 + (p_1 + p_2 + p_3 + p_4)s^3 + (p_1p_2 + p_3p_4 + (p_1 + p_2)(p_3 + p_4))s^2, \tag{202}$$

$$+ (p_1p_2(p_3 + p_4) + p_3p_4(p_1 + p_2))s + p_1p_2p_3p_4. \tag{203}$$

This shows that the term $f_3 = R/L$, which is related to the transient behavior of the unforced coil dynamics. This limits the total of all the poles by $p_1 + p_2 + p_3 + p_4 = R/L$, or in other words, the convergence time of the PID controller is limited by the coil dynamics.

Traditionally, for voltage control of magnetic bearings using PID control, it is assumed that the term $\frac{k_i}{L}\dot{x}(t) \approx 0$ in the coil dynamics, which makes the denominator of the closed-loop transfer function third order, and the PID controller can arbitrarily place the poles. This is valid for stable operation but can present problems during transient behavior.

6.1.2 Explicit Current Control

For the bench-scale testbed, instead of ignoring the shaft velocity effects on the coil dynamics to avoid this performance issue, a different control architecture is used. Instead of voltage control, the coil dynamics and shaft dynamics are separated, and the coil current is controlled using an inner control loop, and the shaft position is controlled using current control, as shown in Figure 45. In this architecture, C_s is the controller

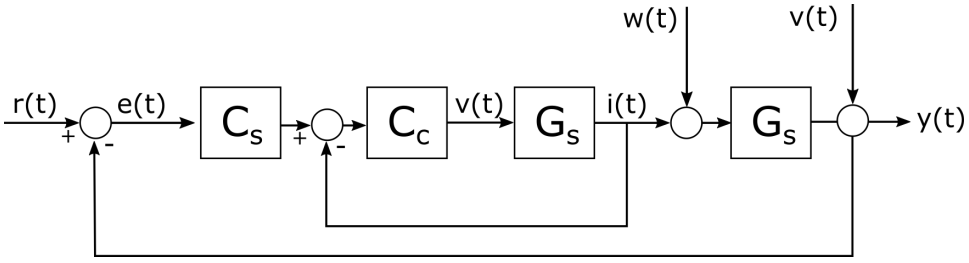

Figure 45. Closed-loop block diagram of bench-scale feedback control system.

for the shaft position, C_i is the controller for the coil current, G_c is the coil dynamics, and G_s is the shaft dynamics. The coil controller improves the transient response of the coil dynamics and reduces the error in the expected coil current. The shaft PID controller then stabilizes the shaft position.

The coil model is given by

$$LsI(s) + RI(s) = V(s), \tag{204}$$

and the transfer function for the coil is then

$$G_c(s) = \frac{I(s)}{V(s)} = \frac{1}{Ls + R} = \frac{1/L}{s + R/L}. \tag{205}$$

The coil current PID controller is given by

$$C_c(s) = K_p^i + K_d^i s + \frac{1}{s}K_i^i = \frac{K_d^i s^2 + K_p^i s + K_i^i}{s}. \tag{206}$$

The feedforward path is then

$$C_c(s)G_c(s) = \frac{(K_d^i s^2 + K_p^i s + K_i^i)}{s(Ls + R)}. \tag{207}$$

And finally, the open-loop system equation is given by

$$G = \frac{C_c G_c}{1 + C_c G_c} = \frac{\frac{(K_d^i s^2 + K_p^i s + K_i^i)}{s(Ls+R)}}{1 + \frac{(K_d^i s^2 + K_p^i s + K_i^i)}{s(Ls+R)}}, \tag{208}$$

$$= \frac{(K_d^i s^2 + K_p^i s + K_i^i)}{s(Ls+R) + (K_d^i s^2 + K_p^i s + K_i^i)}, \tag{209}$$

$$= \frac{(K_d^i s^2 + K_p^i s + K_i^i)}{Ls^2 + Rs + (K_d^i s^2 + K_p^i s + K_i^i)}, \tag{210}$$

$$= \frac{(K_d^i s^2 + K_p^i s + K_i^i)}{(L + K_d^i)s^2 + (R + K_p^i)s + K_i^i)}. \tag{211}$$

$$\tag{212}$$

Hence, we have

$$\omega_n^2 = \frac{K_i^i}{(L + K_d^i)}, \tag{213}$$

$$2\zeta\omega_n = \frac{R + K_p^i}{L + K_d^i}. \tag{214}$$

If we set K_d^i, we have

$$K_i^i = L\omega_n^2 + K_d^i\omega_n^2, \tag{215}$$

$$K_p^i = 2\zeta\omega_n(L + K_d^i) - R. \tag{216}$$

Given a rotational frequency of the shaft of $\omega_s = 60$ Hz (377 rad/s) and choosing $\omega_n = 3\omega_s$, $\zeta = 0.9$, and $K_d^i = 0$, we have the PI controller gains $K_p^i = 1.95$ and $K_i^i = 1660$ and the closed-loop transfer function for the coil given by

$$G_{coil} = \frac{K_p^i s + K_i^i}{Ls^2 + (R + K_p^i)s + K_i^i} = \frac{1497s + 1.279e^6}{s^2 + 2036s + 1.279e^6}, \tag{217}$$

with zero $z_1 = -854$ and poles $\lambda_i = -1018 \pm j493$.

Next the linearized shaft model with $k_x > 0$ and $k_i > 0$ is given by the equation

$$ms^2X(s) - k_xX(s) = k_iI(s), \tag{218}$$

which gives the unstable transfer function

$$G_s(s) = \frac{X(s)}{I(s)} = \frac{k_i}{s^2 - k_x}. \tag{219}$$

With a shaft controller given by

$$C_s(s) = \frac{K_d s^2 + K_p s + K_i}{s} \tag{220}$$

and the coil closed loop transfer function given above, we have the feedforward path transfer function given by

$$C_s G_{coil} G_s = \frac{K_d s^2 + K_p s + K_i}{s} \frac{K_p^i s + K_i^i}{L s^2 + (R + K_p^i) s + K_i^i} \frac{k_i}{s^2 - k_x}. \tag{221}$$

6.1.3 Numerical Derivatives

For most feedback control applications, the derivative of a sensor signal will be used either as an explicit input to the controller in the case of an optimal controller or the controller will take the numerical derivative of a sensor signal internally as in the case of the PID controller (i.e., $K_d \dot{x}(t)$). However, a PID controller software implementation does not need to use the numerical derivative if it is supplied by a sensor or other means like a Kalman filter. Regardless, taking the numerical derivative of a noisy sensor signal will be overwhelmed by the noise. To reduce the noise in a numerical derivative, the signal can be prefiltered, and often in applied PID control, a first-order low-pass filter is integrated with the derivative term as follows:

$$u_d(t) = \frac{K_d s}{T_f s + 1}. \tag{222}$$

Another technique used to minimize sensor noise is online state estimation, which will be described in the following section.

6.2 State Estimation

State estimation is an optimal sensor fusion technique that uses knowledge about the system dynamics, sensor noise, and state uncertainty to minimize the impact of the sensor noise on the estimated states. While there are many state estimation techniques, the most celebrated is the Kalman filter. This technique was developed by Rudolph Kalman in the 1950's and is the foundation of other online state estimation techniques.

For linear systems, the Kalman filter is the exact optimal solution to the state estimation problem. It is a recursive implementation of a Bayesian filter that minimizes the uncertainty of the estimated states. The Kalman filter starts with a discrete time model of the system dynamics.

6.2.1 Linear State-Space Model Discretization

The properties of a linear state-space model admit a universal transformation that is valid for all linear state-space models. Because of the common use of these models, we will begin by deriving this transformation. First, a continuous time linear state space system is given by

$$\dot{x}(t) = Ax(t) + Bu(t) + w(t), \tag{223}$$

$$y(t) = Cx(t) + Du(t) + v(t), \tag{224}$$

where $x \in \mathbb{R}^n$, $u \in \mathbb{R}^m$, and $y \in \mathbb{R}^p$, meaning that $A \in \mathbb{R}^{n \times n}$, $B \in \mathbb{R}^{n \times m}$, $C \in \mathbb{R}^{p \times m}$, and $D \in \mathbb{R}^{p \times m}$. The vectors $w(t)$ and $v(t)$ are process and sensor noise, respectively, which are typically given by zero mean

Gaussian distributions $w(t) \in \mathcal{N}(0, Q)$ and $v(t) \in \mathcal{N}(0, R)$, where Q and R are covariance matrices. This system can be transformed into a discrete-time state space model given by

$$x[k+1] = A_d x[k] + B_d u[k], \tag{225}$$

$$y[k] = C_d x[k] + D_d u[k], \tag{226}$$

assuming a zero-order hold for the input u and with a constant discrete time step of $t[k+1] - t[k] = T$. To find the transformation, we start with the solution to Equations (223) and (224). The term $Ax(t)$ in Equation (223) is the homogeneous part of the ordinary differential equation, and the last two terms are forcing functions that will contribute to the particular solution. We begin with the solution to the continuous time linear state space equation given by

$$x(t) = e^{At}x(0) + \int_0^t e^{A(t-\tau)}[Bu(\tau)]d\tau. \tag{227}$$

At time $(k+1)T$, the system states $x(\cdot)$ are given by

$$x((k+1)T) = e^{A(k+1)T}x(0) + \int_0^{(k+1)T} e^{A[(k+1)T-\tau]}[Bu(\tau)+]d\tau, \tag{228}$$

$$x((k+1)T) = e^{A(k+1)T}x(0) + \int_0^{(k+1)T} e^{A(k+1)T}e^{-A\tau}[Bu(\tau)]d\tau, \tag{229}$$

$$x((k+1)T) = e^{A(k+1)T}x(0) + e^{A(k+1)T}\int_0^{(k+1)T} e^{-A\tau}[Bu(\tau)]d\tau. \tag{230}$$

The unknown term $e^{A(k+1)T}x(0)$ can found by evaluating the system states at time kT, post-multiplying by the constant matrix e^{AT} given by

$$x(kT) = e^{AkT}x(0) + e^{AkT}\int_0^{kT} e^{-A\tau}[Bu(\tau)]d\tau, \tag{231}$$

$$e^{AT}\left[x(kT) = e^{AkT}x(0) + e^{AkT}\int_0^{kT} e^{-A\tau}[Bu(\tau)]d\tau\right], \tag{232}$$

$$e^{AT}x(kT) = e^{AT}e^{AkT}x(0) + e^{AT}e^{AkT}\int_0^{kT} e^{-A\tau}[Bu(\tau)]d\tau, \tag{233}$$

$$e^{AT}x(kT) = e^{AT+AkT}x(0) + e^{AT+AkT}\int_0^{kT} e^{-A\tau}[Bu(\tau)+w(\tau)]d\tau, \tag{234}$$

$$e^{AT}x(kT) = e^{A(k+1)T}x(0) + e^{A(k+1)T}\int_0^{kT} e^{-A\tau}[Bu(\tau)]d\tau, \tag{235}$$

$$\implies e^{A(k+1)T}x(0) = e^{AT}x(kT) - e^{A(k+1)T}\int_0^{kT} e^{-A\tau}[Bu(\tau)]d\tau. \tag{236}$$

Substituting this expression for the initial condition at time $(k+1)T$ into Equation (230) gives the finite difference equation for the state evolution

$$x((k+1)T) = e^{AT}x(kT) + \int_{kT}^{(k+1)T} e^{A[(k+1)T-\tau]}d\tau[Bu(kT)], \tag{237}$$

since $u(kT)$ is constant on the interval $t \in [kT, (k+1)T]$. With a change of variable $\lambda = (k+1)T - \tau$, which implied that $d\lambda = -d\tau$, we can rewrite this equation as

$$x((k+1)T) = e^{AT}x(kT) - \int_T^0 e^{A\lambda}d\lambda[Bu(kT)], \tag{238}$$

$$x((k+1)T) = e^{AT}x(kT) + \int_0^T e^{A\lambda}d\lambda[Bu(kT)], \tag{239}$$

where from inspection we can see that the discrete time matrices are given by

$$A_d = e^{AT}, \tag{240}$$

$$B_d = \left(\int_0^T e^{A\lambda}d\lambda\right)B = A^{-1}(A_d - I)B, \tag{241}$$

$$C_d = C, \tag{242}$$

$$D_d = D. \tag{243}$$

The discrete time state-transition matrix A_d is calculated using a matrix exponential which is defined as

$$e^A = \sum_{k=0}^{\infty} \frac{1}{k!}A^k. \tag{244}$$

This can be calculated in Matlab© using the *expm()* command.

6.2.2 Model Transformation

The discrete time or difference model of a nonlinear ordinary differential equation can be calculated using three different definitions of a derivative. The forward difference equation is given by

$$\frac{dx(t)}{dt} = \frac{x(t+\Delta t) - x(t)}{\Delta t}. \tag{245}$$

The backwards difference equation is given by

$$\frac{dx(t)}{dt} = \frac{x(t) - x(t-\Delta t)}{\Delta t}. \tag{246}$$

The trapezoidal or central difference equation is given by

$$\frac{dx(t)}{dt} = \frac{(x(t+\Delta t) - x(t-\Delta t)}{2\Delta t}. \tag{247}$$

These derivative functions can be expressed as a function of an index variable $k \in \mathbb{Z}$, removing the explicit time dependence. The forward difference equation becomes

$$\frac{dx(t)}{dt} = \frac{x((k+1)\Delta t) - x(k\Delta t)}{\Delta t}. \tag{248}$$

The backwards difference equation becomes

$$\frac{dx(t)}{dt} = \frac{x(k\Delta t) - x((k-1)\Delta t)}{\Delta t}. \tag{249}$$

The trapezoidal or central difference equation is given by

$$\frac{dx(t)}{dt} = \frac{(x((k+1)\Delta t) - x((k-1)\Delta t)}{2\Delta t}. \tag{250}$$

To simplify the notation, we will use the substitution $x[k] = x(k\Delta t)$ to denote a discrete time function with an implicit Δt.

As an example, we will analyze the differential equation describing a second-order mass spring damper system

$$\dot{x_1} = x_2, \tag{251}$$
$$\dot{x_2} = -200x_1 - 17x_2 + u. \tag{252}$$

The first equation can be discretized using the forward difference equation as follows:

$$\frac{dx_1(t)}{dt} = \frac{x_1[k+1] - x_1[k]}{\Delta t} = x_2[k], \tag{253}$$
$$x_1[k+1] - x_1[k] = \Delta t x_2[k], \tag{254}$$
$$x_1[k+1] = x_1[k] + \Delta t x_2[k]. \tag{255}$$

The second equation can be discretized also using the forward difference equation as follows:

$$\frac{dx_2(t)}{dt} = \frac{x_2[k+1] - x_2[k]}{\Delta t} = -5800x_1[k] - 17x_2[k] + u[k], \tag{256}$$
$$x_2[k+1] - x_2[k] = -200\Delta t x_1[k] - 17\Delta t x_2[k] + \Delta t u[k], \tag{257}$$
$$x_2[k+1] = -200\Delta t x_1[k] + (1 - 17\Delta t)x_2[k] + \Delta t u[k]. \tag{258}$$

With a time interval of $\Delta t = 0.001$ seconds, this yields the discrete time state-space equation

$$z[k+1] = \begin{bmatrix} 1 & 0.001 \\ -5.8 & 0.99 \end{bmatrix} z[k] + \begin{bmatrix} 0 \\ 0.001 \end{bmatrix} u[k], \tag{259}$$
$$y[k] = \begin{bmatrix} 1 & 0 \end{bmatrix} z[k] + \begin{bmatrix} 0 \end{bmatrix} u[k]. \tag{260}$$

Comparing this to the linear state-space model transformation that yields the discrete time system,

$$z[k+1] = \begin{bmatrix} 0.9971 & 0.0009941 \\ -5.766 & 0.9872 \end{bmatrix} z[k] + \begin{bmatrix} 5e^{-7} \\ 0.0009941 \end{bmatrix} u[k], \tag{261}$$
$$y[k] = \begin{bmatrix} 1 & 0 \end{bmatrix} z[k] + \begin{bmatrix} 0 \end{bmatrix} u[k], \tag{262}$$

shows that the forward difference method for discretizing the system closely matches the more accurate model given by the linear state-space model transformation. Note that as $\Delta t \to \infty$, the two models converge at the expense of higher computation.

6.3 Linear Kalman Filter

While the linear Kalman filter was originally developed for control systems and is used extensively in those applications, it is also applied to a wide array of data analysis applications because of its general formulation. In general terms, the major steps in the Kalman Filter process are

i) Prediction Step

(a) Estimate the next state of the system based on the model.

(b) Predict the estimated covariance of the next state.

ii) Update Step

(a) Calculate the difference between the estimated next state and the measurement.

(b) Calculate the optimal Kalman gain.

(c) Update the estimated state.

(d) Update the estimated state covariance.

Recursive Bayesian filters are all founded on this basic algorithm. We will present the Kalman filter algorithm without deriving it, but readers who are interested can go to references [[13],[1], and [12]] for more information.

Assuming that the system dynamics are time invariant, we have the discrete-time model

$$x_{k+1} = A_d x_k + B_d u_k + w_k, \tag{263}$$

$$y_k = C_d x_k + D_d u_k + v_k. \tag{264}$$

The goal of the Kalman filter is to minimize the difference between the estimated state $\hat{x}_k$ and the actual state x_k, where t_k is the current time step. The Kalman Filter Prediction step takes the previous estimation of the state and the current control input and estimates the state measurement and uncertainty based on the system dynamics, which are calculated by

$$\hat{x}_k^- = A_d \hat{x}_{k-1}^+ + B_d u_{k-1}, \tag{265}$$

$$P_k^- = A_d P_{k-1}^+ A_d^T + Q, \tag{266}$$

where $\hat{x}_k^-$ is the predicted state at time step k, $\hat{x}_{k-1}^+$ is the updated prediction from the prior time step, P_{k-1}^+ is the state updated state uncertainty from the prior time step, and Q is the covariance matrix of the process noise w. The process noise is assumed to be Gaussian with zero mean, so $w_k \in \mathcal{N}(0, Q)$.

After the prediction step, which uses only knowledge of the system dynamics, the sensor measurements y_k are used to correct the predicted measurement. The measurement innovation is calculated by the error term

$$z_k = y_k - C_d \hat{x}_k^-. \tag{267}$$

Then the optimal Kalman gain is calculated based on the measurement and state uncertainties by

$$K_k = P_k^- C_c^T (C_d P_k^- C_d^T + R)^- 1, \tag{268}$$

where R is the sensor noise covariance matrix, and the sensor noise is also assumed to be Gaussian with zero mean, so $v_k \sim \mathcal{N}(0, R)$. The Kalman gain balances between the model uncertainty and the sensor uncertainty by updating the state estimate and state uncertainty using

$$x_k^+ = K_k z_k, \tag{269}$$

$$P_k^+ = (I - K_k C_d) P_k^- (I - K_k C_d)^T + K_k R K_k^T. \tag{270}$$

Assuming that there is no correlation between the current sensors and the position sensors, calculate the variance of the Baumer inductive sensor as $\sigma_x^2 = 2.8271 \times 10^{-13}$ m^2 and the on-board H-bridge driver current sensor as $\sigma_i^2 = 1.2311 \times 10^{-4}$ A^2 to arrive at the diagonal sensor covariance matrix

$$R = \begin{bmatrix} 2.8271 \times 10^{-13} & 0 \\ 0 & 1.2311 \times 10^{-4} \end{bmatrix}. \tag{271}$$

Similarly, the variance of the static control voltage signal can be calculated from data to be $\sigma_V^2 = 0.0023$ V^2, so the process noise covariance matrix is given by

$$Q = \begin{bmatrix} 0 & 0 & 0 \\ 0 & 0 & 0 \\ 0 & 0 & 0.0023 \end{bmatrix}. \tag{272}$$

Because the position and velocity are not directly controlled, their variance is equal to zero. Then by applying the Kalman filter to the bench-scale model identified experimentally, the position, velocity, and coil currents can be estimated. Figures 46, 47, and 48 show the Kalman filter estimates of the shaft position, velocity, and coil current, respectively. Figures 49, 50, and 51 show the Kalman Filter estimates

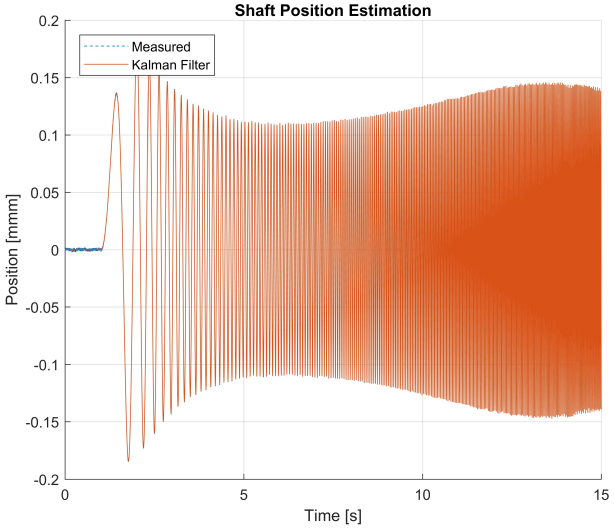

Figure 46. The shaft position estimate using a linear Kalman filter.

of the shaft position, velocity, and coil current, respectively, in a smaller time window. Note that the state estimates for the position and coil current are compared to the measured shaft position and coil current while the velocity is not directly measured, so it is compared to the numerical derivative of the position

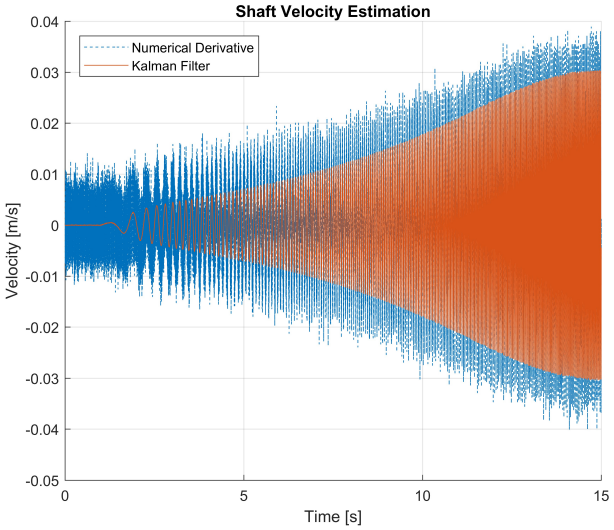

Figure 47. The shaft velocity estimate using a linear Kalman Filter.

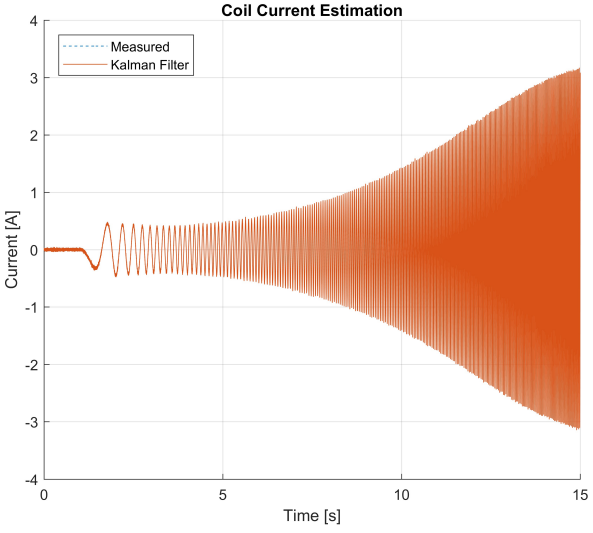

Figure 48. The bipolar magnetic coil current estimate using a linear Kalman Filter.

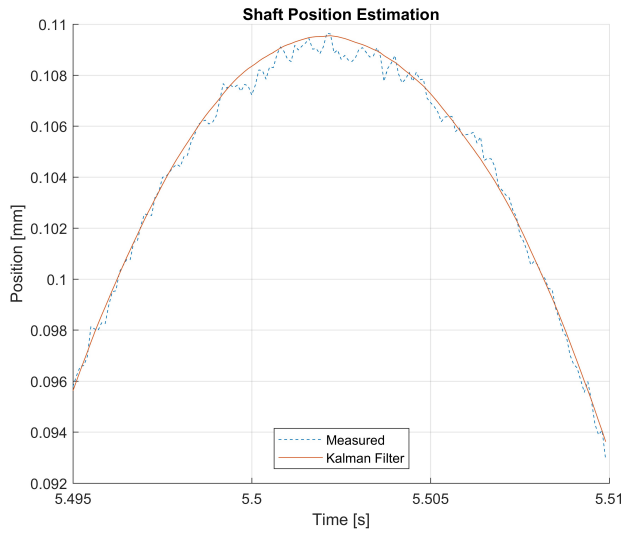

Figure 49. The shaft position estimate using a linear Kalman Filter.

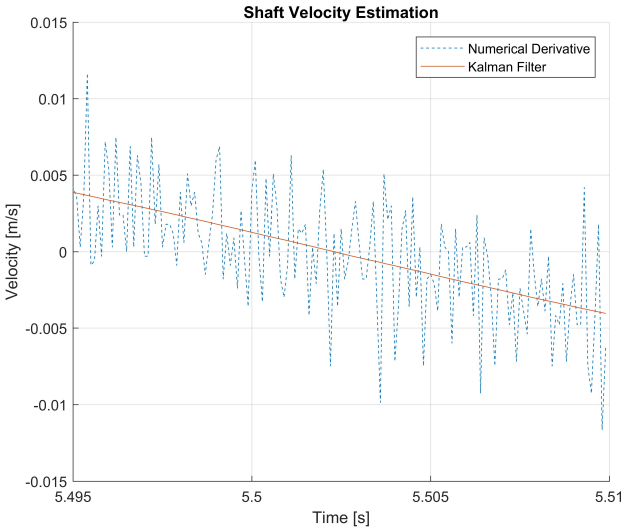

Figure 50. The shaft velocity estimate using a linear Kalman Filter.

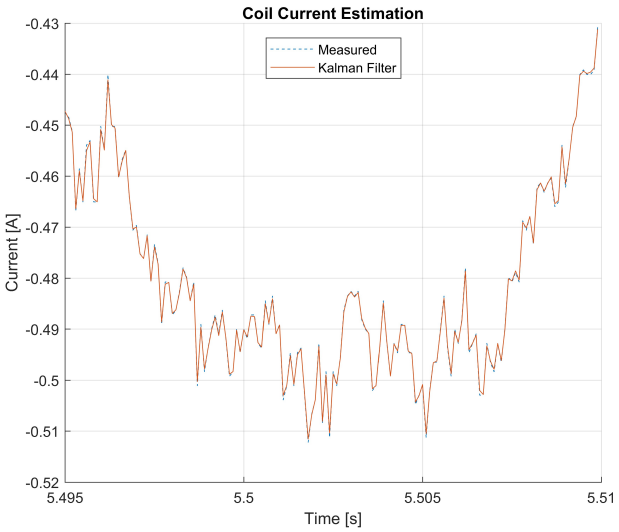

Figure 51. The bipolar magnetic coil current estimate using a linear Kalman filter.

measurements. Also note that the Kalman filter does not introduce a phase lag to the velocity estimate as a low-pass filter would. The velocity estimate is a critical component of any magnetic bearing control. The lack of natural damping in a magnetic bearing means that the controller needs a derivative (velocity) term to stabilize the closed-loop shaft dynamics. If the velocity estimate is poor, as is the case with the numerical derivative despite the extremely low position sensor noise, the maximum gain that can be practically implemented is reduced and the derivative term in the controller will add significant noise to the coil voltage control input. However, with the low-noise Kalman filter velocity estimate, the derivative gain can be increased, which makes the system more stable. Finally, the estimated coil current closely tracks the measured coil current. This is because the input (process) noise covariance is significantly higher than the current sensor noise, so the Kalman filter "trusts" the measured value of the coil current more and tracks it more closely.

6.4 Extended Kalman Filter

The extended Kalman filter is one nonlinear extension to the linear Kalman filter. The main difference is the state propagation and measurement equations. The system model is given by

$$\dot{x}(t) = f(x(t), u(t)) + w(t), \tag{273}$$

$$y(t) = h(x(t)) + v(t). \tag{274}$$

The prediction step for the state can be calculated numerically by

$$x_k^- = x_{k-1}^+ + f(x_{k-1}^+, u_{k-1}, t_k)(t_k - t_{k-1}). \tag{275}$$

Assuming that the state error estimate is smaller than the state vector, the system can be linearized at prior state using

$$F_{k-1} = \left.\frac{\partial f(x,u,t)}{\partial x}\right|_{x=x_{k-1}^+|u_{k-1}}, \tag{276}$$

and the state covariance estimate can be calculated using the standard Kalman filter equation.

$$P_k^- = F_{k-1} P_{k-1}^+ F_{k-1}^T + Q. \tag{277}$$

The measurement innovation is given by

$$z_k = y_k - h(x_k^-), \tag{278}$$

and the remaining steps for the extended Kalman filter are the same as the Kalman filter. For a single bipolar magnetic bearing, any of the nonlinear differential equations of motion can be used to propagate the states [i.e., Equations (28), (40), and (41)], and an appropriate linearized states space model [(i.e., Equation (87)] is used to propagate the prediction covariance.

7 PROJECT CHALLENGES

Unfortunately, a stabilizing controller for the loop-scale magnetic bearing vertical axis was not successfully created before the end of the period of performance for the project.

The first challenge to stabilizing the shaft position was the bandwidth of the magnetic coil dynamics, which is the underlying factor limiting the existence of a stabilizing magnetic bearing controller. Intuitively, if the coil current and consequently the force created by the electromagnet cannot respond as fast as the disturbance forces on the shaft, it will not be able to compensate for them to maintain stable operation.

For the loop-scale testbed, the radial bearing coil has a settling time of about 0.0146 seconds, which is a frequency of approximately 68 Hz. First, at 60 Hz, the operating speed of the pump is only slightly below the pump speed, so the controller would have difficulty stabilizing the shaft at the operating speed. Second and more importantly is the effective natural frequency of the bipolar magnetic bearings with current bias. Using the linearized model of the magnetic bearings, we can calculate the effective stiffness of the magnetic bearings, which is related to the magnitude of the bias current.

Figure 52 shows the horizontal and vertical natural frequencies of the linearized shaft model with varying bias currents, and Figure 53 shows the same for the rear shaft model.

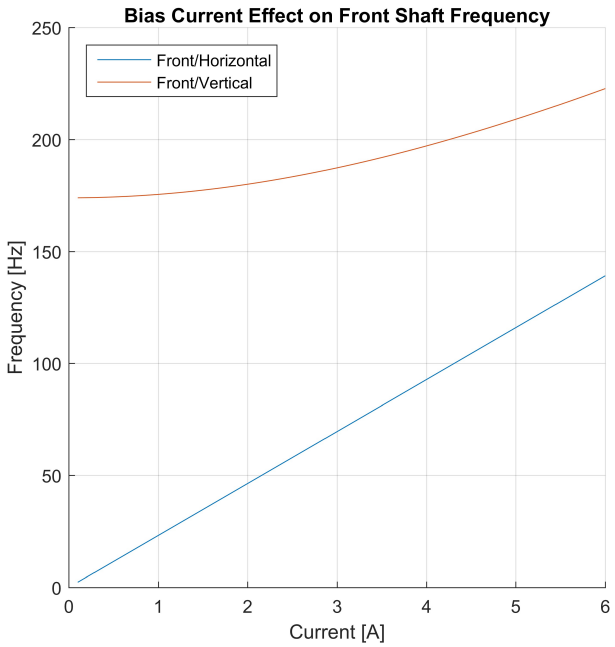

Figure 52. The natural frequency of the linearized shaft model for the front magnetic bearing.

The coil natural frequency is far lower than the maximum 316 Hz frequency of the front shaft in the vertical direction with a 6 A bias current. This means that the coil response needs to be improved through redesigning the coils to have lower inductances or by applying a lead compensator to the coil. The lead compensator was chosen to increase the bandwidth of the coils. The model of the induction coil from the

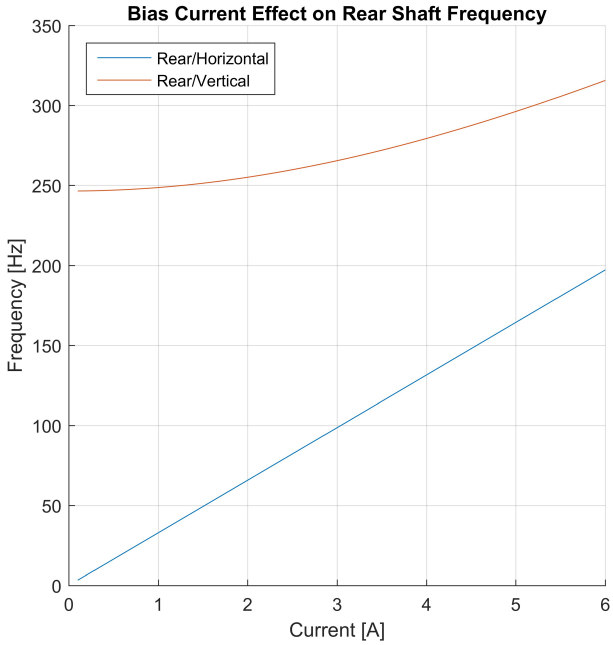

Figure 53. The natural frequency of the linearized shaft model for the rear magnetic bearing.

input to the current is given by the transfer function

$$\frac{I(s)}{U_c(s)} = \frac{a_0}{s + b_0}. \tag{279}$$

The lead compensator is given by

$$L(s) = \frac{s - z_0}{s - p_0}. \tag{280}$$

Finally, we will use an integral feedback controller, which leads to a closed-loop model of the coil dynamics given by

$$\mathcal{G}_c = \frac{a_1 s + a_2}{s^3 + b_1 s^2 + b_2 s + b_3}. \tag{281}$$

The shaft decoupled PID controller can be expressed in frequency/damping form as

$$\mathcal{G}(s) = \frac{\omega_n^2}{s^2 + 2\zeta\omega_n s + \omega_n^2}. \tag{282}$$

The linearized shaft transfer function is given by

$$\mathcal{G}_s = \frac{k_i/m}{s^2 - k_x/m}. \tag{283}$$

Using a PD controller, $\mathcal{H}(s) = k_d s + k_p$, we can rewrite the closed-loop transfer function of $\mathcal{G}_{cl}$ and the controller as

$$\mathcal{G}_{cl} = \frac{\mathcal{G}_s \mathcal{H}}{1 + \mathcal{G}_s \mathcal{H}}, \tag{284}$$

$$= \frac{\frac{k_i}{m}(k_d s + k_p)}{s^2 + \frac{k_i k_d}{m} s + (\frac{k_i}{m} k_p - k_x)}, \tag{285}$$

so to set the cutoff frequency of the transfer function denominator, we want

$$\omega_n^2 = \frac{k_i}{m}k_p - k_x, \implies k_p = \frac{m}{k_i}(\omega_n^2 + k_x). \tag{286}$$

Similarly

$$\frac{k_i}{m}k_d = 2\zeta\omega_n \implies k_d = \frac{m}{k_i}2\zeta\omega_n. \tag{287}$$

The next challenge to developing the stabilizing controller was an error in the wiring of the radial magnetic bearings. Some of the coils' positive and negative terminals were wired backwards, which caused a coupling of the magnetic field between the x and y axes. This was first noticed in open loop current testing of the coils. Figure 54 show two successive voltage steps into the front radial bearing's x-axis coil and then y-axis coil, respectively. Figure 55 shows that instead of being decoupled, a change in the magnetic field of each axis induces a magnetic field in the opposite axis as the magnetic field is created and collapses, which in turn induces a current spike. This coupling caused the bearing forces to be uncontrollable, which

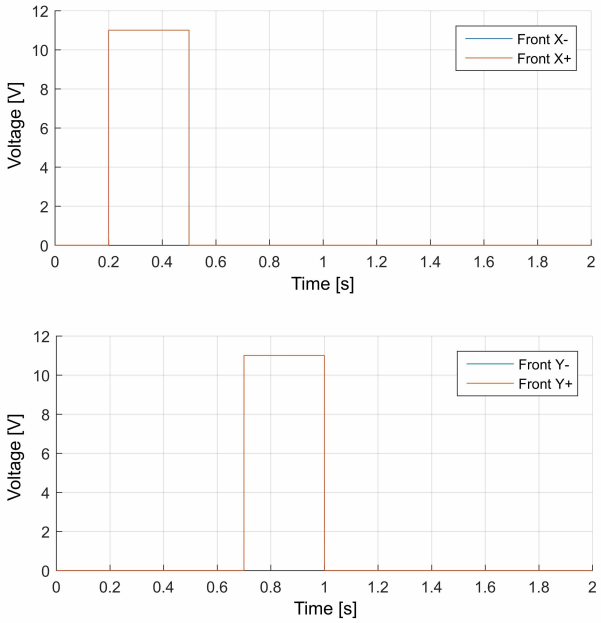

Figure 54. A voltage step input to the front radial bearing x-axis followed by a step input to the front radial bearing y-axis.

destabilized the shaft controller. When the wiring was corrected, the horizontal axis was able to be stabilized, as shown in Figure 56.

However, a stabilizing controller for the vertical axis was not found. After further investigation, it was determined that this was due to issues with the commercial H-bridge drivers breakout boards used in the power electronics system. For a vertical axis stabilizing controller to exist, the required bandwidth of the coil current could not be achieved by the coil lead compensator and feedback controller due to operation of the H-bridge drivers in omni-directional mode. The drivers can be operated in either the omni-direction or

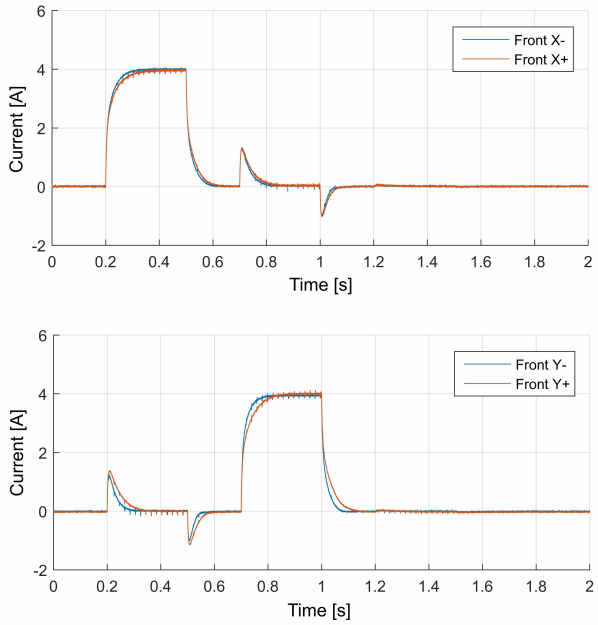

Figure 55. The current response of the front radial magnetic bearings following step inputs when incorrectly wired.

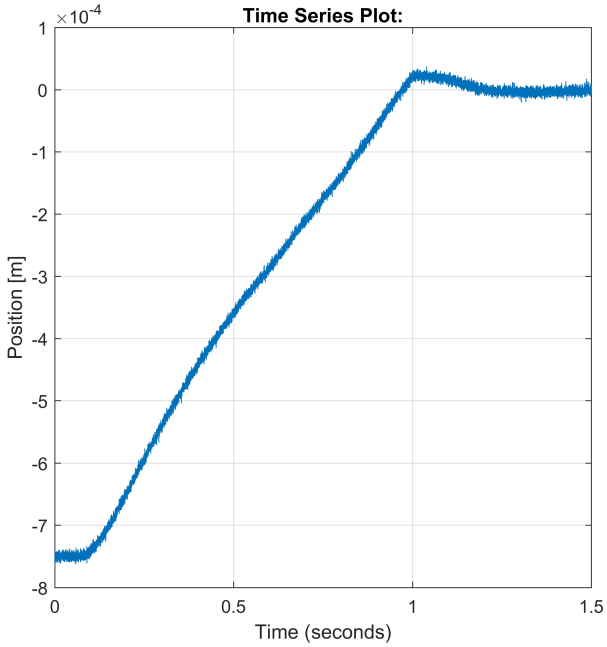

Figure 56. Stable response of the horizontal axis magnetic bearing controller.

bi-directional mode. In omni-directional mode, the output voltage is restricted to $v(t) \geq 0$. In bi-directional mode, the coil voltage can be both positive and negative. When the drivers operate in omni-directional mode, the feedback control can increase the speed with which the current increases, but to down-regulate the coil current, the controller can only set $v = 0$ and let the magnetic field and consequently the current collapse at the speed defined by the physical parameters R/L of the magnetic coil. As an analogy, this is like a car that has an accelerator but no brakes. The car can use the accelerator to speed up and vary the rate of positive acceleration but must coast to slow down or stop. In bi-directional mode, the ability of the controller to apply a negative voltage on the magnetic coils means that the magnetic field and coil current can be forced to collapse more quickly, and consequently the coil lead compensator and feedback controller can achieve the higher bandwidth needed to stabilize the vertical magnetic bearing axis. Another side effect of using the omni-directional voltage control mode on the drivers is that it adds nonlinearities to the coil dynamics. The closed-loop dynamics of the coil current will have different models when the current is increasing and when the current is decreasing, which violates necessary conditions for linearity. Omni-directional mode also adds the hard nonlinearity of $v(t) > 0$, which causes problems with the PID controller. Care must be taken in the implementation of a PID controller to prevent integral windup[§] when the actual control signal does not match the control signal from the PID controller.

To mitigate the magnetic coil bandwidth limitations imposed by the omni-directional mode of the H-bridge drivers, they were all re-wired to operate in bi-directional mode. However, during testing the bi-directional mode did not operate properly. A single H-bridge module could be operated in bi-directional mode, but when more than one module operated at the same time, the drivers would no longer operate in bi-polar mode. After careful inspection we found that the commercial H-bridge driver breakout boards did not adhere to the integrated circuit and mosfet manufacturers' recommendations. Instead of using separate power and instrument ground planes, the breakout boards utilized a single ground plane. This caused noise from the power outputs to corrupt the 0–5 V signals used to set the driver mode. In addition, the use of a single ground plane explains the large current sensor noise seen in experiments. To develop a stabilizing controller for the vertical axis of the loop-scale testbed, the H-bridge drivers would need to be redesigned for higher performance, fabricated, and installed in the power electronics enclosure. Although the main goals of the research were successfully accomplished, regrettably, a 4-month delay in the delivery of the loop-scale testbed components from the fabricator, testbed assembly, system identification, and controller testing began close to the end of the project period of performance. This limited the time available for controller testing, and additional expenses to design and install custom H-bridge drivers were incurred, preventing the completion of the loop-scale testbed. We feel that these issues related to bipolar field drive, magnetic relaxation times, and system frequency response are important considerations for subsequent research and design of other magnetic suspension systems.

[§]Integral windup happens when there is a large error signal into the controller. For example, a step change in the reference input will cause the integral term to accumulate during the transient, which will continue to cause a large control effort after the system reaches the new equilibrium point. This in turn causes overshoot of the trajectory.

8 FUTURE RESEARCH

One area of future research is the application of these techniques to high-temperature devices such as pumps for molten salt nuclear reactors and solar collectors with operating temperatures near 700 °C. Successfully creating high-temperature electromagnetic devices will require an understanding the dynamics of electromagnetic fields and reluctance forces at high temperatures and methods for fabricating high-temperature coils with insulation that will not break down under electric fields, over time, or under mechanical stresses. Another important area of research is developing temperature-dependent dynamic models of the pump and experimentally determining the uncertainty bounds associated with temperature-dependent material properties. Investigating the theoretical bounds on the controller performance and stability related to the inductance of the magnetic coils and methods for mitigating the impact of coil inductance should be investigated. This will be particularly important as the size of the magnetic bearing increases and for thrust bearings that do not utilize laminations, which increases their eddy current magnitude and, as a result, their inductance. This will also be important when using a protective can on the rotor and stator as it will act like a low-pass filter on the magnetic field because of the development and collapse of eddy currents, which will increase the total inductance of the magnetic circuit. For submerged magnetic bearings, a model should be developed that incorporates both shaft flexible modes and fluid forces to be used for robust control design. Finally, the application of control techniques to design a magnetic bearing controller that are robust to the uncertain nonlinear fluid forces and flexible shaft modes should be researched.

9 CONCLUSIONS

In the course of this research, ORNL developed a conceptual design for a high-temperature (>700 °C) pump for molten salt. Specifications for the control system, motor/pump, mechanical performance, rotational dynamics, electrical and magnetic properties, sensors, high-temperature wiring, environmental conditions, and reliability were developed. Then a comprehensive analysis of the manufacturability of the conceptual design was created which showed that the design can be created using modern fabrication techniques. A model of the position-dependent fluid forces due to the thin layer of fluid between the rotor and stator was incorporated into a Jeffcott rotor model of the conceptual design. The stability and performance controllers designed using different control design theories were tested on the dynamic model of the conceptual design. Then a bench-scale testbed was designed and fabricated to validate system models and test control designs, system identification, and state estimation. A power electronics system for controlling magnetic coil voltage was created and successfully used to levitate and stabilize the bench-scale testbed shaft. Grey box system identification tools were used to estimate the model parameters for the bench-scale testbed, and the identified parameters closely matched the expected values. Finally, a loop-scale testbed with submerged magnetic bearings was designed and fabricated. This testbed provided insight into practical issues with the existence and implementation of stabilizing magnetic bearing controllers.

10 REFERENCES

[1] Paul D. Groves. *Principles of GNSS, Interial, and Multisensor Integrated Navigation Systems*. Artech House, 2013.

[2] Kenneth Huebner. *The finite element method for engineers*. J. Wiley, New York, 2001.

[3] Mark Jansen, Gerald Montague, Andrew Provenza, and Alan Palazzolo. High speed, high temperature, fault tolerant operation of a combination magnetic-hydrostatic bearing rotor support system for turbomachinery. Technical Report NASA/TM-2004-212952, NASA, 2004.

[4] Roger A. Kisner, David L. Fugate, Alexander M. Melin, David E. Holcomb, Dane F. Wilson, Pamela C. Silva, and Carola C. Molina. Evaluation of manufacturability of embedded sensors and controls with canned rotor pump system. Technical report, Oak Ridge National Laboratory ORNL/TM-2013/269, 2013.

[5] Roger A. Kisner, Alexander M. Melin, Timothy A. Burress, David L. Fugate, David E. Holcomb, John B. Wilgen, John M. Miller, Dane F. Wilson, Pamela C. Silva, Lynsie J. Whitlow, and Fred J. Peretz. Embedded sensors and controls to improve component performance and reliability: Conceptual design report. Technical report, Oak Ridge National Laboratory ORNL/TM-2012/433, 2012.

[6] Rohan Mandloi and Pritesh Shah. Methods for closed loop system identification in industry. *Journal of Chemical and Pharmaceutical Research*, 7(1):892–896, 2015.

[7] Alexander M. Melin, Roger Kisner, and David L. Fugate. Embedded sensors and controls to improve component performance and reliability: System dynamics modeling and control system design. Technical Report ORNL/TM-2013/415, Oak Ridge National Laboratory, 2013.

[8] Alexander M. Melin and Roger A. Kisner. Embedded sensors and controls to improve component performance and reliability - loop-scale testbed design report. Technical report, Oak Ridge National Laboratory ORNL/TM-2016/563, 2016.

[9] Alexander M. Melin, Roger A. Kisner, Anis Drira, and Frederick K. Reed. Embedded sensors and controls to improve component performance and reliability - bench-scale testbed design report. Technical report, Oak Ridge National Laboratory ORNL/TM-2015/584, 2015.

[10] Alexander M. Melin, Roger A. Kisner, and David L. Fugate. Advanced instrumentation and controls for extreme environments. *IEEE Instrumentation and Measurement Magazine*, 16(3), June 2013.

[11] Alexander M. Melin, Roger A. Kisner, David L. Fugate, and David. E. Holcomb. Hydrodynamic effects on modeling and control of a high temperature active magnetic bearing pump with a canned rotor. In *NPIC&HMIT*, 2015.

[12] T. Schuhmann, W. Hofmann, and R. Werner. Improving operational performance of active magnetic bearings using kalman filter and state feedback control. *IEEE Transactions on Industrial Electronics*, 59(2):821–829, Feb 2012.

[13] Dan Simon. *Optimal state estimation*. J. Wiley, New York, 2006.

[14] Alfons Traxler and Eric Maslen. *Magnetic Bearings: Theory, Design, and Application to Rotating Machinery*. Springer, 2010.